

2024-08-01

## Comparative Study Of Hydrogen Embrittlement On Ebm Inconel 718 As-Built And Hiped Specimens

Julio Cesar Diaz  
*University of Texas at El Paso*

Follow this and additional works at: [https://scholarworks.utep.edu/open\\_etd](https://scholarworks.utep.edu/open_etd)



Part of the [Engineering Commons](#)

---

### Recommended Citation

Diaz, Julio Cesar, "Comparative Study Of Hydrogen Embrittlement On Ebm Inconel 718 As-Built And Hiped Specimens" (2024). *Open Access Theses & Dissertations*. 4174.  
[https://scholarworks.utep.edu/open\\_etd/4174](https://scholarworks.utep.edu/open_etd/4174)

This is brought to you for free and open access by ScholarWorks@UTEP. It has been accepted for inclusion in Open Access Theses & Dissertations by an authorized administrator of ScholarWorks@UTEP. For more information, please contact [lweber@utep.edu](mailto:lweber@utep.edu).

COMPARATIVE STUDY OF HYDROGEN EMBRITTLEMENT ON EBM INCONEL 718  
AS-BUILT AND HIPED SPECIMENS

JULIO CESAR DIAZ

Master's Program in Mechanical Engineering

APPROVED:

---

Francisco Medina, Ph.D., Chair

---

Edel Arrieta, Ph.D.

---

Amit Lopes, Ph.D.

---

Stephen L. Crites, Jr., Ph.D.  
Dean of the Graduate School

Copyright 2024 Julio Diaz

## **Dedication**

This thesis is dedicated to my family who has supported me throughout every step of my educational journey, my friends who have encouraged me to keep moving forward, and my mentors and colleagues who have taught me invaluable lessons.

COMPARATIVE STUDY OF HYDROGEN EMBRITTLEMENT ON EBM INCONEL 718  
AS-BUILT AND HIPED SPECIMENS

by

JULIO CESAR DIAZ, BS

THESIS

Presented to the Faculty of the Graduate School of  
The University of Texas at El Paso  
in Partial Fulfillment  
of the Requirements  
for the Degree of

MASTER OF SCIENCE

Department of Mechanical Engineering  
THE UNIVERSITY OF TEXAS AT EL PASO

August 2024

## **Acknowledgments**

I want to thank Dr. Francisco Medina for allowing me to work at the W.M. Keck Center for 3D Innovation and placing me in projects that have been fundamental for my professional growth. Thanks to Dr. Edel Arrieta for his mentorship and guidance throughout this project and throughout my bachelor's and master's. Thanks to Dr. Jamaa Bouhattate for allowing me to do my thesis experimentation phase at La Universite de la Rochelle and for her mentorship throughout this process. Thanks to Dylan Cozlyn and Achraff for teaching me experimental procedures and helping me expand my knowledge of materials engineering. Thanks to Shadman Tashin for teaching me how to operate the additive manufacturing machine used in this work and helping me throughout my entire thesis. Lastly, I want to thank my colleagues and peers at the Keck Center for all the help they have given me and all the good times we have had.

## Abstract

This study investigates the effects of hydrogen embrittlement (HE) on Inconel 718 parts produced using Electron Beam Melting (EBM) with a spot melting scanning strategy, focusing on analyzing the material's microstructure and mechanical properties. This research aims to understand the impact of hydrogen charging on both as-built and Hot Isostatically Pressed (HIPed) samples of Inconel 718, a material widely used in high-stress applications in aerospace and energy industries.

The methodology included detailed characterization using techniques such as Electron Backscatter Diffraction (EBSD), Transmission Electron Microscopy (TEM), and Scanning Electron Microscopy (SEM) followed by hydrogen charging of EBM-fabricated Inconel 718 samples. Mechanical testing, including microhardness and tensile tests, was conducted to evaluate the changes in properties due to hydrogen charging.

Microstructural analysis through EBSD revealed a randomized crystallographic texture, with TEM and SEM providing insights into dislocation structures and precipitate distributions. Key results indicated hydrogen charging significantly increased hydrogen content, especially in HIPed samples. Microhardness tests showed a pronounced hardness gradient near the charging face, demonstrating the embrittling effect of hydrogen. Tensile testing revealed that while the as-built samples maintained their mechanical properties after hydrogen charging, HIPed samples experienced a substantial reduction in ultimate tensile strength, yield strength, and elongation.

The study concludes that EBM-fabricated Inconel 718 components are susceptible to hydrogen embrittlement, particularly after HIPing. The findings underscore the need for optimized EBM and post-processing techniques to mitigate the risks of hydrogen embrittlement, ensuring enhanced performance in hydrogen-rich environments. These insights contribute to the broader

application of EBM Inconel 718 in critical industries, emphasizing the importance of managing hydrogen effects in advanced manufacturing processes.

## Table of Contents

Dedication .....	iii
Acknowledgments.....	v
Abstract .....	vi
Table of Contents.....	viii
List of Tables .....	xi
List of Figures .....	xii
1. Chapter 1: Introduction .....	1
2. Chapter 2: Literature Review .....	3
2.1 Hydrogen Embrittlement .....	3
2.1.1 HE Mechanism.....	4
2.1.2 HE and Microstructure.....	6
2.1.3 HE and Mechanical Properties.....	10
2.1.4 Other Factors.....	12
2.1.5 Mitigation Strategies.....	12
2.2 Additive Manufacturing.....	13
2.2.1 Material Extrusion .....	13
2.2.2 Material Jetting .....	14
2.2.3 VAT Photopolymerization.....	15
2.2.4 Binder Jetting.....	16
2.2.5 Directed Energy Deposition.....	17
2.2.6 Sheet Lamination .....	18
2.2.7 Powder Bed Fusion .....	19
2.2.7.1 Advantages and Disadvantages of EBM.....	20
2.2.7.2 EBM Overview .....	22
2.2.7.3 Parameters EBM .....	25
2.2.7.4 Scanning Strategies.....	27
2.2.7.5 Microstructure and Mech Properties on EBM.....	27
2.2.7.6 Mechanical Properties EBM .....	28

2.2.7.7 Post Processing on EBM.....	29
2.2.8 AM and HE .....	29
2.3 Inconel 718.....	30
2.3.1 Inconel 718 Microstructure.....	34
3. Chapter 3: Materials and Methods .....	37
3.1 Powder Feedstock Characterization.....	37
3.2 EBM Manufacturing .....	37
3.2.1 Parameters.....	39
3.2.2 Heat Treatments .....	41
3.3 Characterization .....	42
3.3.1 Electron Backscatter Diffraction (EBSD).....	42
3.3.2 Optical Microscopy.....	44
3.3.3 Transmission Electron Microscopy (TEM) .....	45
3.3.4 Scanning Electron Microscopy .....	46
3.4 Hydrogen Charging.....	47
3.4.1 Thermal Desorption Spectroscopy (TDS) .....	49
3.5 Microhardness.....	49
3.6 Tensile Tests .....	51
4. Chapter 4: Results and Discussion.....	53
4.1 Characterization Results .....	53
4.1.1 EBSD Results.....	53
4.1.1.1 As-built Samples.....	53
4.1.1.2 HIPed Samples.....	55
4.1.2 Microscopy Results.....	58
4.1.2.1 As-built Samples .....	59
4.1.2.2 HIPed Samples.....	62
4.1.3 TEM Results .....	65
4.1.3.1 HIPed Condition .....	65
4.1.4 SEM Results.....	69
4.1.4.1 As-Built Samples .....	69
4.1.4.2 HIPed Samples .....	71
4.1.5 Charging Results.....	75

4.2 Microhardness Results .....	76
4.3 Tensile Tests Results.....	77
5. Conclusion .....	81
References.....	83
Appendix.....	91
Vita	94

## List of Tables

Table 1: Chemical Composition of Inconel 718 [93] .....	31
Table 2. Stochastic and Single Directional Shifted Parameters.....	39
Table 3. As-Built Element Distribution .....	69
Table 4. HIPed Element Distribution.....	72
Table 5. Mechanical Properties after Tensile Testing .....	80

## List of Figures

Figure 2.1: Conditions for HE [11].....	5
Figure 2.1: Hydrogen permeation on a) the matrix, b) the surface, c) the subsurface, d) grain boundaries, e) edge dislocations, and f) vacancies [14].....	6
Figure 2.3: Stress-strain curves of IN718 alloy without and with hydrogen charging at 0 mA cm <sup>-2</sup> , 75 mA cm <sup>-2</sup> , 220 mA cm <sup>-2</sup> , and 590 mA cm <sup>-2</sup> [24].....	11
Figure 2.4: SEM images of tensile samples (a) hydrogen free; (b) 75 mA cm <sup>-2</sup> ; (c) 220 mA cm <sup>-2</sup> ; (d) 590 mA cm <sup>-2</sup> . White circles indicating microvoids; Black arrows indicating hydrogen-assisted cracking [24].....	11
Figure 2.5: Schematic of Material Extrusion system [40] .....	14
Figure 2.6: Schematic of Material Jetting system [47] .....	15
Figure 2.7: Schematic of Vat Photopolymerization systems [50] .....	16
Figure 2.8: Schematic of Binder Jetting system [52].....	17
Figure 2.9: Schematic of a DED system. A) laser and powder and B) electron beam and wire [55].....	18
Figure 2.10: Schematic of a Sheet Lamination system [57] .....	19
Figure 2.11: Market share of metal AM technologies [58]. .....	19
Figure 2.12: Schematic of a) overall Freemelt ONE EBM system and b) EB source [74] .....	23
Figure 2.13: Materials strength at different temperatures [94]. .....	32
Figure 2.14: (A) TEM diffraction pattern image of [001] zone of $\gamma$ matrix exhibiting $\gamma'$ and $\gamma''$ superlattice reflections; (B) TEM dark-field image using the $\gamma''(110)/\gamma'(011)$ diffraction spot; (C) Image showing $\delta$ -phase along high-angle grain boundaries [81]. .....	35
Figure 2.15: Powder Size Distribution Graph.....	37

Figure 3.1: Pixelmelt program interface. ....	38
.....	38
Figure 3.2: CAD models of A) Rectangular prisms, 4 Samples:.....	38
15 x 15 x 25 mm. B) Rectangular prism, 1 Sample: 20 x 20 x 25 mm.....	38
Figure 3.3: A) & B) Represent the 5 samples and environment right after opening the chamber.	
C) Represents the samples after being machined off the plate (the arrows represents the rake	
direction). D) Illustrates the typical (EBM characteristic) rough surface finish on the prism.....	41
Figure 3.4: HIP process graph. ....	42
Figure 3.5: ZEISS Crossbeam 340-VP EBDS machine [106].....	43
Figure 3.6: Electro-etching setup.....	44
Figure 3.7: Keyence VH-ZST microscope .....	45
Figure 3.8: Jeol TEM Machine .....	46
Figure 3.9: SEM Machine, Axia.....	47
Figure 3.10: Sample in resin (charging preparation) .....	48
Figure 3.11: A) General and B) Close-up view of the H-charging Setup.....	48
Figure 3.12: Horiba Hydrogen Analyzer .....	49
Figure 3.13: Indentation Schematic .....	50
Figure 3.14: Anton paar Step 4, Microhardness Apparatus.....	51
Figure 3.15: Tensile Sample Dimensions .....	51
Figure 3.16: Kammrath & Weiss Tensile Apparatus.....	52
Figure 4.1: A) Horizontal and B) Vertical As-built EBSD Map .....	54
Figure 4.2: A) Horizontal and B) Vertical As-Built Pole Figures .....	55
Figure 4.3: Random vs CSL distribution. As-Built Vertical. ....	55

Figure 4.4: A) Horizontal and B) Vertical HIPed EBSD Map .....	56
.....	57
Figure 4.5: A) Horizontal and B) Vertical HIPed Pole Figures.....	57
Figure 4.6: Random vs CSL distribution. HIPed Vertical.....	57
Figure 4.7: Grain Size for As-built and HIPed Graph .....	58
Figure 4.8: CSL vs Random GB Graph .....	58
Figure 4.9: As-built Vertical. 200 um scale. XZ Plane. Red arrow showing possible intergranular cracking.....	60
Figure 4.10: As-built Horizontal. 200 um scale. XZ Plane.....	60
Figure 4.11: As-built Vertical. 25 um scale. XZ Plane.....	61
Figure 4.12: As-built Horizontal. 25 um scale. XZ Plane.....	61
Figure 4.13: HIPed Vertical, Scale 200 um, XZ Plane.....	63
Figure 4.14: HIPed Horizontal, Scale 200 um, XY Plane .....	64
Figure 4.15: HIPed Vertical, Scale 25 um, XZ Plane, Arrows showing possible Carbides.....	64
Figure 4.16: HIPed Horizontal, Scale 25 um, XY Plane, Arrows showing possible Carbides. ....	65
Figure 4.17: TEM Bright field image of a Grain Boundary (GB) and a subgrain boundary (SGB) and diffraction pattern corresponding to the matrix .....	66
Figure 4.18: TEM Bright field images of Low Dislocation Density .....	67
Figure 4.19: Bright field image and dark field image showing (with white arrows) gamma prime precipitate and the corresponding diffraction spot.....	68
Figure 4.20: As-Built SEM Image. Red arrows showing carbides. Blue circles showing niobium-molybdenum nitrides. ....	70

Figure 4.21: As-Built Element Color Distribution. A) Nb, B) Mo, C) Al, D) C, E) N, F) Cr, G) Fe, and H) Ni.....	71
Figure 4.22: HIPed Sample SEM Image.....	72
Figure 4.23: HIPed Element Color Distribution. A) Nb, B) Mo, C) Al, D) C, E) N, F) Cr, G) Fe, H) Ni, and I) Ti. ....	74
Figure 4.24: Hydrogen Flow Graph. As-built vs HIPed.....	75
Figure 4.25: Microhardness Measurements Results .....	77
Figure 4.26: As-built Stress vs. Strain Graph .....	79
Figure 4.27: HIPed Stress vs. Strain Graph .....	79

## 1. Chapter 1: Introduction

Inconel 718, a nickel-chromium-based superalloy, is extensively utilized in industries that demand high strength and resistance to extreme environments, such as aerospace and energy. Its remarkable mechanical properties, including high tensile strength, creep resistance, and oxidation resistance, make it an ideal material for critical applications. However, these properties can be significantly affected by manufacturing processes and environmental factors, such as hydrogen embrittlement (HE).

Hydrogen embrittlement is a phenomenon where hydrogen atoms diffuse into the metal, leading to a reduction in ductility and toughness, ultimately causing premature failure. This is a critical concern for components exposed to hydrogen-rich environments, such as those found in aerospace and energy sectors. Understanding the effects of HE on Inconel 718 is essential for ensuring the reliability and longevity of components made from this material.

The advent of advanced manufacturing techniques, such as Electron Beam Melting (EBM), has revolutionized the production of complex geometries and high-performance components. EBM is an additive manufacturing (AM) process that uses an electron beam to selectively melt metal powder layer by layer, producing near-net-shape parts with high density and excellent mechanical properties. However, the susceptibility of EBM-fabricated Inconel 718 to hydrogen embrittlement, especially after post-processing treatments like Hot Isostatic Pressing (HIPing), is not well understood.

Previous studies have explored the microstructural characteristics and mechanical properties of Inconel 718 produced by traditional manufacturing methods and various AM techniques. Research has shown that the microstructure of EBM-fabricated parts is typically characterized by elongated columnar grains aligned with the build direction. HIPing is often

employed to relieve residual stresses and improve ductility, but it may also affect the material's susceptibility to HE.

Limited research has been conducted on the combined effects of EBM fabrication, HIPing, and hydrogen charging on Inconel 718. The existing literature highlights the need for a comprehensive understanding of how these factors interact and influence the material's performance, particularly in hydrogen-rich environments.

This study aims to investigate the effects of hydrogen embrittlement on Inconel 718 parts produced by EBM, with a focus on both as-built and HIPed conditions. The specific objectives of this research are:

- To characterize the microstructural features of EBM-fabricated Inconel 718 using techniques such as Electron Backscatter Diffraction (EBSD), Transmission Electron Microscopy (TEM), and Scanning Electron Microscopy (SEM).
- To evaluate the mechanical properties of as-built and HIPed Inconel 718 samples before and after hydrogen charging.
- To analyze the hydrogen diffusion behavior in EBM-fabricated Inconel 718 and its impact on the material's microstructure and mechanical properties.

The significance of this study lies in its potential to enhance the understanding of hydrogen embrittlement in EBM-fabricated Inconel 718, thereby informing the development of optimized manufacturing and post-processing techniques. By addressing the challenges associated with HE, this research contributes to the broader application of Inconel 718 in critical industries, ensuring the production of reliable and high-performance components.

## 2. Chapter 2: Literature Review

### 2.1 HYDROGEN EMBRITTLEMENT

Hydrogen Embrittlement (HE) is a phenomenon that occurs when hydrogen atoms get infused into a metal's lattice or microstructure and, as a consequence, degrades the mechanical properties of the metal by making it brittle and, therefore, more prone to cracking/fracturing. Metals that are most commonly affected by this are high-strength metals, particularly high-strength steels; high-strength metals usually have a higher density of dislocations within their microstructure, which create spaces for hydrogen atoms to get trapped in and start embrittling the material [1]. Moreover, high-strength metals are usually less ductile and more brittle to begin with [2]. Nevertheless, metals such as iron, nickel, titanium, cobalt and their alloys are also affected by HE [3].

There are a few main industries or settings where this has become an issue, as metals are in constant contact with hydrogen. In the aerospace industry, some components might be in constant exposure to manufacturing processes or environments where hydrogen is present [4]. Automotive components such as fasteners and gears might be subjected to electroplating or pickling, processes which makes them susceptible to HE [5]. Gas and oil pipes are also at risk because of their inherent functions, carrying substances that might be corrosive and contain hydrogen [6]. Again, in the case of many electronic devices, hydrogen is induced through electroplating. From these examples, it can be observed that HE does not only happen because of the environment or function the components are intended for but also because of the manufacturing or enhancement processes they are subjected to. Some examples of HE-inducing processes include heat treatments, welding and brazing, casting, cold working, cleaning and degreasing, surface coating, and the ones already mentioned, such as electroplating and pickling [7], [8]. This happens

due to moisture in procedures such as water in plating baths when electroplating or internal stresses caused such as during welding [9], [10].

Another area where hydrogen plays a significant role is the energy sector. When looking for better fuel options to mitigate greenhouse gas emissions, hydrogen is a more sustainable energy as it can be produced through multiple low-carbon processes. Now, the challenge is building the necessary infrastructure to deal with the production, transportation, and storage of that hydrogen while mitigating all of the safety risks associated with it. This will involve selecting better materials to handle the hydrogen without causing major losses in the performance and lifespan of these components due to HE. These components, when used in contact with hydrogen, are often subjected to different stress levels and pressures, which further affect their susceptibility to HE.

### **2.1.1 HE Mechanism**

HE is a complicated subject to fully understand as hydrogen atoms often move and jump from one place of the lattice structure to another. Nevertheless, a few things have been observed. There are three criteria for HE damage to occur as seen in Figure 2.1: (1) there must be a susceptible metal (different metals have different levels of vulnerability towards hydrogen), (2) the material should be experiencing loading/stresses (or residual stresses from the manufacturing method), and (3) the environment must contain hydrogen [11].

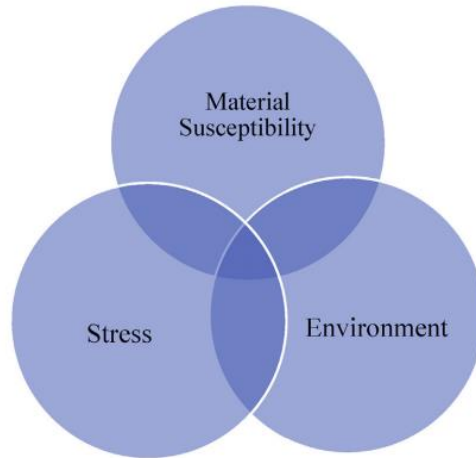


Figure 2.1: Conditions for HE [11]

As mentioned above, the main issue with these materials is that they come in contact with hydrogen. Whenever the hydrogen atoms have contact with the metal surface, the adsorption process begins. Hydrogen atoms are characterized by their high reactivity; they readily interact with other atoms or molecules due to their electron configuration, which predisposes them to form bonds with other atoms or molecules, in this case, the metal surface [12]. After this, the hydrogen atoms dissolve into the metal's microstructure as they are very small compared to metal atoms and start distributing themselves finding pathways through the metal's lattice in a process called diffusion. These atoms will often migrate to high triaxial stress regions as this state of stress within the material distorts or opens up space (or interstitial sites) in the metal lattice creating areas of low hydrogen concentration and low energy state and thus effective trapping sites for the hydrogen. These sites include grain boundaries, dislocations, and vacancies in the microstructure as seen in Figure 2.2 [13].

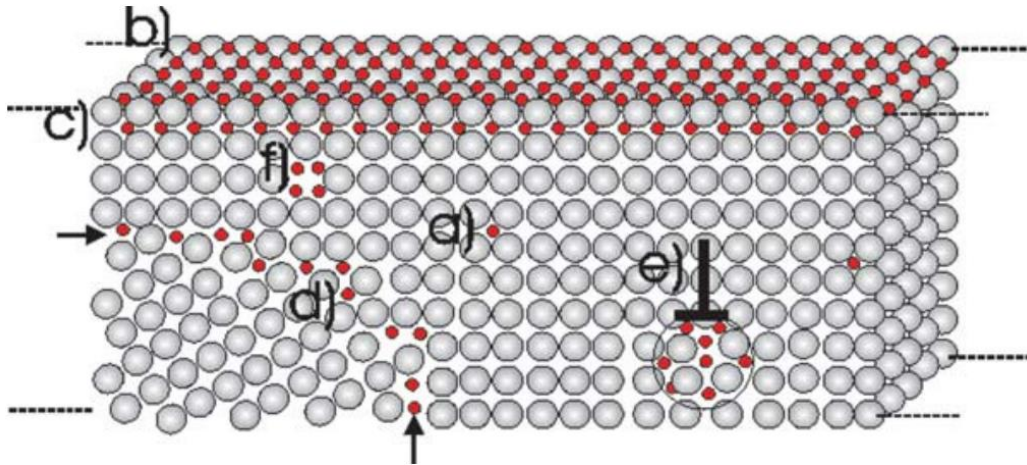


Figure 2.1: Hydrogen permeation on a) the matrix, b) the surface, c) the subsurface, d) grain boundaries, e) edge dislocations, and f) vacancies [14].

These atoms concentrate and form clusters in these specific areas of the microstructure and create pressure that helps with crack initiation [15]. The way these atoms are distributed across the metal largely depends on the material's microstructure; grain morphology, its defects, and whether the material is under stress or not.

### 2.1.2 HE and Microstructure

Crystal structure, grain morphology, and the shape, size, and configuration of the grains in the material's microstructure play an important role. The crystal structure determines the number of interstitial sites a material has between its metal atoms, which can serve as places for the hydrogen atoms to reside. Usually, materials that possess a body-centered cubic (BCC) tend to have more interstitial sites than face-centered cubic (FCC) structures [16]. This could cause a higher concentration and risk of HE. Grain size and orientation also play an important role. In smaller grain sizes, the number of grain boundaries in a given area increases, which can play either a positive or negative role in hydrogen distribution depending on their shape and orientation, as they can either inhibit hydrogen entrapment or disperse it from places where it could concentrate

and create vulnerable points. For example, Koichi Takasawa et al. studied how grain size affects steel's resistance to hydrogen embrittlement [17]. They studied steel samples with varying grain sizes against high-pressure hydrogen and performed tensile tests. Finer-grained steel absorbed more hydrogen but fractured less easily, indicating better resistance, suggesting finer grains disperse hydrogen, preventing it from concentrating at weak spots and causing cracks. The grain orientation has significant importance in the way hydrogen propagates, where it concentrates, and thus, where cracks might initiate given stress is being applied. Wei Wang et al. investigated how the orientation of crystals in steel affects its weakness to hydrogen embrittlement. The researchers found that specific crystal orientations, like  $\{100\}$ , were more prone to hydrogen cracks, while others, like  $\{111\}$ , were more resistant; aside from these high-angle misorientations (50-60 deg) were the most vulnerable to fracture [18].

As mentioned before, when it comes to the defects, the most important are vacancies, dislocations, and grain boundaries (GB) [19]:

- Vacancies: these vacancies represent missing lattice atoms of the metals microstructure, making them ideal spaces for the smaller hydrogen atoms to get in and start forming clusters.
- Dislocations: they are line defects in a crystal structure which is represented as a misarrangement in the atomic structure. The most common types of dislocations are screw and edge dislocations; materials often have a combination of both. They can act as pathways for hydrogen and act as efficient diffusion paths making it possible for those atoms to reach critical areas such as grain boundaries. They provide enhanced mobility to these molecules which accelerates the hydrogen accumulation. Also, whenever the material

is subjected to a force or stress, the dislocations within the material start piling up which can be detrimental as this means an even larger concentration of hydrogen.

- Grain Boundaries (GB): as atoms arrange themselves within a material and form grains, they also create GBs which is the area where two or more different grains meet. These GBs form a perfect place for hydrogen atoms to either accumulate in them or pass through given the lower atomic density of the boundary. GBs can also be stress concentrators which, when combined with hydrogen molecules, act as crack initiation or propagation spots. As mentioned before, GB are one of the main contributors to HE as they serve as pathways for the hydrogen molecules to disperse and accumulate.

There are different types of GB: low angle (below 15 deg) and high angle (above 15 deg). Low-angle GB are subgrain boundaries and could almost be considered to be the same grain since their atomic configuration and orientation are mostly identical. High-angle GB are much more pronounced and play a much more significant role in hydrogen diffusion. Within the high-angle GB, they can also be separated by Special (or coincident site lattice (CSL)) GB ( $\sigma$  below 29) and Random GB ( $\sigma$  equal to or above 29). The Special GBs are characterized for having more structure and a lower energy [20]. In a study done by A. Oudriss et al., the effect of hydrogen was studied on Special and Random GBs [21] A few observations were made: In Special GBs, dislocations and vacancies accommodate their misorientation. These GBs are narrow and can often hold the hydrogen atoms more easily because of their high trapping site density. On the other hand, Random GBs are less structured and have higher excess free volume, which often helps hydrogen diffuse at a faster rate through the microstructure. Hydrogen diffusion could highly depend on the type of GB present, its amount, and its distribution across the microstructure.

All of these different defects allow the hydrogen atoms to accumulate and form high-pressure hydride clusters, which happen when hydrogen atoms start combining with the metal atoms, which can promote cracking when the material is under stress. As the hydrogen atoms reach these different sites, the electrons from these atoms start interacting with the electrons from the metal and start deteriorating the metallic bonds which reduces their ability to deform plastically and makes them brittle. All of these serve as trapping sites for the hydrogen atoms. Within the trapping sites, there are two types: reversible and irreversible [22]. In reality, all trapping sites are reversible but some take much longer than others and might even require a special treatment. The reversible trapping sites often are elastic fields, edge dislocations, and precipitates while the irreversible often are vacancies and dislocation cores. These are all found in the GBs.

Aside from defects in the microstructure, phase composition is another important factor affecting HE. With INC 718, the different phases present in the material (such as the austenitic  $\gamma$  phase, the  $\gamma'$  phase, and the  $\gamma''$  phase) can influence how the hydrogen atoms are distributed and where they get trapped as different phases may express different susceptibilities to HE. B. Kagay et al. investigated how the internal structure of Alloy 718, especially the presence of a specific type of particle  $\delta$ -phase at grain boundaries, impacts how susceptible it is to hydrogen embrittlement. [23]. They discovered that the material with the least amount of  $\delta$ -phase (under-aged condition) resisted hydrogen embrittlement the best. In contrast, the material with the most  $\delta$ -phase (high delta condition) was the weakest against hydrogen embrittlement and showed intergranular cracking. The study suggests that other factors like the size and amount of different phase types ( $\gamma'$  and  $\gamma''$ ) also play a role, along with the overall strength of the material.

### 2.1.3 HE and Mechanical Properties

As previously mentioned, everything that happens in the microstructure, the effect of hydrogen in metals, is reflected in the reduction in mechanical performance. Some of the mechanical properties that are affected include tensile strength, ductility, toughness, fatigue strength, and fracture toughness. These properties are affected for various reasons: (1) the presence of hydrogen atoms disrupts the connectivity and bond between the metal atoms and the grains, and (2) the high-pressure points in the microstructure created by hydrogen atom clusters make the material more susceptible to premature fracture. Xingfeng Li et al. investigated how hydrogen weakens the nickel-based superalloy IN718 by exposing it to hydrogen and measuring its strength and fracture behavior [24]. Examination of the fractures revealed that hydrogen creates voids at two main locations: 1) where slip bands intersect needle-shaped  $\delta$  phase particles within grains and 2) at the interface between the main metal phase and  $\delta$  phase particles along grain boundaries. The presence of the  $\delta$  phase at grain boundaries also encouraged cracks to travel preferentially between grains, as shown in Figure 2.4. The researchers propose that both hydrogen-enhanced localized plasticity and hydrogen-enhanced decohesion mechanisms contribute to the overall embrittlement of the alloy. Figure 2.3 shows the decline in mechanical performance of the studied samples.

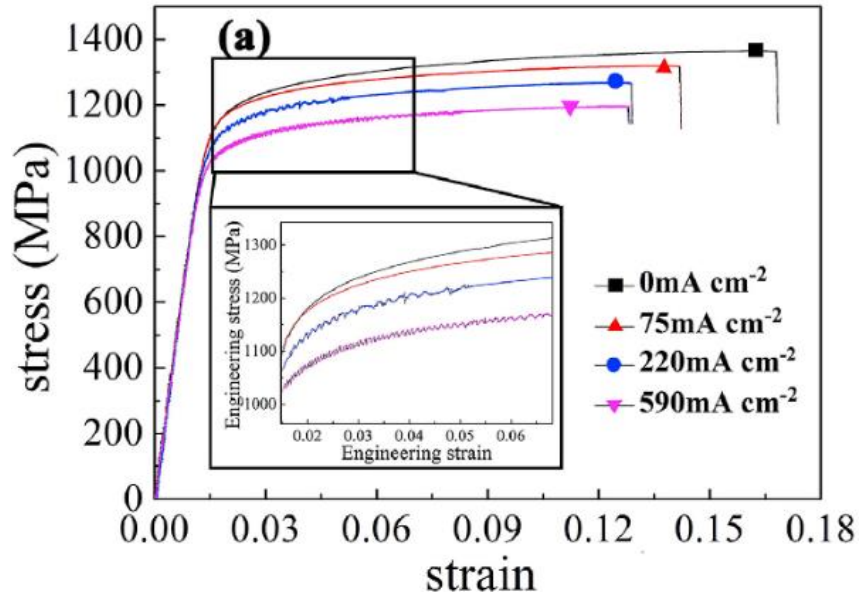


Figure 2.3: Stress-strain curves of IN718 alloy without and with hydrogen charging at  $0 \text{ mA cm}^{-2}$ ,  $75 \text{ mA cm}^{-2}$ ,  $220 \text{ mA cm}^{-2}$ , and  $590 \text{ mA cm}^{-2}$  [24]

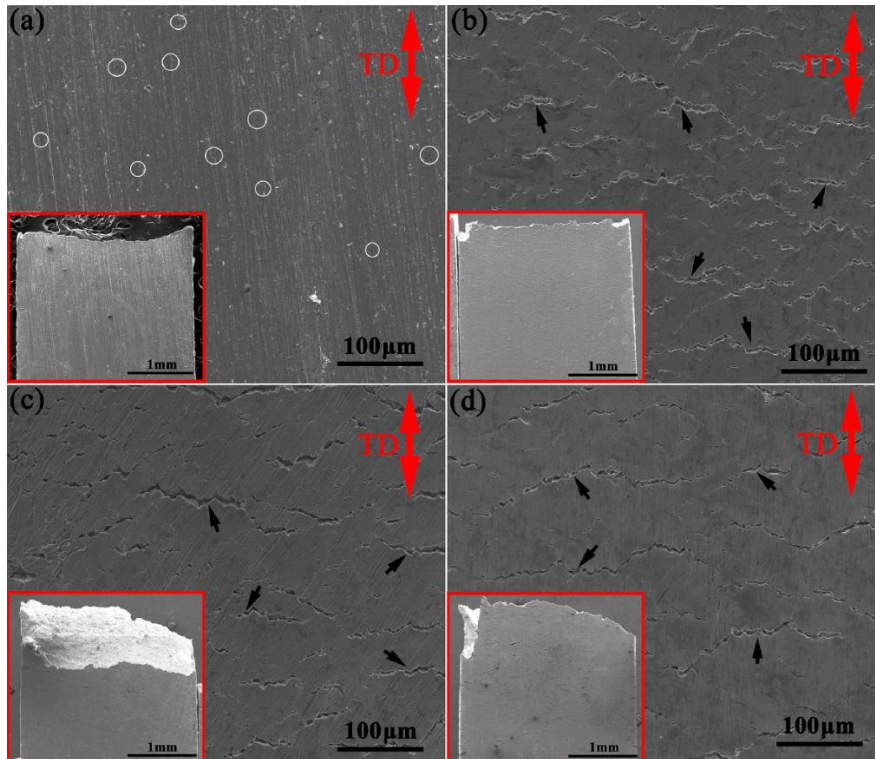


Figure 2.4: SEM images of tensile samples (a) hydrogen free; (b)  $75 \text{ mA cm}^{-2}$ ; (c)  $220 \text{ mA cm}^{-2}$ ; (d)  $590 \text{ mA cm}^{-2}$ . White circles indicating microvoids; Black arrows indicating hydrogen-assisted cracking [24]

#### **2.1.4 Other Factors**

When observing the environment in which a metal component operates, the level of susceptibility and damage done by HE is also affected by the conditions under which the component operates. Two of the main factors are temperature and pressure. In a review done by Jonathan A. Lee et al., they concluded that room temperature is often where most metals are most susceptible to HE as at lower temperatures, the hydrogen's mobility is much lower which reduces the diffusion through the metal, while at higher temperatures diffusion is considerably faster which reduces trapping [25]. In addition, they mention that it is very common for susceptibility to increase with higher hydrogen pressure.

#### **2.1.5 Mitigation Strategies**

There are many things that might help mitigate or prevent HE from occurring. Material selection is a big factor. If the application allows, a lower-strength metal could be utilized as they are less susceptible to hydrogen. Materials with higher percentages of Ni and lower percentages of C also work well [26]. Heat treatment or “bakeout” can be applied to the component post-plating [27]. Ceramic coatings such as  $\text{Al}_2\text{O}_3$  and  $\text{TiAlN}$  are some of the most popular and effective for HE prevention [28]. In addition, modifying the microstructure of the material can also be an effective solution to this problem. This can be done by applying heat treatments as they change the microstructure of the material, by adding alloying elements that could be beneficial (less susceptible), or by adapting or modifying the manufacturing method which is what this study aims to do by studying additive manufacturing.

## **2.2 ADDITIVE MANUFACTURING**

Additive Manufacturing (AM) is a manufacturing process in which a three-dimensional object is built (or printed) layer by layer. Generally, AM is characterized for allowing the design and manufacture of complex components; in other words, AM allows for geometrical freedom [29]. There are 7 process categories for AM: Material Extrusion, Material Jetting, VAT Photopolymerization, Binder Jetting, Directed Energy Deposition (DED), Sheet Lamination, and Powder Bed Fusion (PBF) [30].

### **2.2.1 Material Extrusion**

Material Extrusion: According to ISO/ASTM 52900, material extrusion is an additive manufacturing process in which material is selectively dispensed through a nozzle or orifice. This is an early AM technology invented in the late 1980s [31]. It is perhaps the most popular and accessible of all the AM technologies [32], [33]. Because of this fact, material extrusion is used for all kinds of purposes, from making recreational builds and prototypes to building functional parts [34], [35], [36]. Thermoplastics are the most common materials used in this technology [37]. Some of these thermoplastics include polyethylene, polypropylene, polyvinyl chloride, acrylonitrile butadiene styrene, polylactic acid, polycarbonate, and aliphatic polyamides [38]. Usually in this process, as shown in Figure 2.5, the filament (string of thermoplastic material) will be connected and heated by the nozzle before coming out in a liquid state and being deposited on the platform below. This process is repeated layer by layer until the final part is printed. These machines' most common working mechanism is the nozzle moving in the X & Y directions while the platform moves in the Z or vertical direction [39].

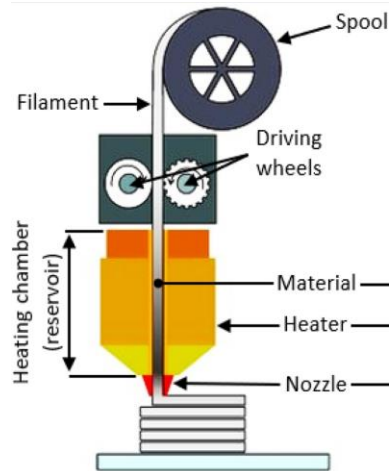


Figure 2.5: Schematic of Material Extrusion system [40]

### 2.2.2 Material Jetting

According to ISO/ASTM 52900, material jetting is an additive manufacturing process in which droplets of build material are selectively deposited. Similar to an inkjet printer, material jetting systems count on a printhead with small nozzles that dispense the droplets of a photopolymer, which will then get hardened under light. Layer by layer, the material is deposited. The technology, as shown in Figure 2.6, has a curing system, usually a UV light source, that will cure the droplets as they are being deposited which also ensures that the layers bond together [41]. Material Jetting can deliver realistic models and prototypes because of its high-dimensional accuracy, smooth surface finish, and the fact that many colors can be used during the building process [42], [43], [44], [45], [46].

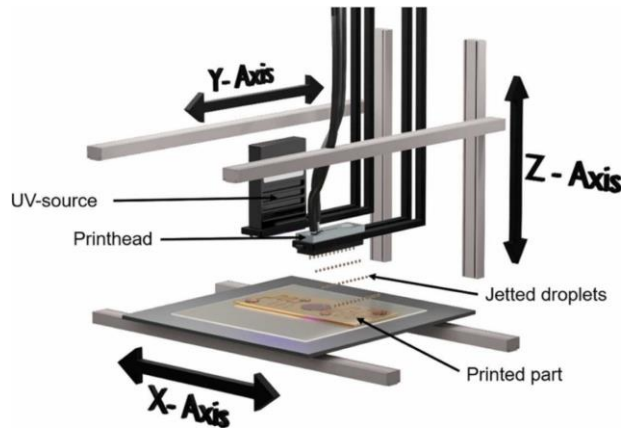


Figure 2.6: Schematic of Material Jetting system [47]

### 2.2.3 VAT Photopolymerization

According to ISO/ASTM 52900, vat photopolymerization is an additive manufacturing process in which liquid photopolymer in a vat is selectively cured by light-activated polymerization. This process, schematic shown in Figure 2.7, usually has a vat that contains all the liquid photopolymer resin, the printer then directs a light source, usually a UV laser, to selectively harden targeted areas of the resin vat. After this, the building platform lowers to grab more resin and the process is repeated layer by layer. After printing, as a post-process, the final part is taken out of the vat, the excess resin is removed, and the part is further cured in a UV light chamber. This technology is characterized by its high resolution, being able to build very detailed parts and high-dimensional accuracy [48], [49].

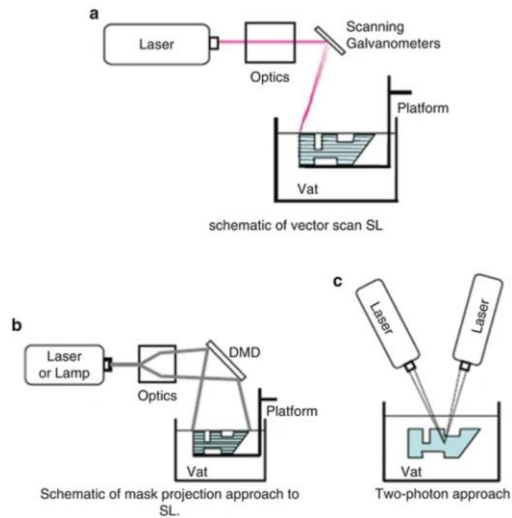


Figure 2.7: Schematic of Vat Photopolymerization systems [50]

### 2.2.4 Binder Jetting

According to ISO/ASTM 52900, binder jetting is an additive manufacturing process in which a liquid bonding agent is selectively deposited to join powder materials. A schematic is shown in Figure 2.8. This process is similar to Material Jetting as they both have a printhead with small nozzles that dispense a liquid. In binder jetting, the liquid bonding agent is dispensed into a powder bed so that the individual particles can be bonded together and form a semi-solid or “green” part. Usually, a thin layer of metal, ceramic, or sand powder will be spread throughout the printing area, the printhead will then dispense the binder in the desired areas, the whole layer will then be cured by a heat source, and the whole process will be repeated layer by layer. The green parts coming out of this process will then have to be further cured and sintered to achieve a fully dense state. The Binder Jetting process can be fast but it often requires post-processing which can mess with the dimensions and the surface finish of the part [51].

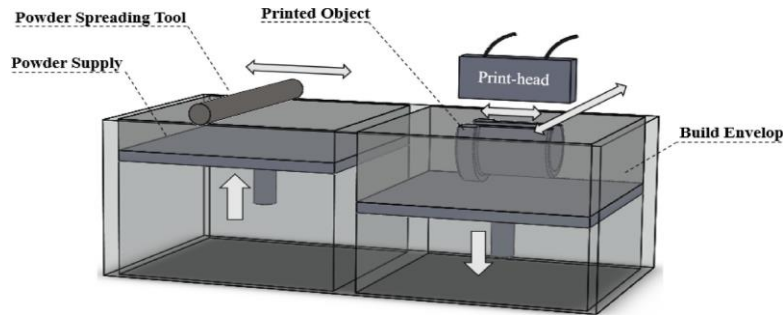


Figure 2.8: Schematic of Binder Jetting system [52]

### 2.2.5 Directed Energy Deposition

According to ISO/ASTM 52900, directed energy deposition (DED) is an additive manufacturing process in which focused thermal energy is used to fuse materials by melting as they are being deposited. DED uses a concentrated energy source, it can be an electron beam, a laser, or a plasma arc, to melt the material coming out of the nozzle. A schematic is shown in Figure 2.9. The material could come in two forms: a wire or powder. The process works layer by layer. The heat source and nozzle move together to melt the material precisely as it is being deposited in the correct areas. These machines will often operate under a controlled environment with reduced oxygen to reduce the chances for oxidation which ensures a proper weld or bonding between each of the layers [53]. DED is especially useful for building large components, it has high rates of deposition and can be also used to repair components [54].

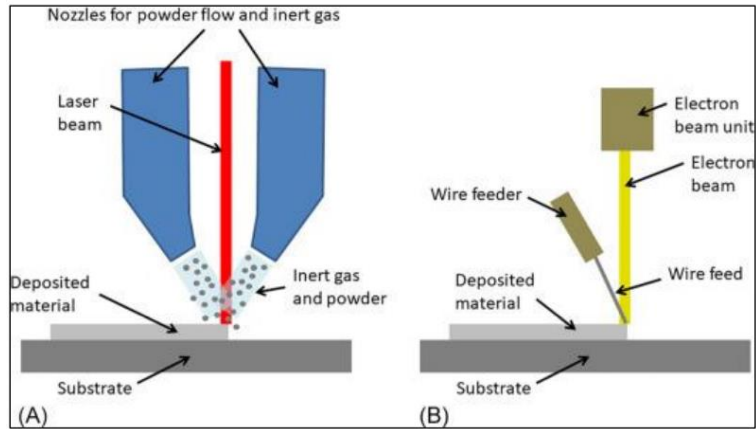


Figure 2.9: Schematic of a DED system. A) laser and powder and B) electron beam and wire [55]

### 2.2.6 Sheet Lamination

According to ISO/ASTM 52900, sheet lamination is an additive manufacturing process in which sheets of material are bonded to form an object. This works with various materials, such as paper, polymer films, or metal foils, and these sheets are pre-cut based on the desired layer profile. Each layer sheet is bonded with the previous one in a different way depending on the material. For metal sheets, the bonding mechanism is applied pressure with ultrasonic welding. The high pressure and vibration applied between the sheets bond them together. The shape of the object and the sheet can either be cut after or before bonding, depending on the specific system. These machines can be cheaper and faster than other AM systems, and can also manufacture a large number of materials, however, sheet lamination does not produce high-resolution parts and is often used for prototyping rather than high-precision end-use components [56]. A schematic is shown in Figure 2.10.

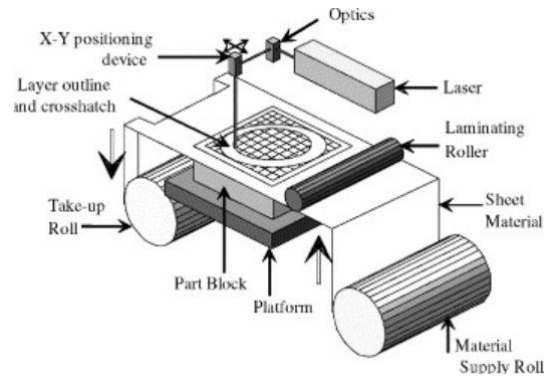


Figure 2.10: Schematic of a Sheet Lamination system [57]

### 2.2.7 Powder Bed Fusion

According to ISO/ASTM 52900, powder bed fusion (PBF) is a process category in which thermal energy, delivered by a laser or electron beam, selectively fuses regions of a powder bed. PBF industry has by far the largest market share when considering other AM metal technologies, as shown in Figure 2.11.

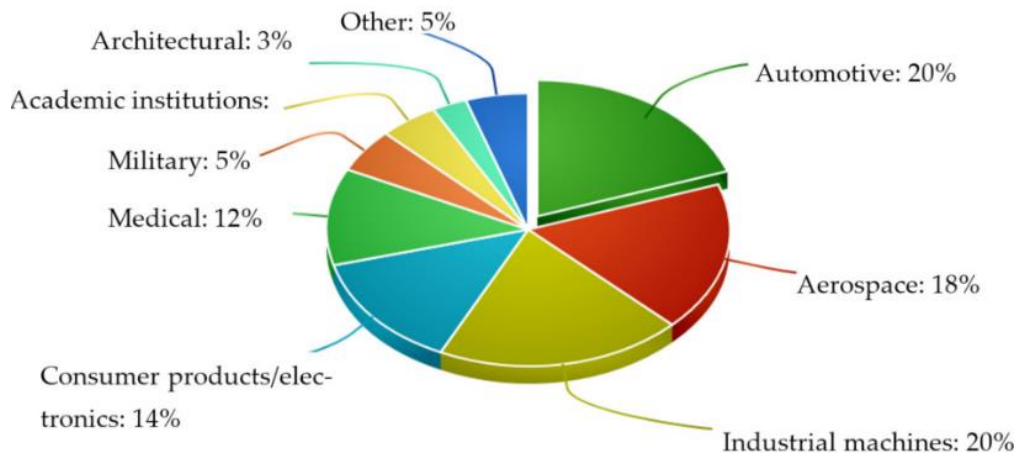


Figure 2.11: Market share of metal AM technologies [58].

Within PBF, there are two main categories: Laser Powder Bed Fusion (L-PBF) and Electron Beam Powder Bed Fusion (EB-PBF). In these processes, a thin layer of powder is first

deposited from the hoppers onto the build platform by some rolling or raking mechanism; a power laser or electron beam then acts as the heat source to scan the powder bed and selectively melt the particles together according to the component shape. The build platform will then lower slightly so a fresh new layer of powder can be deposited, and the process repeats after every layer to complete the entire build. Depending on the technology, the system will operate under a controlled environment, such as an inert gas, or it will operate under a vacuum. PBF is a well-established process and produces parts that often have a high-dimensional accuracy and are suitable for end-use applications [59]. However, they can be expensive relative to other manufacturing methods and often require post-processing, such as heat treatments, to relieve the internal stresses induced during the build [60], [61].

In this thesis, the main focus will be set on Electron Beam Powder Bed Fusion (EB-PBF), also called electron beam melting (EBM), which is a branch of PBF. This technology was invented in Sweden by Arcam AB, and later purchased by General Electric [62], [63]. However, all of the work presented in this thesis was done in a Freemelt system (Freemelt ONE), which is another company that makes open-architecture EBM 3D systems [64]. Their system allows for more user control and print customization compared to other traditional EBM systems [65].

### ***2.2.7.1 Advantages and Disadvantages of EBM***

When using EBM to manufacture any component, it is clear that this technology has its advantages and disadvantages when compared with other AM technologies and traditional manufacturing methods. When contrasting EBM against other AM technologies it can be seen that EBM can produce high-density components, near net shape. This translates to high tensile strengths, comparable to wrought metal components [66]. Complex parts with internal channels

and overhangs with minimal support structures can be created with this technology more easily than others [67], [68]. A wide range of materials can be used to print with EBM, including some reactive and refractory metals [69]. One of the downsides is the fact that the EBM process usually has slower build speeds (depending on the systems being compared), which could make it less appealing when considering high output or high volume production. The cost per part is usually higher, again, this depends on the technologies being considered. Also, there are other AM methods with much smoother surface finishes which might be important depending on the application.

Now, when comparing EBM with traditional manufacturing methods, there are major pros and cons to consider. As EBM is an AM technology, this means an inherent design freedom when creating new components. Complex geometries can be created and printed which might be extremely difficult or even impossible to manufacture using traditional subtractive methods. Material waste is also a big issue with subtractive manufacturing methods; high amounts of material are thrown into waste and are hard to recycle. EBM has the capability of only using/melting the material needed to build the desired component and almost immediately reusing any powder around the print, creating very little waste. Also, EBM is a great alternative to creating legacy components [70]. These legacy components are usually replacement parts that are no longer in production. This creates an opportunity for EBM to produce low-volume, customized parts for multiple industries. Finally, as freedom of design exists on AM, this gives the opportunity to consolidate complex assemblies made up of multiple components into one single part. Whereas these capabilities make EBM attractive and suitable for many applications, traditional manufacturing methods still have many disadvantages. There is an even wider range of materials available for well-established traditional processes. Also, EBM-printed parts often require post-

processing steps such as heat treatments, which make the cost to manufacture even higher [71]. Finally, all EBM systems have relatively small and limited build chamber size which inevitably restricts the size of the components that can be printed. Overall, EBM can create components with favorable properties but the process presents some limitations. It is important to consider the application, cost, size, and other things when deciding how a component will be manufactured.

### ***2.2.7.2 EBM Overview***

EBM is a technology that, as its name implies, works by using an electron beam source to selectively melt the metal powder. This technology can print a wide variety of materials but they all have to be conductive to dissipate the electric charge from the electron beam interaction with the powder. The best type of powder particle morphology is spherical as they can easily flow across the powder bed and ensure a more even distribution [72] Several powder manufacturing methods exist; spherical powder is manufactured either by gas atomization or plasma. Normally, the particle sizes preferred for EBM processes are 45-105 microns in diameter.

The electron beam used comes from a diode-type source with a CO<sub>2</sub> laser-heated cathode. A schematic of an EBM system is shown in Figure 2.12. The CO<sub>2</sub> laser hits and heats the cathode, which causes it to emit electrons. These electrons are directed with the diode and focused into a narrow and precise beam by beam-forming coils in the column. These beam-forming coils are electromagnetic components that can focus the electrons from the initially divergent beam and dictate its trajectory down to the building area. The beam's power ranges from 0-6 kW. This whole process occurs under a vacuum. Vacuum levels are kept at 10<sup>-6</sup> hPa (mbar) in the building chamber and 10<sup>-7</sup> hPa (mbar) in the column. Printing under vacuum allows electrons to follow their path without resistance, making it a more efficient process; aside from this, a vacuum environment

helps prevent oxidation that would normally happen due to the high temperatures, allowing the printing material to maintain its quality and chemical composition, and allowing the electron beam to penetrate deeper into the powder bed which creates a better fusion between each of the layers [73]. If this process happened under a controlled gas environment, as in LPBF, the electron beam would collide with the other gas particles. The EBM machine used for the fabrication of all INC 718 samples examined in this study was a Freemelt One. These machines are mainly suitable for small builds meant for research & development purposes [74]. The building chamber has dimensions of 100 mm H x 100 mm Ø which inevitably limits the desired print size to that envelope.

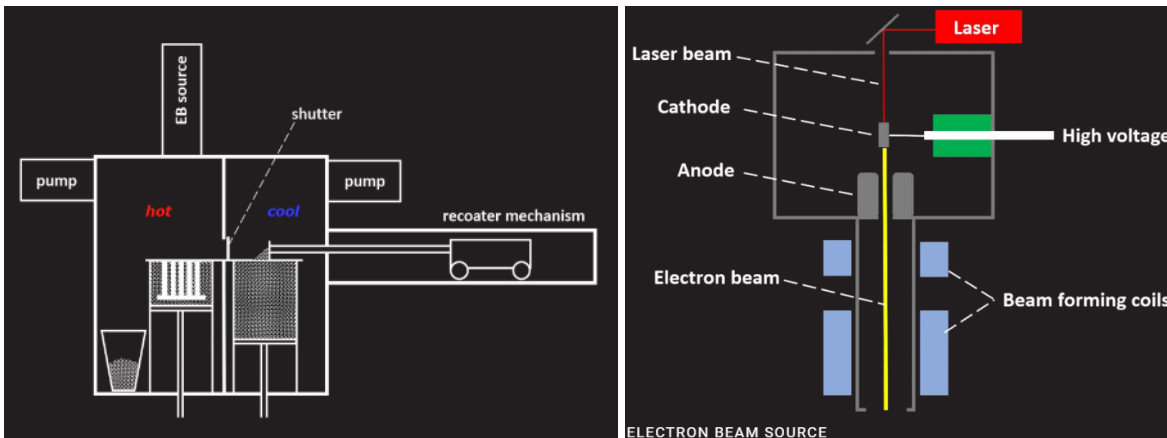


Figure 2.12: Schematic of a) overall Freemelt ONE EBM system and b) EB source [74]

This whole process starts with a Computer-Aided Design (CAD) model, which is the digital version of the object that needs to be printed. This CAD model is then sliced or codified in a specific software so that the EBM machine can process it and later print it. After the CAD file has been sliced and all parameters have been set, then the machine setup begins. This process usually consists of sieving then metal powder through a specific mesh size so that the particle sizes are controlled; bigger particle sizes could negatively affect the printing process.

The particle sizes used for EBM processes usually range between 50-120 microns. It is important to have this range of sizes so that the powder bed remains as fully packed or as dense as possible during the printing of each layer; fully packed layers reduce the risk of porosity in the print [75]. The sieved powder is then placed in the powder tank inside the machine. After this, the build plate, usually a circular-shaped steel plate, is then leveled. Leveling the plate ensures it will not later interfere with other components, such as the raking mechanism, potentially ruining the entire process. The plate is then lowered by a specific distance to account for thermal expansion when heated, which also prevents any interference. Finally, the machine can be put into a vacuum so that all air is extracted from the chamber and column. After reaching proper levels of vacuum, mentioned above, the print can then begin.

The process starts with a general preheating step. This works by activating the e-beam and defocusing it so that it delivers a specific flow rate of energy to the entire build area so it can be preheated and reach a specific temperature before printing. This is done to ensure a high-temperature printing environment and to sinter the powder particles around the plate, which will give the plate a certain level of stability and prevent it from moving from its place. As discussed above, the EBM process works at high temperatures at all times, usually maintained above 900 C depending on the material. This happens for several reasons [76], [77]. Keeping a high environment temperature reduces the thermal gradient between the volumes of powder that is being melted and its surroundings. This affects the cooling rates of each layer. Cooling rates can then affect the entire microstructure of the print which then affects its mechanical properties. Slower cooling rates can help reduce the amount of residual stresses left in the print [78]. Aside from all of this, higher printing environment temperatures enhance the powder flowability which ensures an even powder distribution in the printing area and improves the adhesion between layers.

After the plate has reached a certain temperature in this first general preheating step, the raking mechanism takes powder from the powder tank and evenly spreads it across the building platform, leaving a thin layer of powder across the plate. A second, more localized, preheating begins around the specific areas of the actual shape of the print. As with the first general preheating, this localized preheating step happens by defocusing the beam and applying energy to a large, selected area. The next step is melting. The beam is highly focused and selectively melts the shapes of the actual component being built. Usually, the beam will first melt the hatch area of the whole shape, the inside area, and then proceed to melt the contour of it. The raking, preheating, and melting steps are then repeated continuously until the entire component is built. Finally, the machine must be let cool down on its own, maintaining the vacuum environment to prevent oxidation, before it can be opened and the print is taken out.

### ***2.2.7.3 Parameters EBM***

Again, EBM involves numerous parameters that alter a specific aspect of the printing process. Some of them are beam power, beam focus, scan speed, layer thickness, scanning strategy, preheating, etc. It is important to define the values for each of these parameters before the print as they can all affect a different aspect of the print and consequently affect the microstructure and mechanical properties of the part [79]. Here is a list of the most common parameters used along with a brief description of what they do:

- Power: power at which the beam will be generated, measured in (W). Ranges from 0-6000 W.
- Jump Length: used to jump from one pixel to another in the x & y directions when moving to another row. Measured in (mm).

- Spot Size Percent: the spot size percent is measured from 1-100%. This spot size percent represents the beam radius. The most focused is achieved at 1% whereas the most defocused beam is achieved at 100%.
- Beam size: diameter of the beam at the 1% spot size percent. Measured in (mm).
- Current: current applied to the beam. Measured in (mA).
- Spot Dwell: Amount of time, measured in ( $\mu\text{s}$ ), each beam spot will stay at a specific location.
- Energy per Spot Area: the amount of energy that is applied by the beam into a specific area. Measured in ( $\text{J}/\text{mm}^2$ ).
- Mesh Size: this determines the size of each pixel where the beam is positioned.
- Number of Spots: total number of spots that will cover the area of your print. This is more of a measurement caused by other parameters.
- Layer Height: the height of each layer that will be spread across the build platform by the raking mechanism, measured in ( $\mu\text{m}$ ).
- Start Heat: the temperature under the build plate that must be reached before starting the actual print steps. Usually, a slow energy rate is applied to ensure the general area around the plate gradually reaches a high temperature, which ensures a better process. Measured in (C).
- Preheat: number of repetitions, equivalent to an amount of time, the preheat process will be done on the printing area (on the powder bed) before each melt step. This step is done to ensure the whole new layer of fresh powder reaches a certain temperature and is preheated, before melting.
- Scanning Strategy: this determines the path the beam will follow to perform the melting step. this parameter can be highly influential in the microstructure of the entire part.

#### ***2.2.7.4 Scanning Strategies***

As previously mentioned, the scanning strategies that are chosen for a print are highly influential to the microstructure of the final part which later dictates the properties of it. One of the various scanning strategies can be chosen when for a specific print depending on the desired outcome. For this thesis, a single-directional shifted scanning strategy was chosen. This strategy was chosen as it is a type of what is called a spot-melting scanning strategy, which is capable of delivering certain kinds of microstructures. Andrew T. Polonsky et al. investigated how different melting strategies in additive manufacturing affect the final structure of Inconel 718 [80]. They found that using a focused spot melt technique with slower heat delivery promotes the formation of equiaxed grains. Conversely, a continuous line scan (raster melt) with faster energy input creates elongated columnar grains aligned with the scan direction. This study highlights the importance of scan strategy selection for controlling or predicting the final microstructure and properties of the manufactured parts.

#### ***2.2.7.5 Microstructure and Mech Properties on EBM***

Each manufacturing method has different processes to create a component. These differences in the processes alter the material's microstructure in different ways. When 3D printing something using an EBM machine, there are typical or general microstructural characteristics that can be seen in the components in their as-built state, meaning with no further post-processing techniques. When analyzing metals printed with EBM, it is common to observe elongated or columnar grains [81]. These grains grow in a vertical form, perpendicular to the build plate and following the build direction due to the heat flow moving in that same direction. These components often exhibit near-net-shape densities, meaning they can achieve very high densities with minimal

porosity in them (the printing parameters also play an important role in the density of the components) [82]. As mentioned before, the EBM process occurs under high temperatures, which helps with proper particle bonding and helps with the density of the part. Again, residual stresses are also an inherent part of the printing process. The relatively rapid melting and cooling phases of the material can cause residual stresses as the material expands when heated and contracting when cooling. As different layers can experience this expansion and contraction multiple times, stresses are created in the microstructure.

#### ***2.2.7.6 Mechanical Properties EBM***

These general microstructural features translate into the printed samples' mechanical properties. High densities translate into high tensile strength, relative to the material being printed, allowing them to withstand high loads and stresses, especially with INC 718. As mentioned before, INC 718 is a precipitation-hardened alloy which gives it its ductility; when printed with EBM, this ductility might be slightly lower due to the residual stresses in the samples. As ductility lowers, elongation also suffers. The columnar grain structure creates a phenomenon called anisotropy which gives the components favorable tensile strength and elongation when tested in the vertical (perpendicular to the build platform) direction. As with other AM technologies, EBM creates a component layer by layer. These layers form a rough texture around the component, called surface roughness. This can be a significant factor when the components are meant for applications requiring wear resistance. Residual stresses due to the rapid heating and cooling cycles can cause high-stress points and later crack initiation spots [83]. INC 718 printed samples normally retain their high temperature and corrosion resistance.

### **2.2.7.7 Post Processing on EBM**

Very often, EBM parts undergo post-processing to correct porosity, relieve residual stresses, and meet other industry or application-specific requirements [84], [85], [86]. These post-processing methods usually begin with some kind of heat treatment. Some of the most typical heat treatments EBM components usually undergo are Hot Isostatic Pressing (HIP), Solution Treatment (ST), and Aging. The HIP process uses high pressure and high temperature to close all of the voids or pores within the component. In the process of doing this, HIPing may also have an effect on grain size, homogenizes the microstructure by redistributing its precipitates, and dissolves some certain phases. In the context of INC 718, HIPing usually dissolves gamma and delta phases due to their lower solvus temperatures (780-925 °C and 1020 °C respectively) while keeping carbides (solvus temp. 1290 °C) [87]. This causes the material to decrease in tensile strength and increase its elongation and fatigue life while the other heat treatments, ST and Aging, serve to bring out the desired phases (gamma phases) of the material [88]. Aside from this, some applications might have certain requirements that could require machining to achieve tight tolerances and better surface finishes. Overall, post-processing techniques help to increase the integrity of the components, most times positively altering their mechanical performance, and preparing it for their specific application. In this paper, only the effect of HIPing will be studied.

### **2.2.8 AM and HE**

AM has extensively been studied for many applications but lacks research on its relationship with HE. This area has recently gained more attention as more AM techniques and materials are being studied, but there is a clear lack of information regarding the effects of HE on INC 718 parts manufactured by EBM. Still, studies performed on other materials can provide

valuable insight into AM-HE relationships. As an example, Ju Yao et al. wrote a review on the research done on AM and HE [89]. In it, they explain that research on HE in additively manufactured (AM) Ti-6Al-4V parts (LPBF and EBM) shows conflicting results compared to traditionally made parts. LPBF's microstructure might make it more prone to HE than EBM, and HE susceptibility in LPBF itself might depend on printing direction. Also, opposing views exist when studying EBM parts vs wrought parts, with some studies suggesting better HE resistance for EBM and others finding the opposite. This inconsistency highlights the need for further research to clarify how HE affects AM parts compared to traditional methods. As mentioned before, there is a lack of research focusing on INC 718, still, there are a few studies published. As an example, Naveen Karuthodi Mohandas et al. examined how hydrogen gas affects LPBF INC 718, comparing it to traditionally manufactured INC 718 [90]. Although all samples became brittle with hydrogen exposure, the heat-treated AM material showed much less embrittlement (64% lower) despite its higher strength. This is due to the anisotropic microstructure behavior caused by 3D printing. The elongated grains confine hydrogen embrittlement to a narrow zone along the printing direction, unlike the uniform embrittlement seen in conventional material. While both types of INC 718 are susceptible to hydrogen embrittlement, the AM process creates a strategic advantage as the microstructure offers the potential for designing components where hydrogen exposure is a concern. This study shows that AM could be advantageous when manufacturing components to control their microstructures and thus influence their susceptibility to HE.

### **2.3 INCONEL 718**

As mentioned above, the material that was used for these experiments is INC 718. This material is considered to be a superalloy given it is a nickel-based alloy with strengthening

precipitates and can maintain its strength and mechanical properties at elevated temperatures (exceeding 700 deg °C), exhibit good performance in corrosive environments such as oxidation, hot gases, and other specific chemicals, and resist deformation under stress and high temperatures which ensures they can keep their original shape and function in demanding applications; summarized, this material exhibits excellent strength and mechanical properties and high temperature, corrosion, and creep resistance [91], [92, p. 718]Table 1 shows this material's chemical composition, and Figure 2.13 shows its performance against temperature compared to other metals.

Table 1: Chemical Composition of Inconel 718 [93]

<b>Material</b>	<b>Percentage Range (wt%)</b>
Nickel	50-55
Chromium	17-21
Iron	Balance
Columbium	4.75-5.5
Molybdenum	2.8-3.3
Aluminum	0.2-0.8
Titanium	0.65-1.15
Manganese	0.35 max
Silicon	0.35 max
Boron	0.006 max
Carbon	0.08 max
Sulphur	0.15 max

Magnesium	Residual
-----------	----------

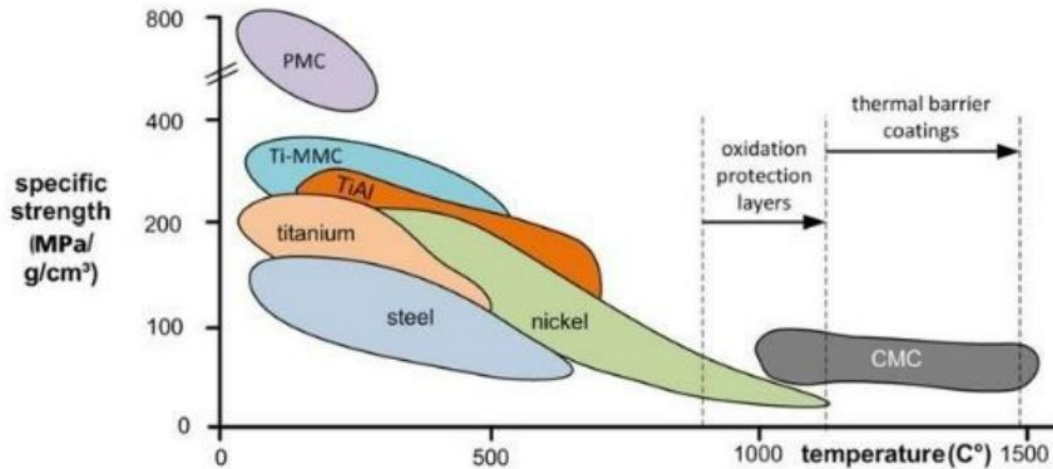


Figure 2.13: Materials strength at different temperatures [94].

These features make it favorable for multiple industries such as aerospace, oil & gas, energy generation, chemical processing, and others where the extreme environments require the properties that INC 718 has. The aerospace industry is often in need of components such as turbine blades, discs and some afterburner components that are in constant exposure to extreme environments where they might experience high temperatures, be subjected to high cyclic loads and corrosive environments [95]. The oil & gas industry is often in need of components such as downhole tools, pipelines, and subsea equipment that are subjected to corrosive chemicals, constant stress and wear, and high pressures [96]. In industries where chemical processing is needed, components such as pressure vessels and valves are manufactured and need to withstand environments where corrosive chemicals might be used [97]. Despite all of the material's positive properties, or perhaps because of them, INC 718 is not considered to be an easy material to manufacture through traditional methods [98]. Manufacturing methods such as forming,

machining, molding, and joining are considered to be traditional manufacturing methods that are widely used across many industries because due to a large number of years they have been present, they have become reliable and low-cost, especially when intended for mass production. However, it is difficult to manufacture INC 718 through these methods because of several aspects: (1) the material's high strength and hardness make it difficult to machine and can wear out the used tools faster. (2) The material shows work-hardening, which causes it to become harder and, therefore, more difficult to work with. (3) Because of its elasticity, the material can experience springback by trying to return to its previous shape or form. (4) Since the material is high temperature resistant, certain forging processes might need to use a lot of energy to work it. Nevertheless, AM offers new manufacturing options. INC 718 could be additively manufactured or "printed" using multiple AM technologies such as DED, LPBF, and EBM, but for this scope of work, EBM was the selected manufacturing method. As mentioned before, EBM provides a better opportunity to control the microstructure of whatever is being printed more than other technologies because of how the process works (slower cooling, less chance of contamination, vacuum environment, and wide range of parameters).

When trying to understand this material's relationship with HE, it is important to first look at its performance compared to other materials and then look deeper at the microstructure of the material. Carbon steels and high-strength steels are highly susceptible to HE due to their microstructure; several phases, like ferrite and pearlite, can form pathways for hydrogen atoms to penetrate and cause embrittlement [99]. Steel is the most commonly used material to build components that are used for keeping storage hydrogen due to the cost-effectiveness of the material, good mechanical strength and durability, and the fact that there are vast, effective, and well-established methods to manufacture it. The most common type of components that are

currently made from steel are highly pressurized tanks (to carry the hydrogen) and smaller components such as pressure vessels, valves, and fittings. However, there are no studies where different materials' susceptibilities to HE are compared.

### **2.3.1 Inconel 718 Microstructure**

Now looking deeper into the microstructure of INC 718, this material usually consists of a nickel matrix with strengthening precipitates like gamma prime ( $\gamma'$ ) and gamma double prime ( $\gamma''$ ) and includes a delta ( $\delta$ ) phase [100], [101]. The material can also often display laves and niobium carbides (NbC). Now, depending on the solidification (cooling rate) of the material, the morphology, placement, and size of these precipitates will be affected. Niobium carbides are often seen as a favorable outcome, while laves are often seen as a negative one because of how they affect the properties of the material [102]. Now, the microstructure of any material will inevitably change with different manufacturing methods. When manufactured using EBM technology, INC 718 often exhibits columnar grains growing in the direction of heat extraction known as the build direction. It normally contains the same precipitates,  $\gamma'$  and  $\gamma''$ , as shown in Figure 2.14, although their arrangement could vary depending on the processing parameters. As mentioned before, EBM builds will often exhibit a strong texture towards the build direction which can then lead to anisotropic behavior. L.E. Murr explains how the EBM process affects the internal structure of nickel-based superalloys like Inconel 625 and 718 [103]. EBM creates unique microscopic features within the printed metal which include elongated, aligned internal structures called "precipitate architectures," which tend to form in the same direction as the printing process.

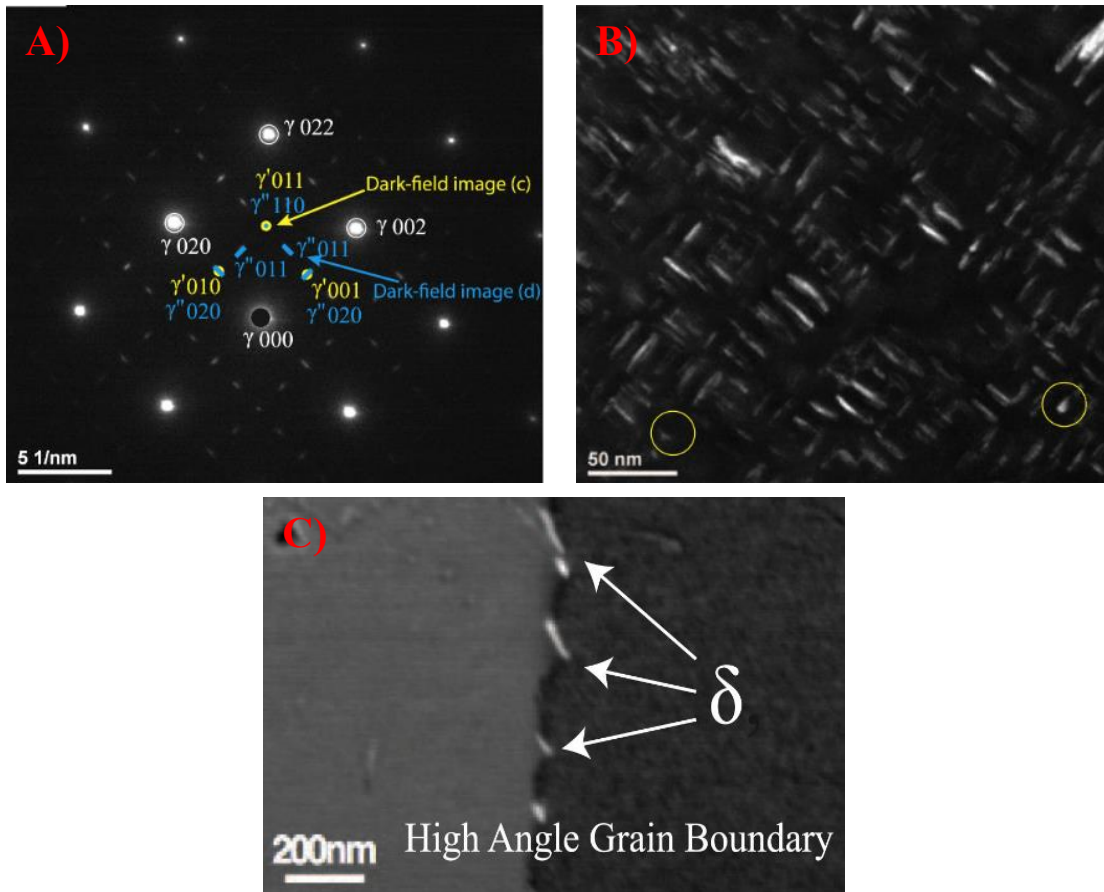


Figure 2.14: (A) TEM diffraction pattern image of [001] zone of  $\gamma$  matrix exhibiting  $\gamma'$  and  $\gamma''$  superlattice reflections; (B) TEM dark-field image using the  $\gamma''(110)/\gamma'(011)$  diffraction spot; (C) Image showing  $\delta$ -phase along high-angle grain boundaries [81].

The exact type and orientation of these  $\gamma''$  precipitates depend on the specific alloy being printed. For instance, Inconel 718 forms disc-shaped precipitates along  $\{1\ 0\ 0\}$  planes. Additionally, EBM creates elongated grains with low-angle boundaries throughout the material. The study suggests that by carefully adjusting the beam and scanning parameters (beam radius, scan spacing, and scan velocity) of the EBM machine, it might be possible to control these internal structures and potentially influence the final mechanical properties of the 3D-printed nickel alloy part.

The fact that INC 718 is a precipitation hardenable alloy means that those precipitates act as barriers to the movement of dislocations within the metal's microstructure which makes the material stronger and, simultaneously, those same precipitates can then act as barriers to hydrogen diffusion, offering some resistance against HE [104]. In general, when the precipitates are well distributed in the microstructure, the precipitates tend to act as trapping sites for hydrogen atoms and prevent them from reaching grain boundaries where they would cause more damage by starting the embrittlement process. Precipitates like  $\gamma'$  are often considered as beneficial while the  $\delta$ -phase usually facilitates the hydrogen diffusion towards grain boundaries. G. C. Obasi et al. studied the effect of different microstructures in Nickel alloy and found that  $\delta$ -phases tend to increase the material's susceptibility to HE [105].

### 3. Chapter 3: Materials and Methods

#### 3.1 POWDER FEEDSTOCK CHARACTERIZATION

Before printing, the powder was first analyzed and characterized. The chemical composition of the powder is previously shown in Table 1. A particle size distribution test was performed, shown in Figure 2.15, using a Retsch Camsizer X2. Results show 10% of powder particles are below 58.7  $\mu\text{m}$  in diameter, 50% of powder particles are below 70.0  $\mu\text{m}$ , and 90% of powder particles are below 84.8  $\mu\text{m}$ .

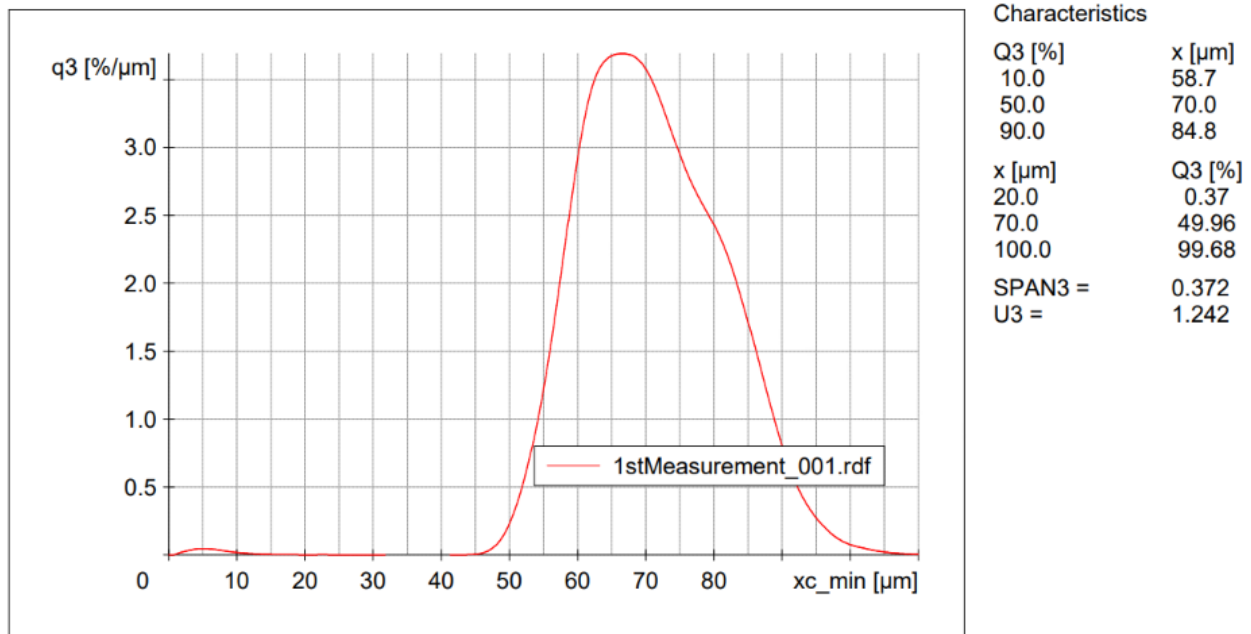


Figure 2.15: Powder Size Distribution Graph.

#### 3.2 EBM MANUFACTURING

As always, the printing process begins by creating CAD models, in this case created in Autodesk Fusion 360. These are shown in Figure 2.17. They are later exported to a Freemelt proprietary slicer software which creates a code specific for the machine to read and execute so that the correct beam paths are followed to print the desired shape. After the file is sliced, the user is allowed to enter the desired parameters and scanning strategies, as shown in Figure 2.16, by

using Pixelmelt, another Freemelt proprietary software. This file has to be manually inputted to the machine before every print.

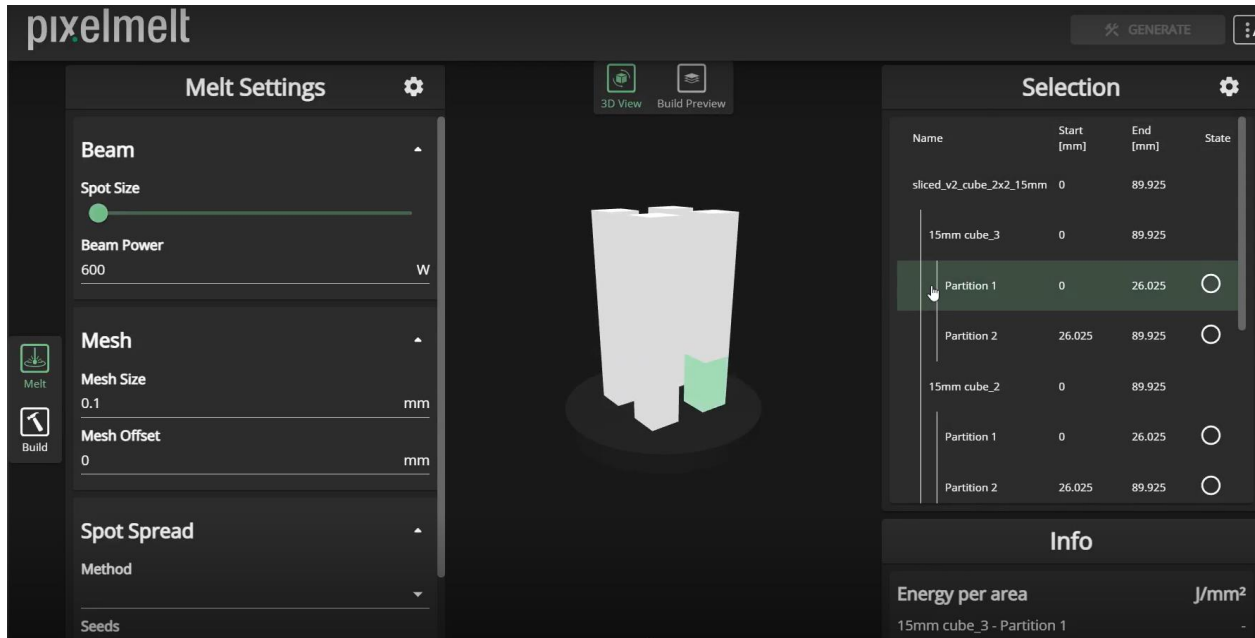


Figure 3.1: Pixelmelt program interface.

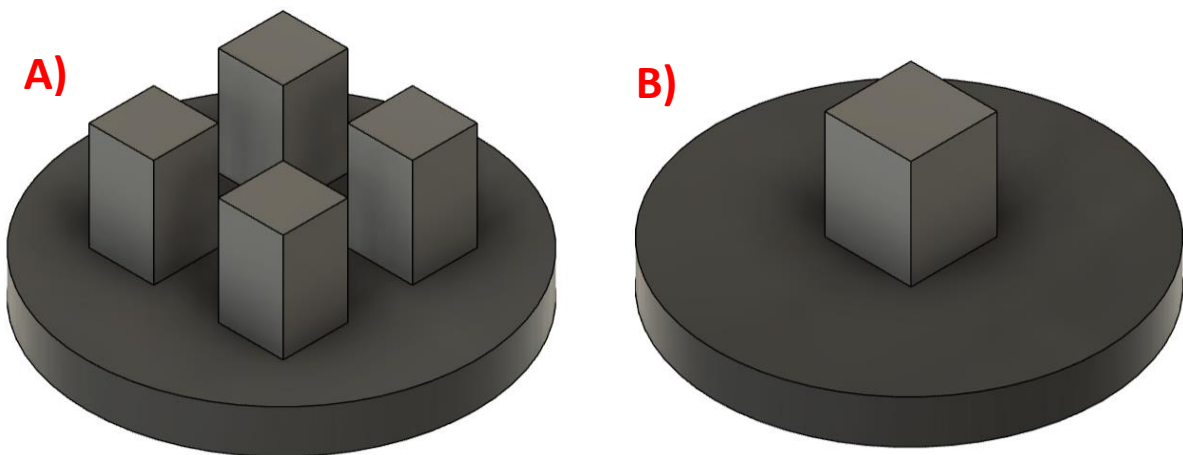


Figure 3.2: CAD models of A) Rectangular prisms, 4 Samples: 15 x 15 x 25 mm. B) Rectangular prism, 1 Sample: 20 x 20 x 25 mm.

All INC 718 samples studied in this thesis were manufactured, or printed, in a Freemelt One system. In this system, the electron beam comes from a diode-type source with a CO2 laser-heated cathode, as mentioned before. The beam's power has the capability of operating in a range from 0-6 kW. The machine is also capable of reaching high levels of vacuum,  $10^{-6}$  hPa (mbar) &  $10^{-7}$  hPa (mbar), which helps with the quality of the print. The building is relatively small compared to other EBM systems with dimensions of 100 mm H x 100 mm Ø. This system can manufacture components at over 1100 C which allows it to print with a wide variety of materials, also discussed previously in more detail in the literature review section of this document.

### 3.2.1 Parameters

The rectangular prism samples that were printed were initially computer-modeled and then sliced and processed using the Pixelmelt software which is a proprietary software of the Freemelt company. In this software, the main parameters for the print were set so that once the file is saved, it can be transferred to the main computer of the Freemelt One system. As mentioned before, Single Directional Shifted scanning strategy was used to build the samples. In Table 2, the parameters used for this scanning strategy are shown. These parameters are considered to be the most influential in the printing process as they directly affect the microstructure and mechanical properties.

Table 2. Stochastic and Single Directional Shifted Parameters

<b>Parameters</b>	<b>Single Directional Shifted</b>
Starheat	1050 °C
Preheat	200 reps

Power	360 W
Jump	X_10 px   Y_10px
Spot Size Percent	1%
Beam Size	~0.250-0.280mm
Current	6mA
Spot Dwell	250us
Energy Per Spot Area	9J/mm <sup>2</sup>
Mesh Size	0.1
Number of Spots	22500
Layer Height	0.075

After the printing process, the machine is at a very high temperature and has to be cooled down at ambient temperature but still under vacuum. The cooldown process takes around an entire day. After the chamber has reached ambient temperature, the machine can be open and the samples can be taken out by carefully removing all the surrounding sintered powder (seen in Figure 3.3 A and B). The samples had to be sectioned off the build plate by using a bandsaw cutter as the printing process usually makes them strongly adhere to it (as seen in Figure 3.3 C).

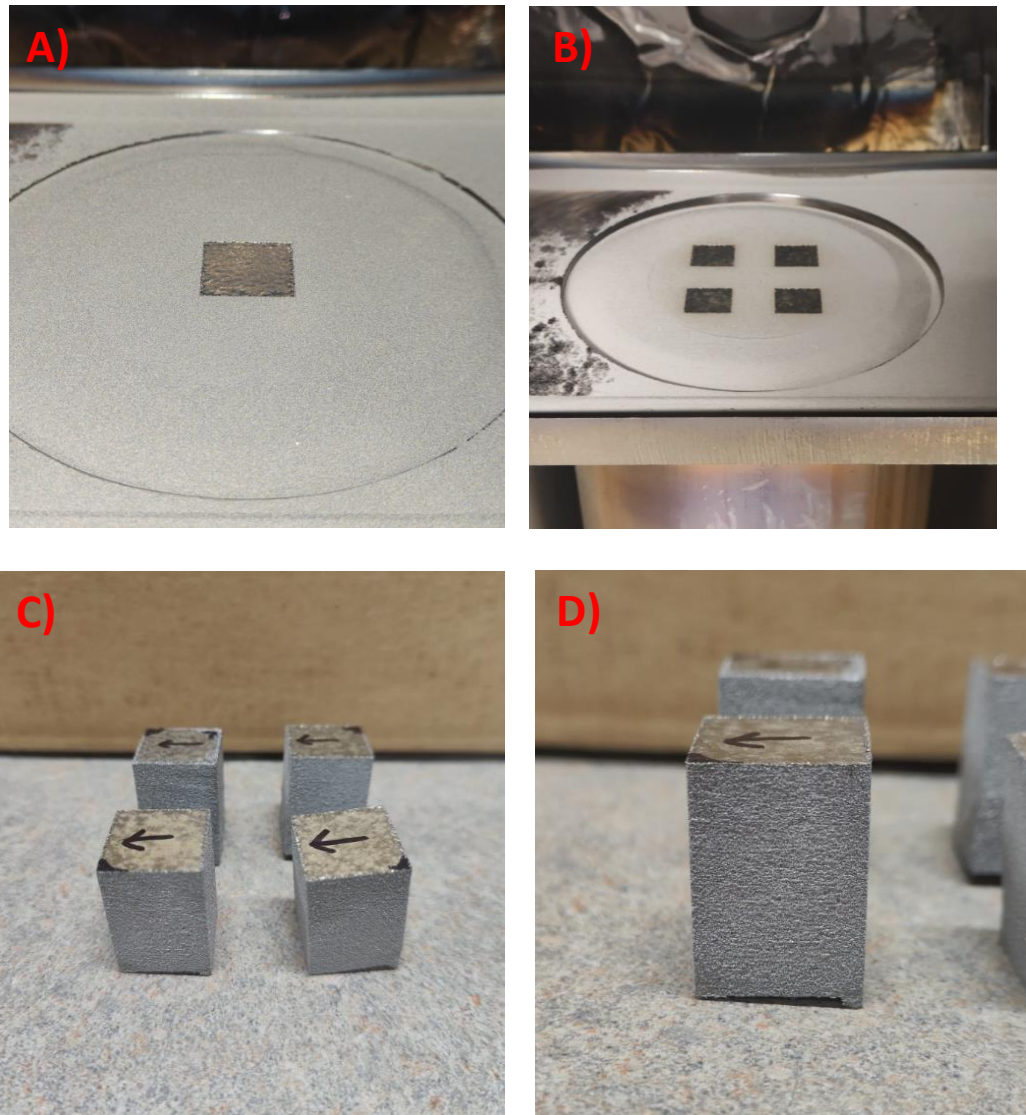


Figure 3.3: A) & B) Represent the 5 samples and environment right after opening the chamber. C) Represents the samples after being machined off the plate (the arrows represents the rake direction). D) Illustrates the typical (EBM characteristic) rough surface finish on the prism.

### 3.2.2 Heat Treatments

A HIP heat treatment was applied to a portion of the samples to analyze the effect of hydrogen in both as-built and HIPed samples. The process consisted of elevating the temperature to 1160 °C at a rate of 15 °C/min, then holding the temperature at 1160 °C for 3 hours at 100 MPa in an Argon atmosphere, and finally just letting it cool by itself inside the furnace (furnace cooling).

This whole process is illustrated in Figure 3.4. Again, the HIPing process is mainly meant to close or eliminate porosity within the part as it applies heat and pressure to it. ASTM F3301 standard was used for this process.

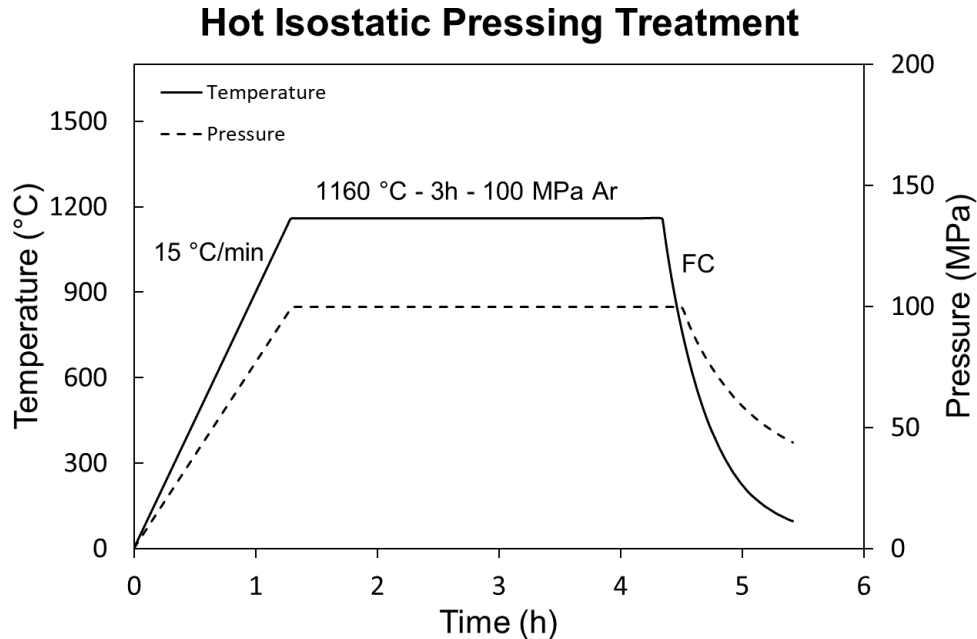


Figure 3.4: HIP process graph.

### 3.3 CHARACTERIZATION

#### 3.3.1 Electron Backscatter Diffraction (EBSD)

EBSD is a microstructural characterization technique that is used to obtain crystallographic information from a material. This technology works by directing an electron beam to the sample being analyzed at an angle which will form diffraction patterns from the backscattered electrons hitting the crystal lattice, which will be detected or captured by the machine. This procedure serves to obtain crystallographic orientation, grain boundary character (e.g., low-angle boundaries, high-angle boundaries, and twin boundaries), and identify phases (such as the  $\gamma'$  and  $\gamma''$  strengthening phases, carbides, and Laves phases) and grain morphology which all affect the material's properties and performance. As previously mentioned, EBM is a complex process which involves

rapid solidification and complex thermal cycles which all affect the material's microstructure and needs to be characterized with a method such as EBSD.

A small rectangular section of the original printed parts were cut for this analysis. All of the samples were prepared for EBSD analysis grinding and polishing them with SiC abrasive paper with sizes ranging from 800 to 2400, and polishing with 3  $\mu\text{m}$  and 1  $\mu\text{m}$  diamond suspensions. As EBSD procedure requires a high-quality surface finish to ensure the production of clear diffraction patterns, the samples must undergo a final polishing step using a 0.02  $\mu\text{m}$  oxide polishing suspension solution. Features such as the grain size, morphology, orientation as well as the grain boundary character were extracted and examined using EBSD. Coarse and fine maps (low and high resolution) were obtained by using a field-emission scanning electron microscope (ZEISS Crossbeam 340-VP), shown in Figure 3.5, equipped with an EDAX EBSD detector with a step size ranging from 0.7  $\mu\text{m}$  to 8  $\mu\text{m}$ . A clean-up procedure was performed on all EBSD images on OIM TSL Analysis v8 software.



Figure 3.5: ZEISS Crossbeam 340-VP EBSD machine [106].

### 3.3.2 Optical Microscopy

This procedure complements EBSD as another form of observing and analyzing microstructures from a different perspective and even observe defects such as porosity, cracks, and lack of fusion and also assess the quality of the surface finish. The sample is polished to eliminate all the roughness and create a smooth surface which is critical for proper observation. Again, these procedure required SiC abrasive paper with sizes ranging from 800 to 2400, and polishing with 3  $\mu\text{m}$  and 1  $\mu\text{m}$  diamond suspensions. Then the sample is electro-etched with oxalic acid at 4 V and 3 A for around 2 min (time is dependent on the sample size) to enhance the contrast between different phases, grains, and microstructural features. Figure 3.6 illustrates the electro-etching procedure.

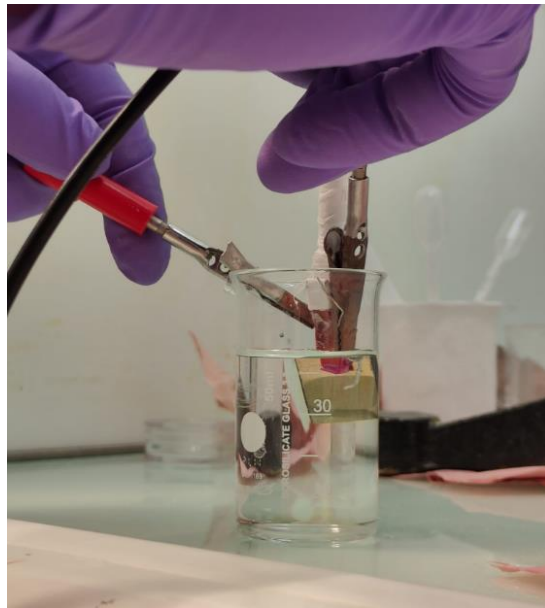


Figure 3.6: Electro-etching setup.

After electro-etching, the sample is taken to be observed and analyzed under a microscope. For this study, a Keyence VH-ZST microscope, shown in Figure 3.7, was used to analyze the samples. Different magnifications were used to analyze the various microstructural features of the samples.



Figure 3.7: Keyence VH-ZST microscope

As the results and discussion section show, after performing optical microscopy and observing vertical and horizontal samples, the microstructure was very similar in size and shape, which is why, for the rest of the experiments, only vertical samples were tested.

### 3.3.3 Transmission Electron Microscopy (TEM)

TEM is a technique that makes it possible to analyze materials at an atomic level. Defects, composition, lattice structure, phase composition, and grain boundaries are some of the things that can be observed by using this technology. It works by passing a beam of electrons through a thin section of the material, the edges of the holes created by electro-polishing, which will make these electrons diffract, create specific patterns depending on the phase of the material being observed, and finally create an image of the material's inner structure. A Jeol TEM apparatus was used for this study (shown in Figure 3.8). For INC 718, it will make it possible to analyze the size, shape, and distribution of precipitates such as  $\gamma'$  and  $\gamma''$ , detect some of the dislocations in the sample, etc.

The samples used for TEM observation were sectioned into a 3 mm diameter disc, with a final thickness of  $\sim 100 \mu\text{m}$ . The samples were progressively polished with SiC abrasive paper with sizes ranging from 800 to 4000 to achieve a smooth surface finish.

After polishing, the samples were electro-polished using a TenuPol-5 machine to create small holes in the samples as the TEM machine will focus on them to extract the images and information.

The solution used for the electro-polishing has the following mixture: 75% of MeOH, 16% of 2-Butoxyethanol, and 9% of Perchloric Acid.



Figure 3.8: Jeol TEM Machine

### 3.3.4 Scanning Electron Microscopy

Scanning Electron Microscopy (SEM) is a technology that uses a beam of electrons to analyze the surface of a sample at very high resolutions (even at the nanometer scale). When the electron beam hits the material's atoms at the surface, these send a signal to the SEM apparatus containing data about the metal's surface, creating an image. This technology is useful for analyzing phases, grain boundaries, and defects in the microstructure, which is what was done in this study.

As-built and HIPed samples were analyzed under SEM after being etched to highlight the microstructural features. Energy-dispersive X-ray spectroscopy (EDS) system, was coupled with this study to perform elemental analysis which provides more insight into the material's composition and element distribution. EDS was mainly done to analyze the primary elements such as Ni, Cr, Mo, Ti, C, Al, Fe, N, and Nb. This technique creates color-coded maps which allows a simple element distribution observation. An Axia SEM apparatus was used to perform the analysis, shown in Figure 3.9.



Figure 3.9: SEM Machine, Axia

### 3.4 HYDROGEN CHARGING

Hydrogen charging, following ASTM G148-97, was done to understand the interaction between hydrogen and INC 718; how it affects its properties and performance.

The samples were made into rectangular pieces of dimensions 4 X 10 mm and ~400  $\mu$ m thickness. They were slightly polished to remove the stresses induced when sectioning/cutting them. After, they were attached to a screw with conductive glue, as this will ensure current passed to the sample, and finally covered in resin, as seen in Figure 3.10.

The charging is done by immersing the sample in an electrolyte solution and passing an electrical current through it to facilitate the absorption of hydrogen. The setup is shown in Figure 3.11. The current applied depends on the size or area exposed of the sample. For the dimensions mentioned above, a current of 24 mA was applied. The samples were tested for 72 hr at room temperature.

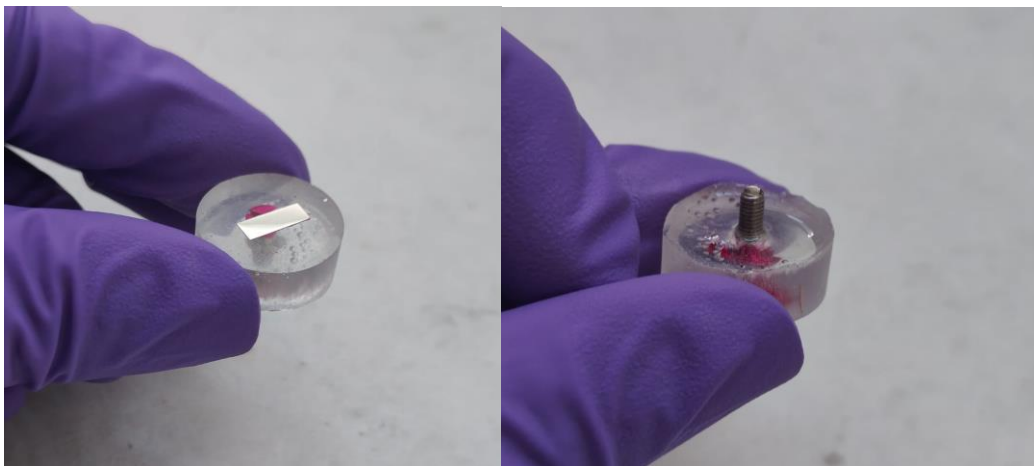


Figure 3.10: Sample in resin (charging preparation)

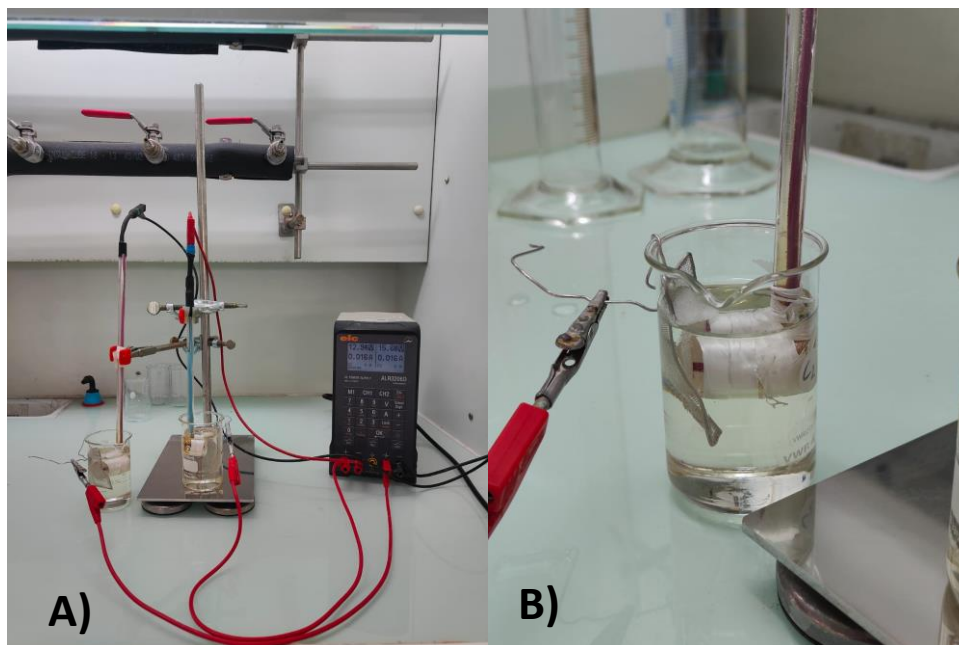


Figure 3.11: A) General and B) Close-up view of the H-charging Setup

### 3.4.1 Thermal Desorption Spectroscopy (TDS)

Right after charging, a TDS test is performed in a Horiba Hydrogen Analyzer, shown in Figure 3.12, to obtain the hydrogen concentration in the sample as it is being melted. It is crucial to perform the test as soon as the samples are taken out of the charging solution as hydrogen starts diffusing not only further into the sample but also out of it. The sample is placed inside the TDS apparatus, which then proceeds to heat and melt it by raising the temperature to 2000 °C, which makes the hydrogen desorb. The whole experiment usually takes around 2 min. This hydrogen desorption is measured and recorded by the apparatus. Hydrogen concentration measurements are crucial to understanding how hydrogen moves through the metal, provide insight into hydrogen diffusion dynamics, and help to learn how much hydrogen a material can absorb and retain under different conditions, in this case, as-built vs HIPed.



Figure 3.12: Horiba Hydrogen Analyzer

### 3.5 MICROHARDNESS

This technique is used to obtain the mechanical properties of a material, especially its hardness (resistance to deformation). It involves applying a measured localized force by pressing

a precise indenter (usually diamond) into the material's surface. Microhardness tests are especially useful when the surface explored has a mixed microstructure like the one studied in this study as it allows to test hardness at precise points and study localized properties on different phases and grain sizes. For this experiment, Vickers technique was used. The apparatus used to perform these tests is shown in Figure 3.14 and the schematic of this test in Figure 3.13. A row of 5 indentations with a force of 5 mg was performed by separating each indentation 25  $\mu\text{m}$  from each other to account for the indentation diameter and ensure having a valid result. Also, this distance was chosen to analyze the area of interest; hydrogen only permeates a few tenths of microns into the material (depending on the charging time). Three rows of indentations, with a separation of 50  $\mu\text{m}$  between them, were made to analyze the hardness values at different locations and have more accurate results as shown in Figure 3.13.

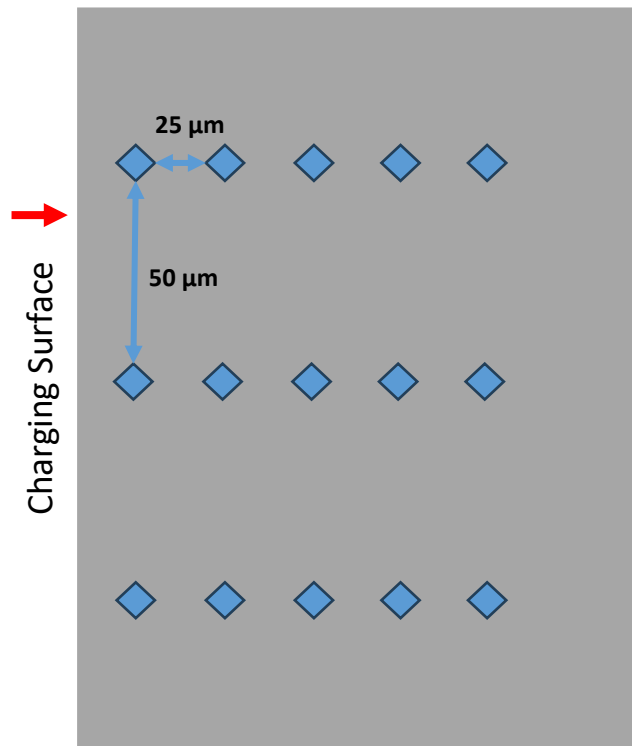


Figure 3.13: Indentation Schematic



Figure 3.14: Anton paar Step 4, Microhardness Apparatus

### 3.6 TENSILE TESTS

Tensile testing was conducted to determine the specimens' behavior under uniaxial tensile stress and obtain the specimens' yield stress, ultimate tensile stress, and elongation at fracture. The process involves pulling the tensile specimen at a certain strain rate ( $10^{-4} \text{ s}^{-1}$  for this experiment) until fracture/failure while recording data to plot stress vs. strain curves and determining the mechanical properties of the samples. This was performed on HIPed and as-built samples, both in H-charged and uncharged conditions, in the vertical direction. Two samples of each specimen were tested for comparison. Figure 3.15 shows the dimensions for the tensile samples and Figure 3.16 shows the apparatus used to perform the tests.

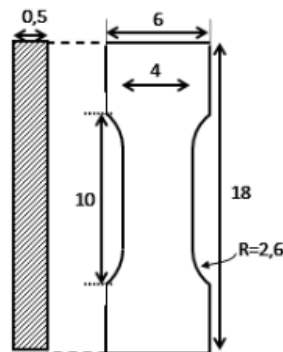


Figure 3.15: Tensile Sample Dimensions

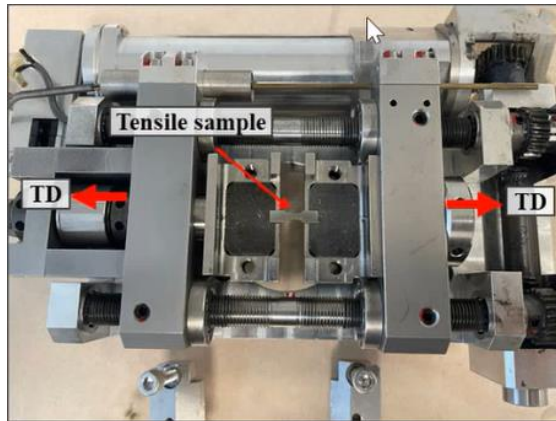


Figure 3.16: Kammrath & Weiss Tensile Apparatus

## 4. Chapter 4: Results and Discussion

### 4.1 CHARACTERIZATION RESULTS

#### 4.1.1 EBSD Results

##### 4.1.1.1 *As-built Samples*

When observing the EBSD images in the as-built state, Figure 4.1, it can be seen how the grains do not possess a particular growth direction or anisotropy as in most cases in AM parts. This is due to the particular thermal gradient caused by the scanning strategy. As mentioned before, spot melting scanning strategies often melt the layer surface in smaller discrete areas which promotes a more uniform heat distribution and not a directional one as in other scanning strategies. Aside from this, spot melting usually means smaller thermal gradients and faster cooling rates which tend to promote slightly smaller grain sizes and an overall more equiaxed microstructure, which can all be seen in Figure 4.1.

The next image, Figure 4.2, represents the polar figures for this microstructure which confirm the randomized texture. As it can be clearly observed, there is not a clear strong pattern or distribution for the crystallographic orientation of the microstructure, meaning the samples have a mostly randomized texture. This is something particular to this scanning strategy as typical scanning strategies tend to have a very strong texture, usually towards the build direction in the  $\langle 001 \rangle$  direction. Compared to a study done by Goel et al., pole figures from highly columnar microstructures show much more texture and intensity values when built using a raster/line melt [88].

The as-built microstructure averages  $95.6 \pm 1.2\%$  in high-angle grain boundaries across vertical and horizontal build directions. This high number again confirms the randomized and untextured microstructure as low-angle grain boundaries cannot have an untextured microstructure. From this percentage,  $75 \pm 0.8\%$  belongs to random grain boundaries with a  $\Sigma > 29$  while  $20 \pm 1\%$  belongs to CSL grain boundaries with a  $\Sigma < 29$ . Figure 4.3 represents the microstructure with the actual random and CSL GB distribution. As it can be observed, even

though CSL GB are spread evenly throughout the area, they appear to be somehow connected in clusters.

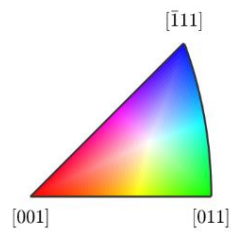
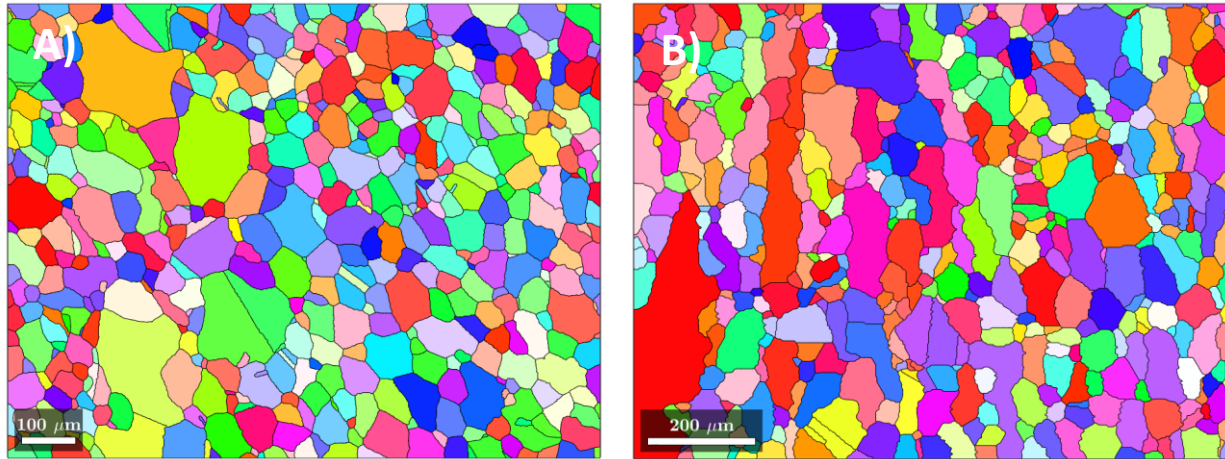


Figure 4.1: A) Horizontal and B) Vertical As-built EBSD Map

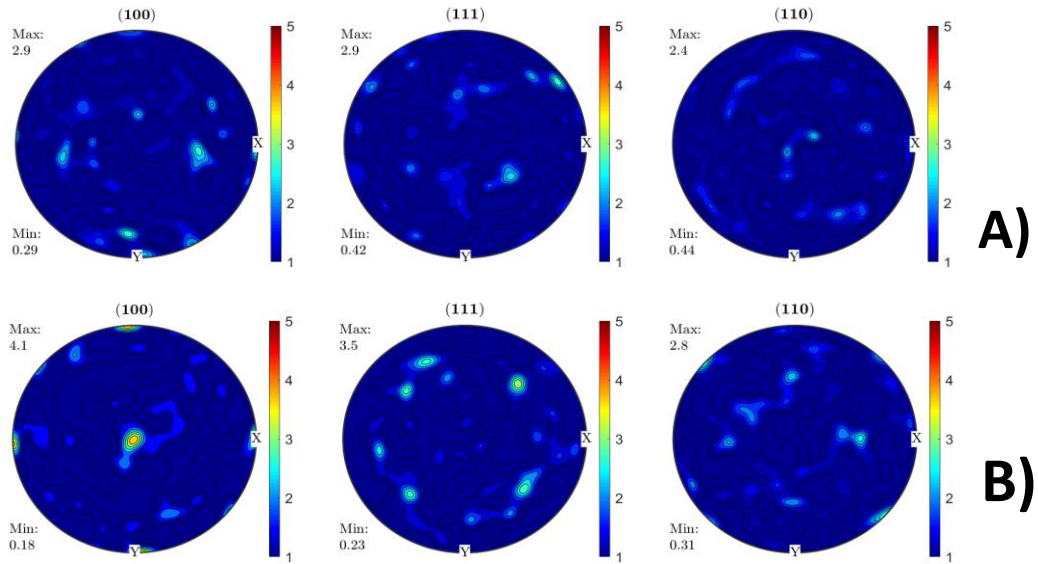


Figure 4.2: A) Horizontal and B) Vertical As-Built Pole Figures

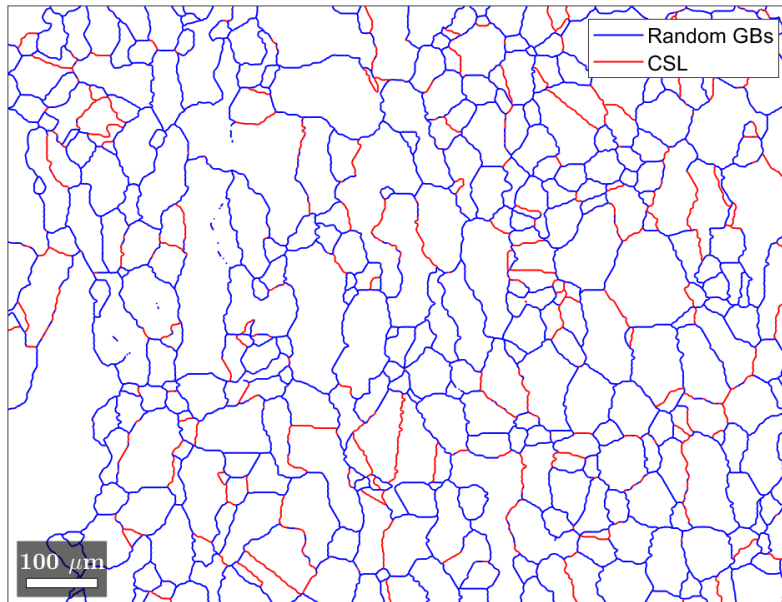
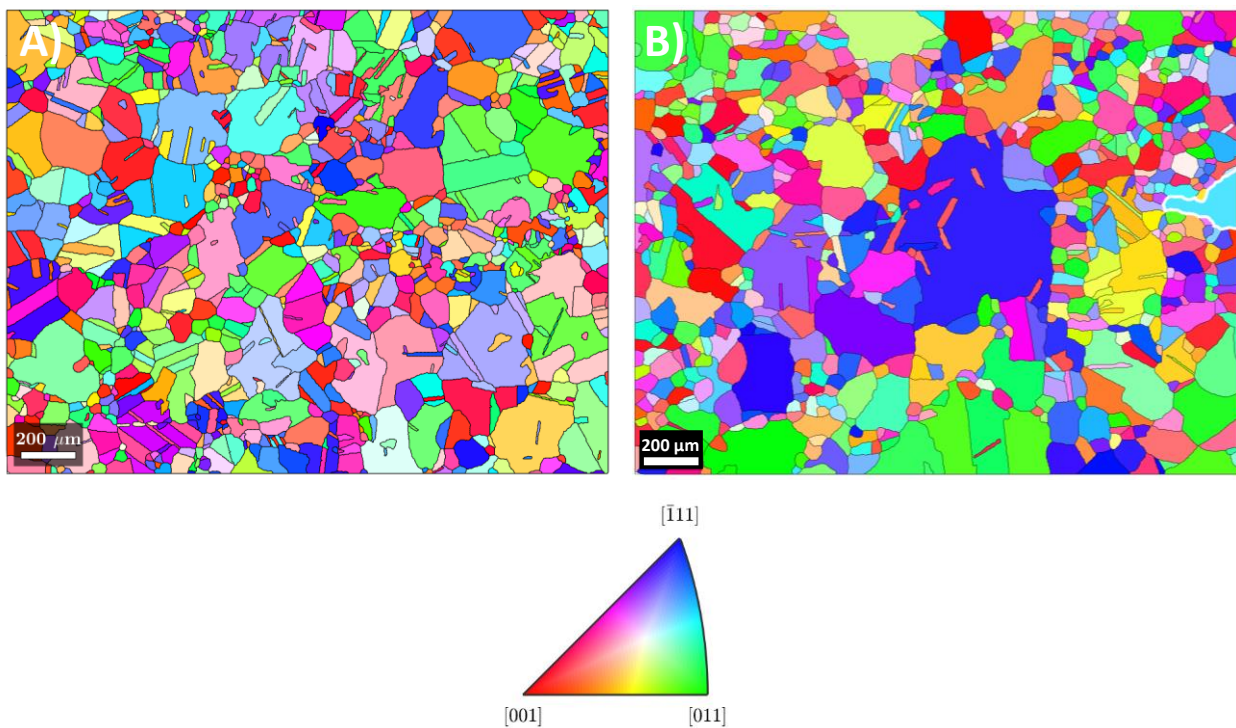


Figure 4.3: Random vs CSL distribution. As-Built Vertical.

#### 4.1.1.2 HIPed Samples

The next images represent the microstructures after HIPing. The pole figures, Figure 4.5, show that after HIPing, the overall microstructures maintain the same type of randomized

crystallographic orientation, not exactly in the same directions as before, but still mostly showing a weak texture, especially when compared to the HIPed samples studied by Goel et al. [88]. After HIPing, the average grain sizes were expected to experience high growth as seen in other studies [87], [107], [108], nevertheless, as seen in Figure 4.7, grain sizes did not experience significant growth. Also, the microstructure retains a high percentage of high-angle GB with 97.2%. Nevertheless, its distribution is different as the overall percentage of random GB decreased while the CSL percentage increased as shown in Figure 4.8. This can be observed as HIPed samples usually have a higher percentage of twin grain boundaries (which are CSLs) [109]. Figure 4.6 shows the map distribution of random vs CSL GB. Random Gb still dominate the matrix while CSL GB seem to be evenly scattered throughout the microstructure but still connected to one another in most cases. It can also be observed that a large percentage of the CSL GB corresponds to twin GB.



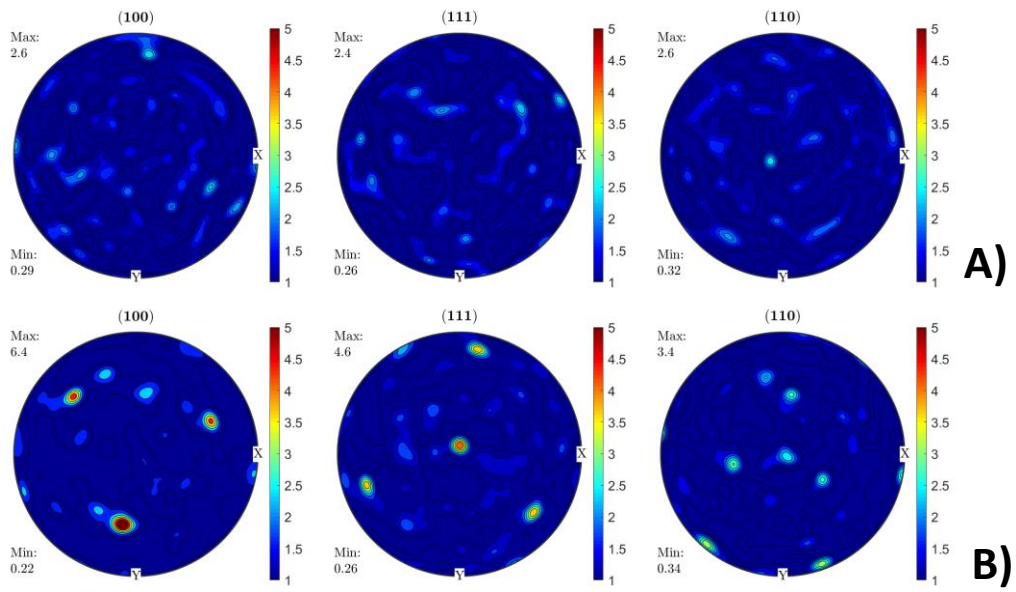


Figure 4.5: A) Horizontal and B) Vertical HIPed Pole Figures

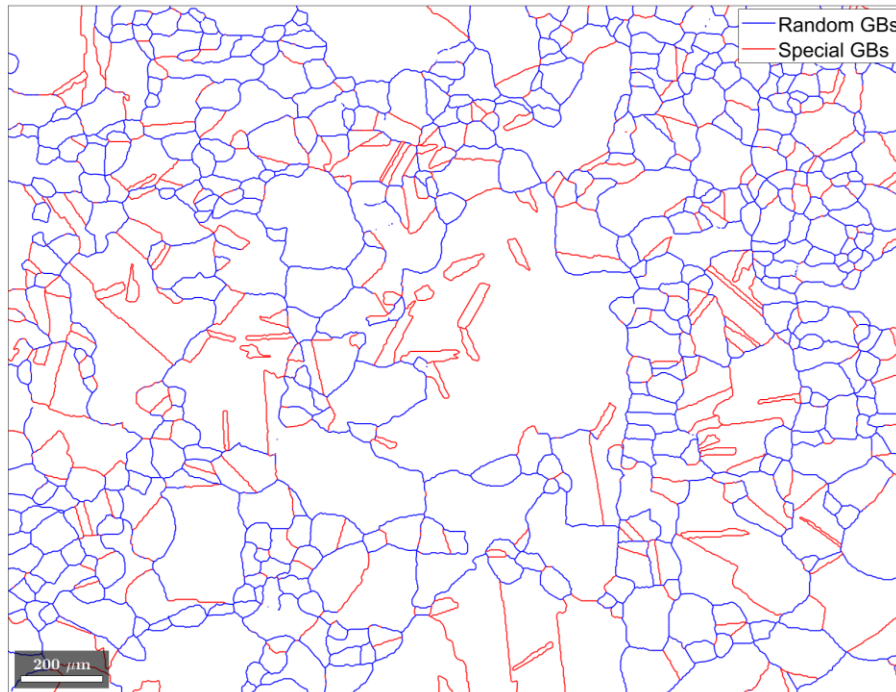


Figure 4.6: Random vs CSL distribution. HIPed Vertical.

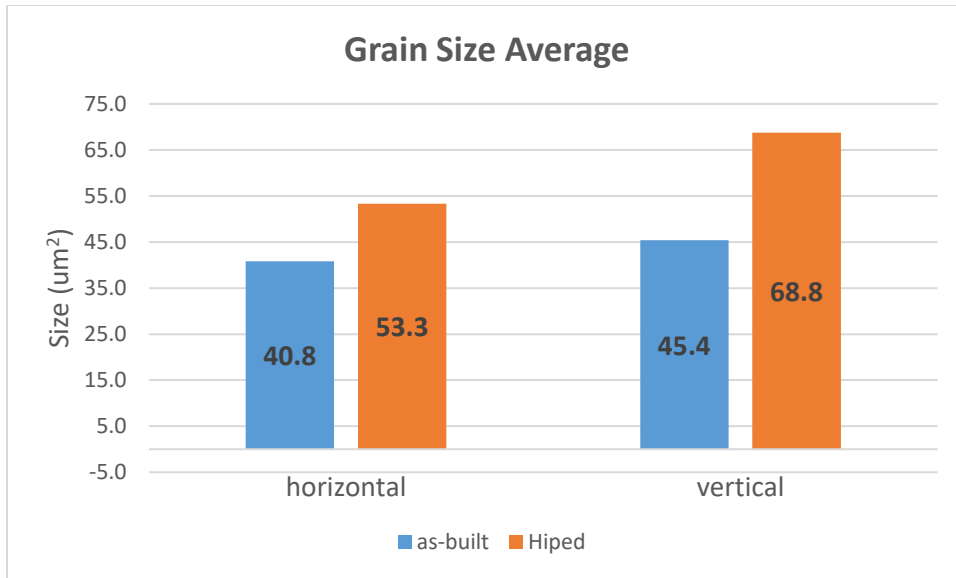


Figure 4.7: Grain Size for As-built and HIPed Graph

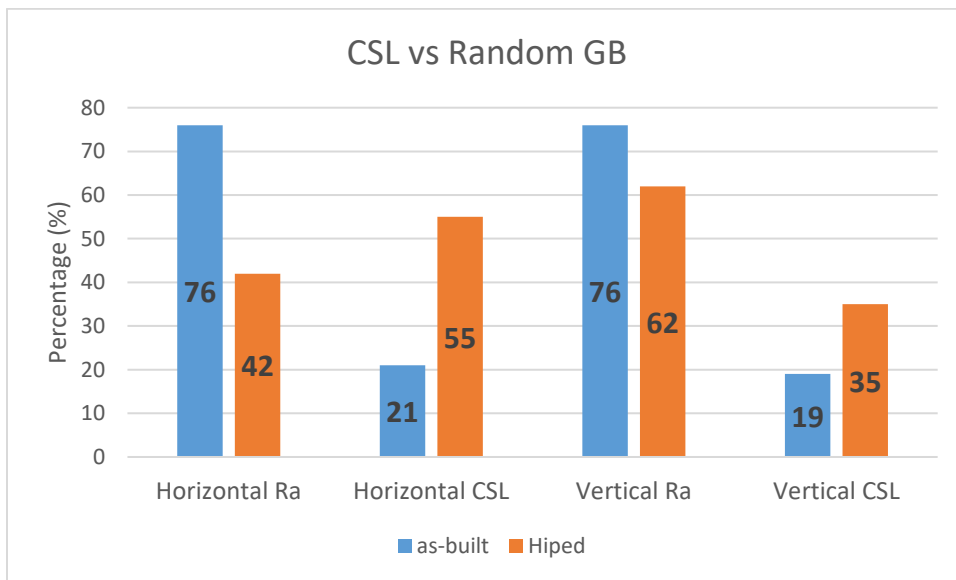


Figure 4.8: CSL vs Random GB Graph

#### 4.1.2 Microscopy Results

Microscopy images were taken at different magnifications to observe multiple phenomena and compare between as-built and HIPed samples, while also comparing vertical and horizontal build directions.

#### ***4.1.2.1 As-built Samples***

When observing the samples in their as-built state, it can be seen that although there is still some percentage of columnar grains along the build direction, these samples do not exhibit the same dominant anisotropic columnar grain structure as most EBM-printed parts. This is due to the SDS spot-melting scanning strategy used in this study. The scanning strategy effectively created a more equiaxed microstructure. Interestingly, it consists of bigger grains along with clusters of smaller grains. This mixture may affect the way hydrogen diffuses through the material, the hardness values at different points of the samples, and the strength and ductility of the parts.

Another evident feature is the large amount of porosity in the samples. Most of this porosity can be categorized as lack of fusion, which happens when there is not enough energy to melt the powder (a common type of defect in metal additive manufacturing). Multiple reasons can cause this; low beam power, high scanning speeds, unfocused beam, insufficient preheating, high layer thickness, etc. It is crucial to adjust the printing parameters for future prints as porosity can later result in crack initiation areas and premature failure. More experiments and prints must be conducted to explore the multiple parameters, identify the specific cause for this issue, and better understand this scanning strategy. Also, as seen in Figures 4.9, 4.10 & 4.12, there are a few areas where grain boundaries appear to be darker, which might indicate a concentration of precipitates. After observing similar precipitate concentrations in other scientific studies [110], [111], it was determined to be delta phase segregation.



Figure 4.9: As-built Vertical. 200 um scale. XZ Plane. Red arrow showing possible intergranular cracking.

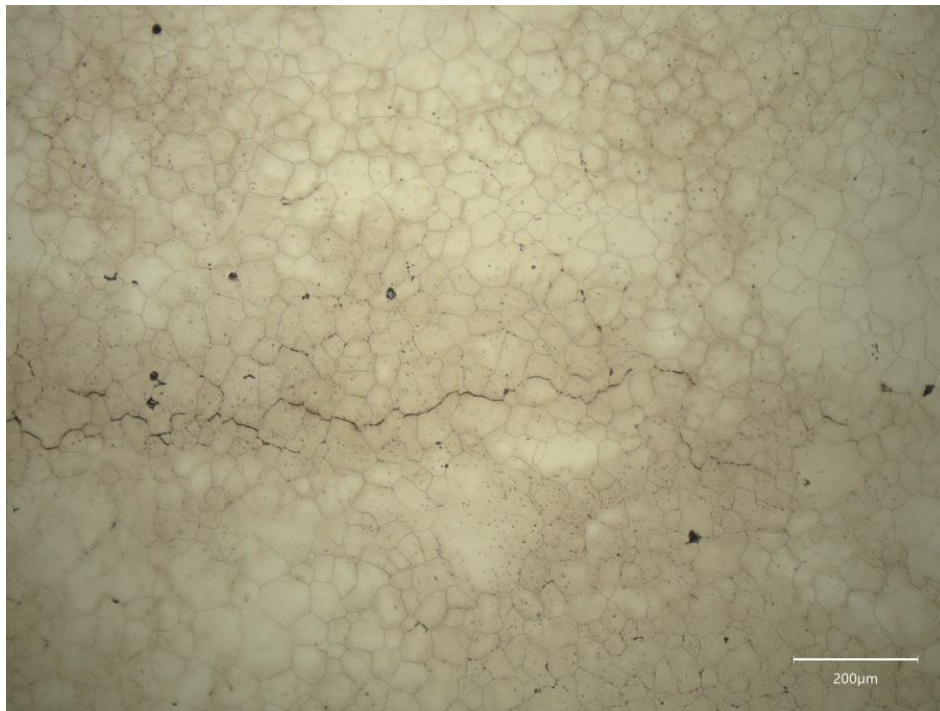


Figure 4.10: As-built Horizontal. 200 um scale. XZ Plane.

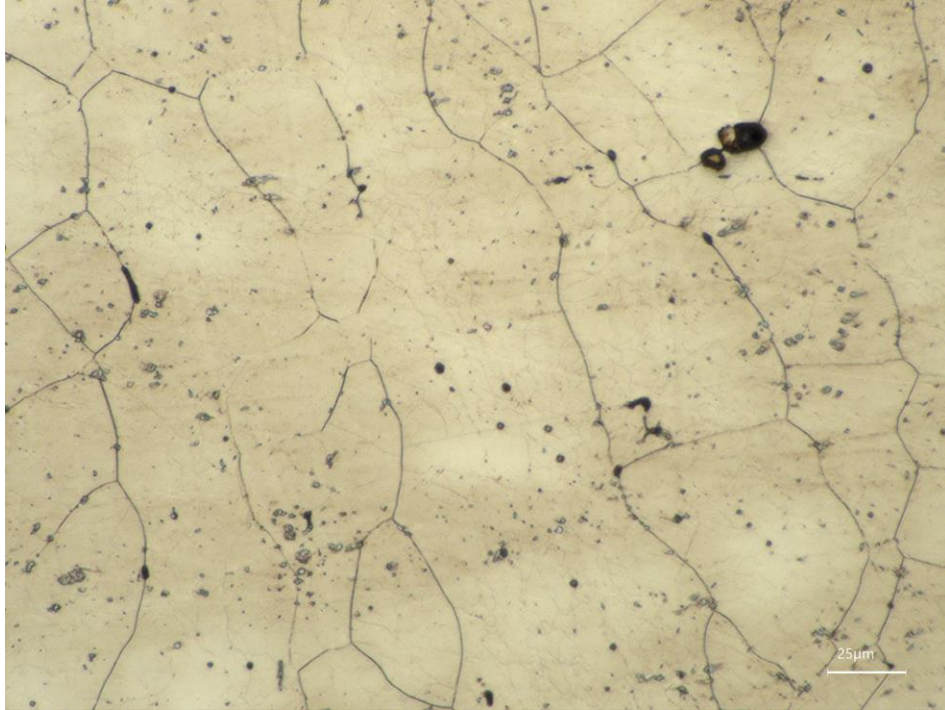


Figure 4.11: As-built Vertical. 25 um scale. XZ Plane.

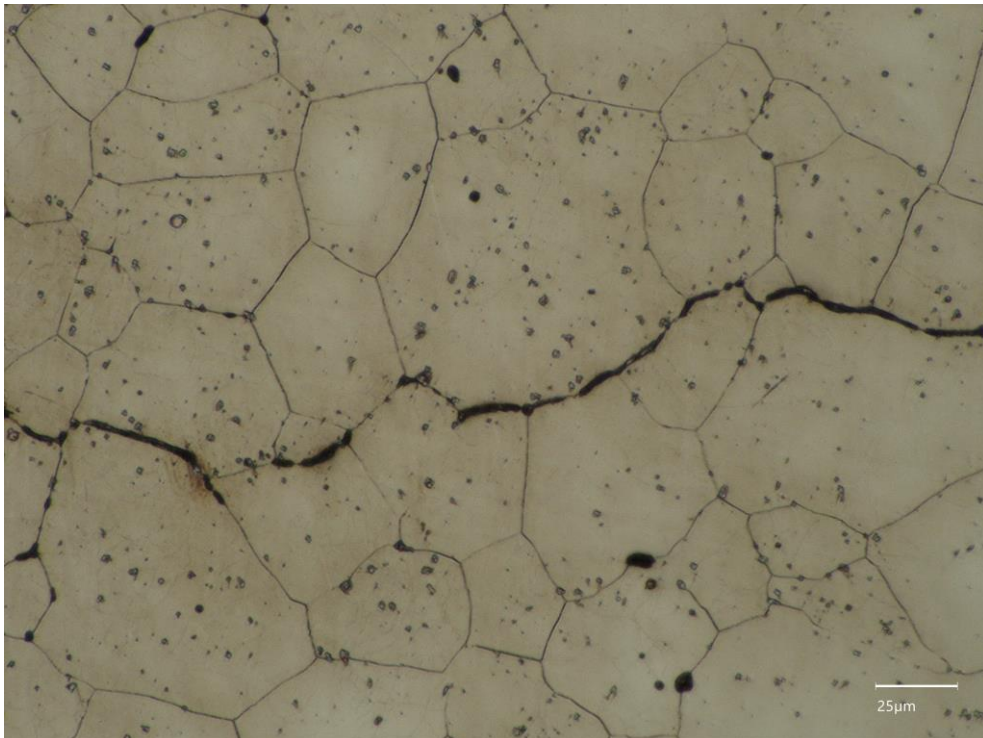


Figure 4.12: As-built Horizontal. 25 um scale. XZ Plane.

#### ***4.1.2.2 HIPed Samples***

Usually, after doing a HIP heat treatment, the microstructure of the EBM printed samples will somewhat change (dimensions, morphology, texture, etc). Nevertheless, when comparing Figures 4.13 & 4.14, it can be seen how the samples retained their general grain size and morphology after HIP. This is likely due to the precipitation shown in the HIPed figures by the red arrows, which might be some kind of carbides spread across the microstructure, especially along grain boundaries, as shown in Figure 4.15, which usually prevents grain growth during the heat treatment. The presence of carbides cannot be fully confirmed from these images alone, which is why an SEM analysis was performed afterward.

When grain orientations in the HIPed samples (Figures 4.13 & 4.14) are compared, it can be seen that they have somewhat similar grain size and morphology. Both have a combination of bigger grains with clusters of smaller grains.

Appendix 1 shows the cross-section along the entire sample in both vertical and horizontal directions after HIPing, and the difference in porosity is still very evident. Vertical orientations will most commonly show more porosity, like in this case, as this orientation shows the printing layers and the defects between them can be more visible. By comparing the images in Appendix 1, it is clear that the HIPing treatment drastically decreased porosity. Nevertheless, HIPed samples still have much more porosity than desired. After performing porosity measurements by analyzing sample images in ImageJ software (seen in Appendix 2), it was seen that as-built samples were 97.8% dense and HIPed samples were 99.4% dense. This heat treatment process can only eliminate enclosed porosity, which means the remaining porosity is connected and open. Again, the lack of fusion clearly indicates that the printing parameters need to be adjusted.

As far as the precipitate segregation shown in the as-built images, the HIP treatment appears to have eliminated it, as this treatment usually also serves to dissolve precipitates and different phases back into the matrix and create a more uniform one.

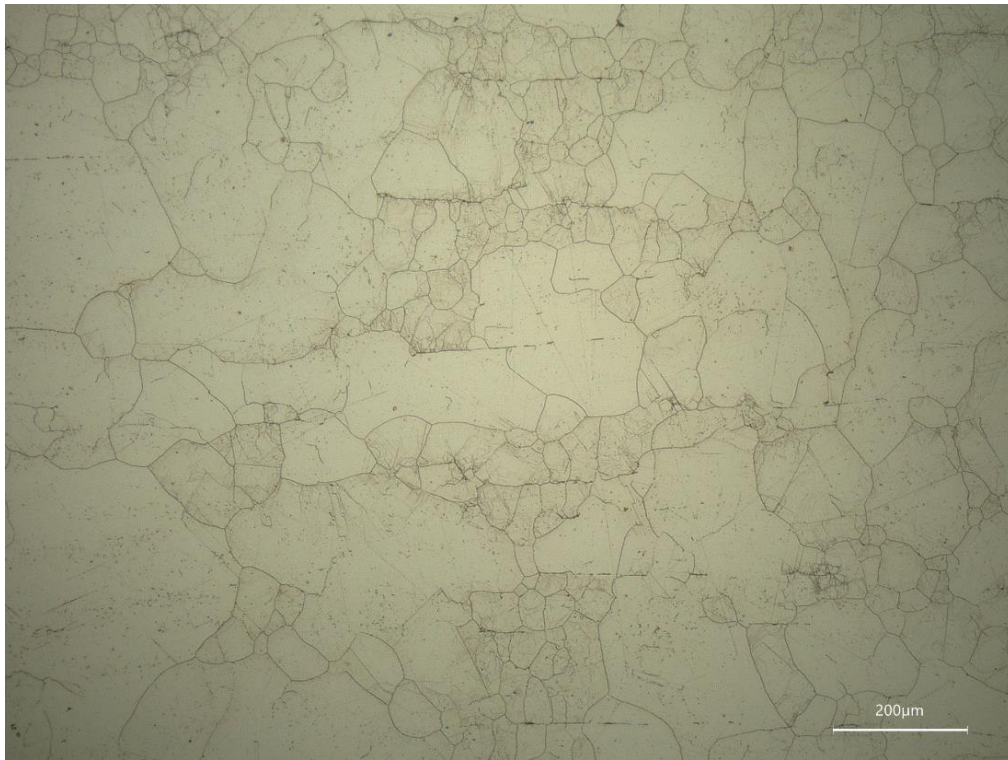


Figure 4.13: HIPed Vertical, Scale 200 um, XZ Plane

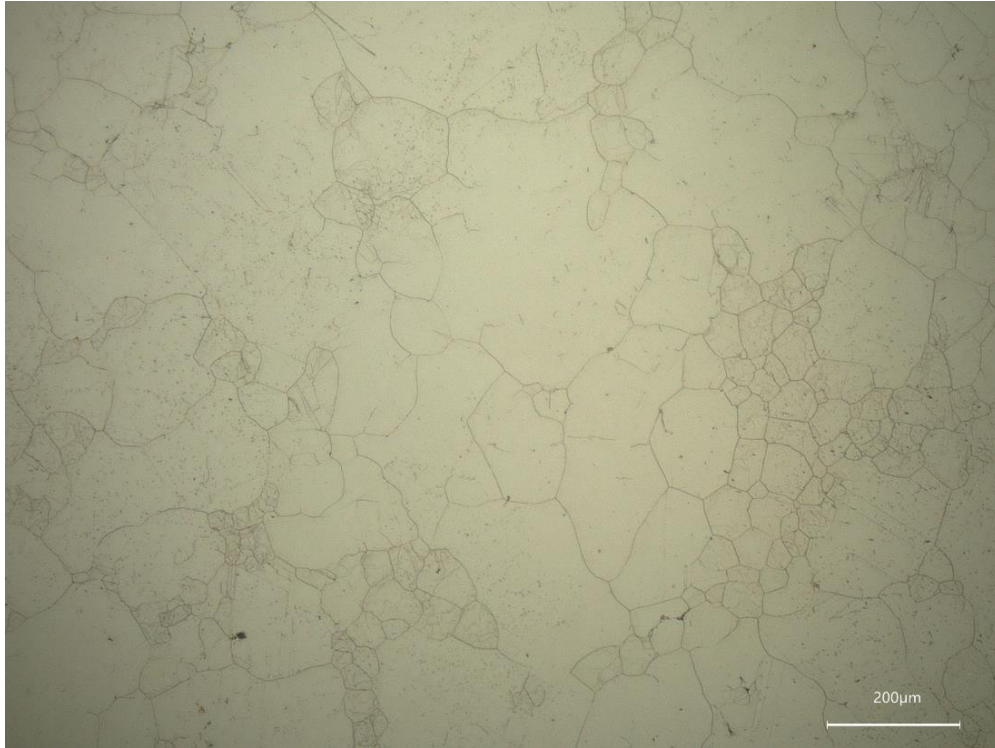


Figure 4.14: HIPed Horizontal, Scale 200 um, XY Plane

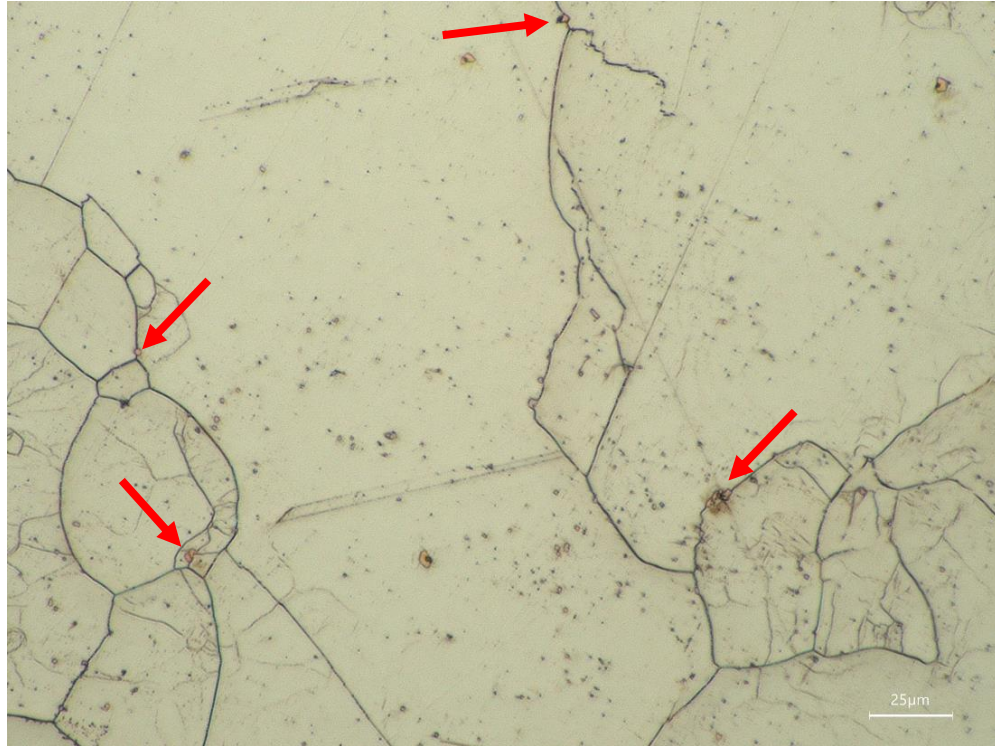


Figure 4.15: HIPed Vertical, Scale 25 um, XZ Plane, Arrows showing possible Carbides

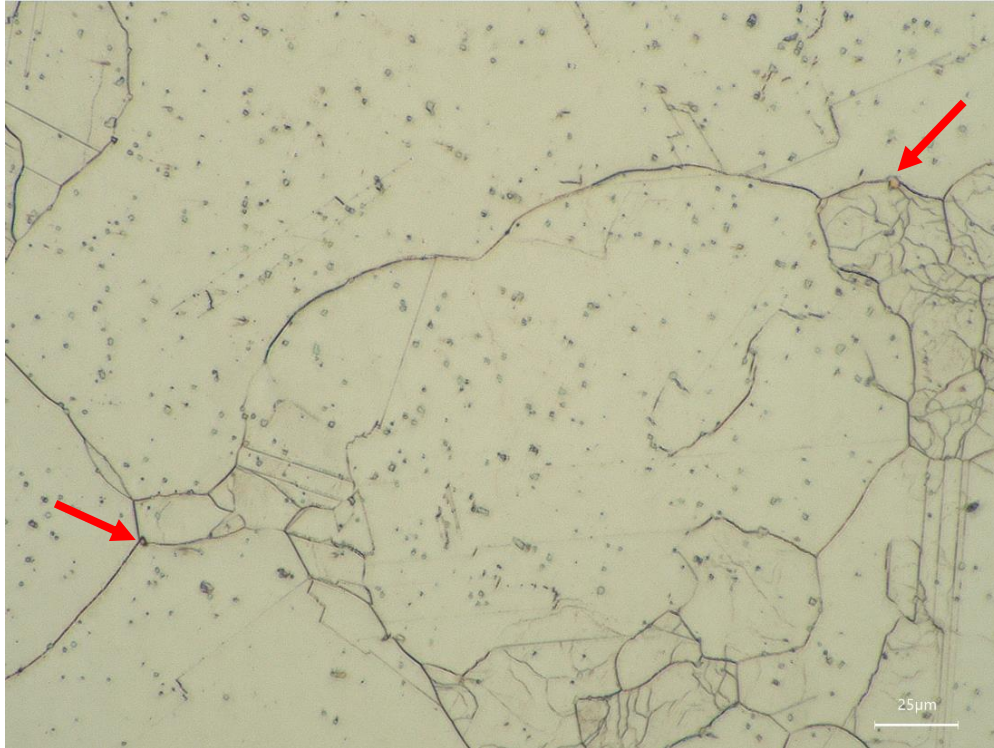


Figure 4.16: HIPed Horizontal, Scale 25  $\mu\text{m}$ , XY Plane, Arrows showing possible Carbides.

Again, after performing optical microscopy and EBSD on as-built and HIPed samples, it can be observed that both horizontal and vertical building direction microstructures are mostly the same, which is why, from this point on, this study was only focused on the vertical direction samples. Due to the chosen scanning strategy, the vertical direction was chosen as its microstructure is highly uncommon among most EBM printed samples. This makes this microstructure unique and worth studying and understanding.

### 4.1.3 TEM Results

#### 4.1.3.1 HIPed Condition

The samples in the HIPed condition are presented in Figures 4.17-19. TEM allowed to see fine features of the microstructure at a micro and nano scale. Figure 4.17 shows an example of a main grain boundary (most likely a high-angle GB) and a subgrain boundary (most likely a low-

angle GB as it is barely distinguishable and seems to share the orientation from the main grain. Based on this image, the diffraction pattern of the matrix was obtained.

As mentioned in the literature review section, one of the main characteristics of the HIPing process is that it tends to relieve most internal stresses present in the components induced during the printing process. This process affects dislocations as it usually decreases their density. This can be seen in Figure 4.18. Very few dislocation spots were found in the samples during TEM.

Finally, Figure 4.19 shows some level of gamma prime precipitation in the matrix. Although it is common for HIP to dissolve these precipitates due to their solvus temperature, gamma prime has the chance of reforming in the cooling part of the process. Finding gamma prime in these samples was challenging which might mean low levels of it in the HIPed specimens.

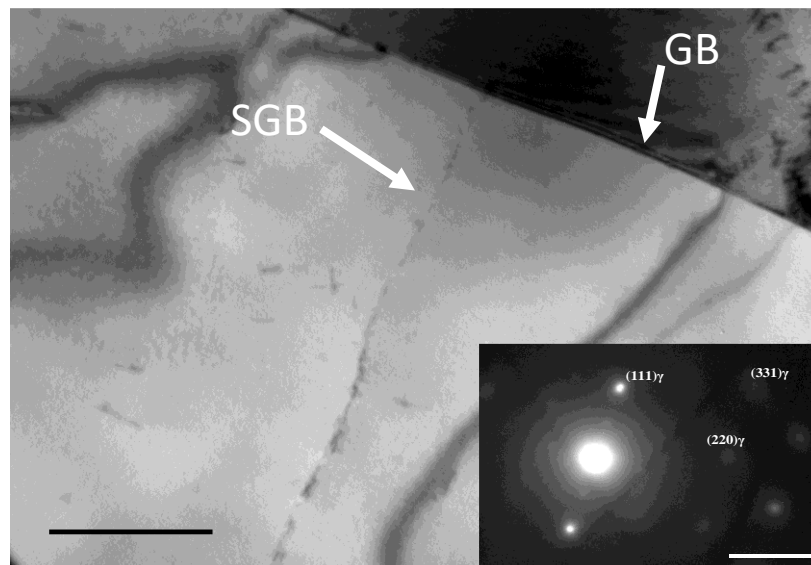


Figure 4.17: TEM Bright field image of a Grain Boundary (GB) and a subgrain boundary (SGB) and diffraction pattern corresponding to the matrix

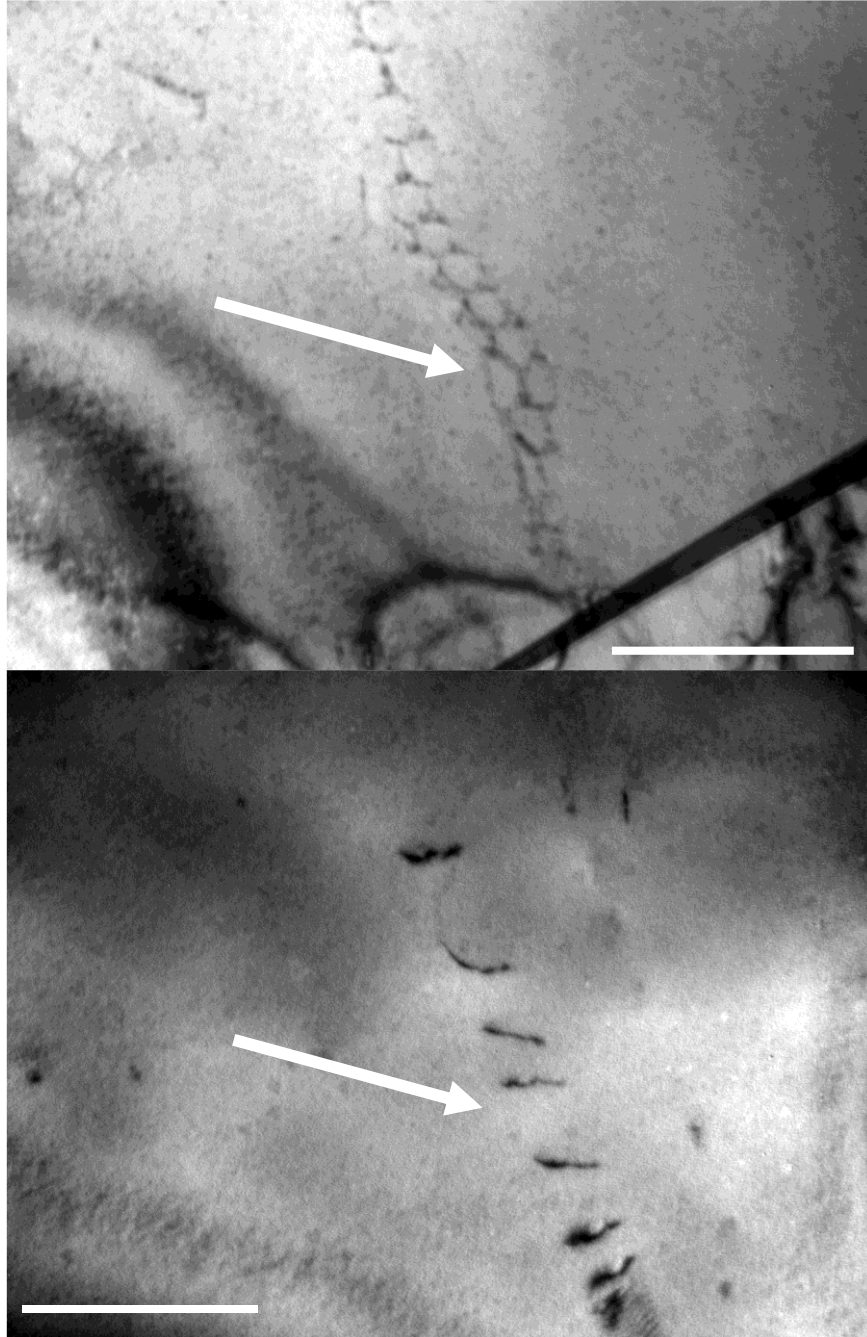


Figure 4.18: TEM Bright field images of Low Dislocation Density

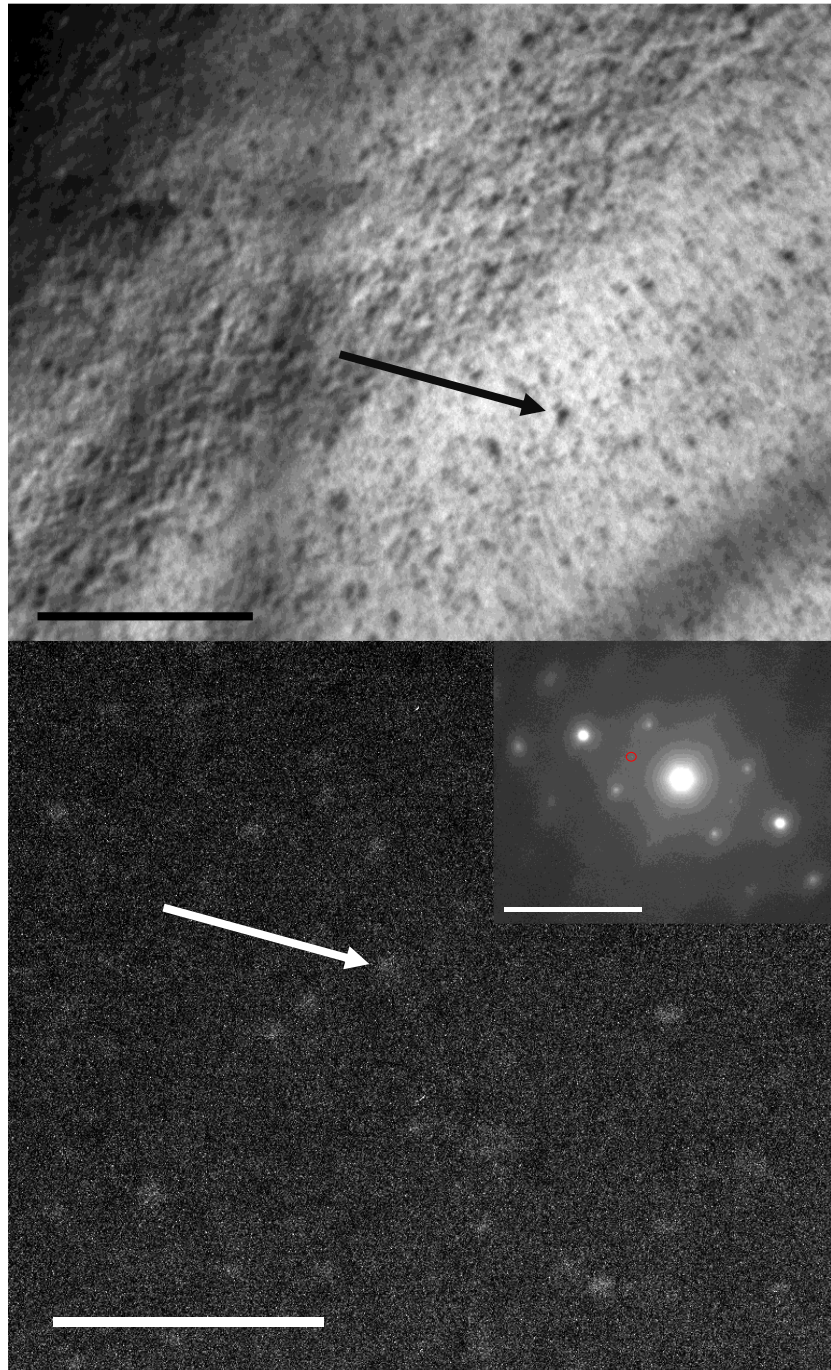


Figure 4.19: Bright field image and dark field image showing (with white arrows) gamma prime precipitate and the corresponding diffraction spot

#### 4.1.4 SEM Results

Again, SEM analysis was especially done to obtain EDS maps and be able to better understand the material composition and element distribution. A representative area of the sample was chosen for this process.

##### 4.1.4.1 As-Built Samples

The area chosen for the as-built sample is shown in Figure 4.20. This image shows an enlarged view of grains, grain boundaries, and some precipitation scattered throughout the image. These precipitates do not seem to have a preferential position as they are placed inside the grains and at the grain boundaries.

After performing EDS, Table 3 was obtained. Compared to the chemical composition, Table 1 shows that most elements have their expected content percentage except for Carbon. This element content is initially supposed to be around 0.08%, whereas here, it is 7.5%. This significant increase might be due to using carbon tape when mounting the samples to the SEM fixture.

Table 3. As-Built Element Distribution

<b>Element</b>	<b>Wt. %</b>	<b>Wt. % Error</b>
C	7.5	0.0
N	1.6	0.0
Al	1.0	0.0
Cr	17.2	0.0
Fe	16.4	0.0
Ni	48.1	0.1
Nb	5.6	0.0
Mo	2.6	0.0

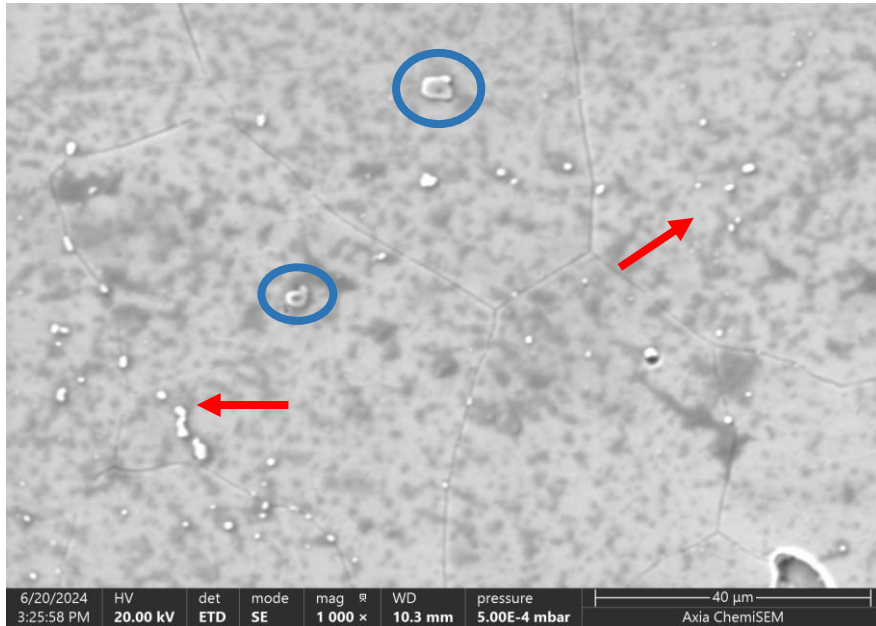


Figure 4.20: As-Built SEM Image. Red arrows showing carbides. Blue circles showing niobium-molybdenum nitrides.

The following image, Figure 4.21, shows the color-coded element distribution. Most elements appear to be well dispersed/scattered throughout the matrix. The precipitation mentioned before seems to be 2 different types. After observing the color-coded element distribution, the first precipitation, indicated with red arrows in Figure 4.20, is composed of niobium, molybdenum, and some carbon too. This composition makes it very likely for these phases to be a mix of MC carbides and  $M_{23}C_6$  carbides. The second precipitation type seems to be composed of niobium, a small percentage of molybdenum, and nitrogen. This composition belongs to a niobium nitride (NbN) or a niobium-molybdenum nitride.

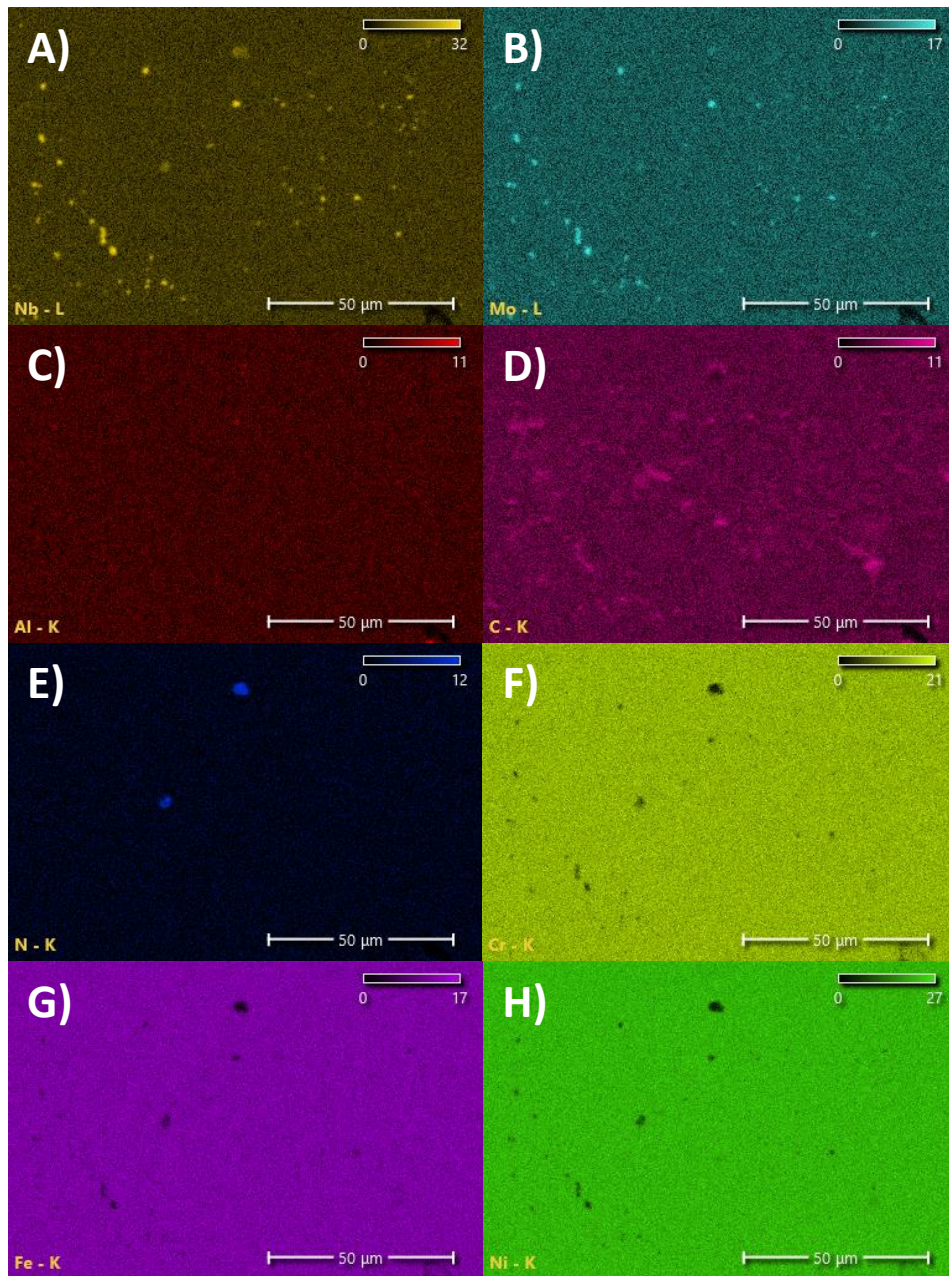


Figure 4.21: As-Built Element Color Distribution. A) Nb, B) Mo, C) Al, D) C, E) N, F) Cr, G) Fe, and H) Ni.

#### 4.1.4.2 HIPEd Samples

Figure 4.22 shows the chosen inspection area for the HIPEd sample. This image shows a similar view to the as-built sample, depicting the same precipitation arranged in a very similar way. Table 4 shows the element concentrations in that image. When comparing both tables, it can

be seen that both conditions have a very similar element percentage content, as the HIPing treatment does not affect these quantities.

Table 4. HIPed Element Distribution

Element	Wt. %	Wt. % Error
C	5.8	0.0
N	1.7	0.0
Al	0.5	0.0
Ti	0.9	0.0
Cr	17.5	0.0
Fe	16.5	0.0
Ni	48.6	0.1
Nb	6.0	0.0
Mo	2.5	0.0

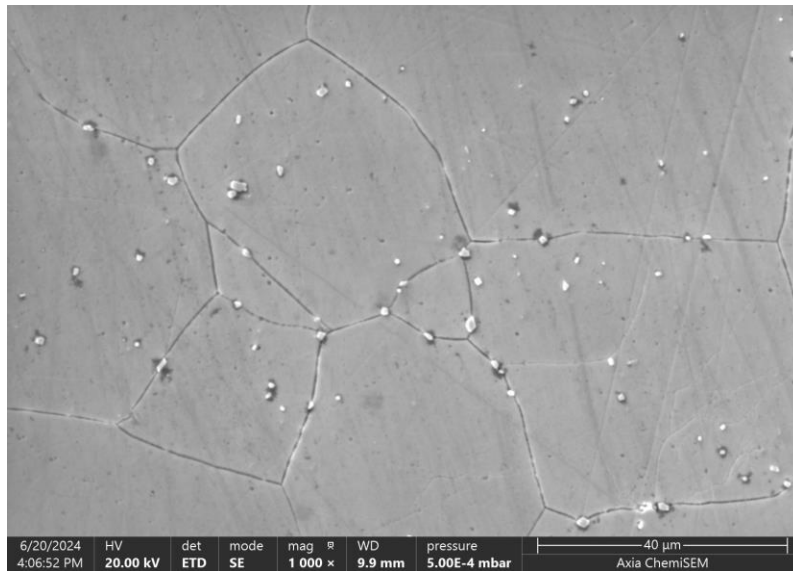


Figure 4.22: HIPed Sample SEM Image

The following Figure 4.23 shows the color-coded element distribution. Again, most elements seem to be well distributed throughout the matrix. After HIPing treatment, a better element distribution is always expected. Still, the same precipitation appears in the as-built

samples. These precipitates seem to be composed of niobium, molybdenum, carbon, and titanium, indicating they are the same types of carbides present in the as-built state. This is understandable as carbides' melting point is above the HIPing temperature; thus, they cannot dissolve into the matrix like most precipitates. These carbides might have played a significant role in the fact that grain sizes didn't grow much larger after this treatment as shown in the EBSD results section as also seen in a study done by Nandwana et al. [87].

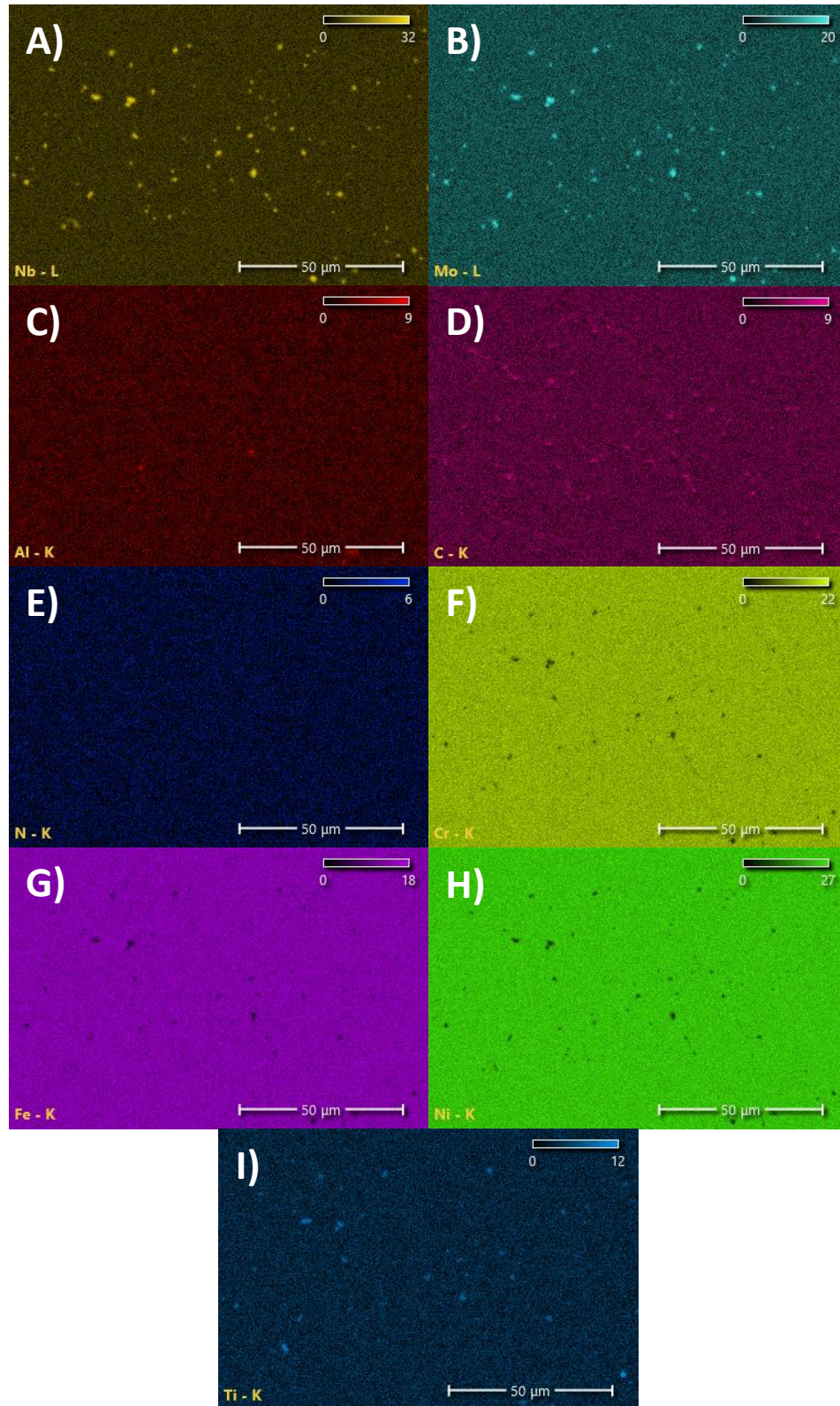


Figure 4.23: HIPed Element Color Distribution. A) Nb, B) Mo, C) Al, D) C, E) N, F) Cr, G) Fe, H) Ni, and I) Ti.

### 4.1.5 Charging Results

After performing hydrogen charging for 72 hours, the hydrogen concentration in the samples was immediately measured using the TDS apparatus and the following graph, Figure 4.24, was obtained.

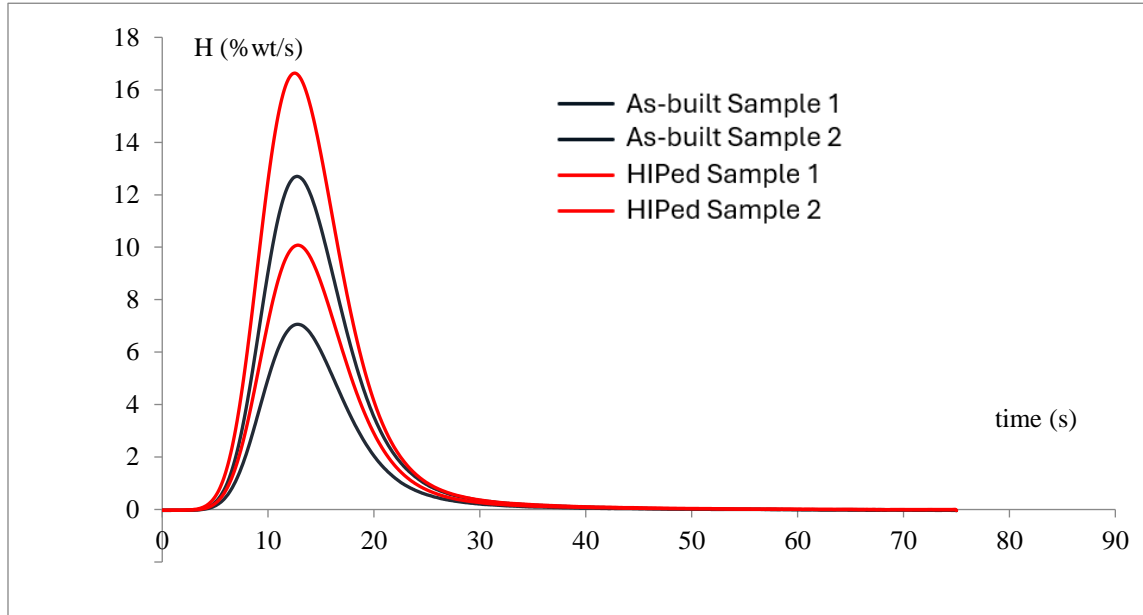


Figure 4.24: Hydrogen Flow Graph. As-built vs HIPed

This figure describes the hydrogen content inside the sample as it is melting. The final concentrations for all samples were 199.3 and 112.9 ppm for as-built samples 1 and 2, and 255.4 and 157.1 ppm for HIPed samples 1 and 2, resulting in a higher average (156.1 vs 206.3 ppm) for the HIPed samples. These numbers were calculated by integrating the area under each one of the flow curves.

These results are somewhat unexpected as the initial hypothesis was as-built samples having a higher concentration due to their higher percentages in random grain boundaries and smaller grain sizes, which initially was thought to highly affect hydrogen concentration levels. Other factors that could affect these results are that as-built samples also possess higher amounts of dislocations, precipitation, and residual stresses. These things inhibit hydrogen movement

throughout the sample and can even trap it, which might explain these results. Lastly, something that might also be affecting the results is the high levels of porosity found in these samples, but hydrogen-porosity dynamics haven't been studied very well yet. Concluding why HIPed samples experienced higher concentrations is difficult but sample porosity might be a significant contributor that cannot be fully understood yet. The rest of the experiments will help clarify this relationship and additional hydrogen concentration tests should be performed to have more trusted results.

## **4.2 MICROHARDNESS RESULTS**

Microhardness was performed with the sole purpose of observing the hardness changes across the sample after charging. As it can be seen in Figure 4.25, the highest hardness values are found near the charging face, with an average value of 428 HV. The values decrease as the indentations go further into the bulk of the sample, demonstrating the embrittlement caused by the hydrogen. The final indentations at the 5<sup>th</sup> column averaged a value of 353 HV, showing a difference of 75 HV across the entire 100  $\mu\text{m}$  distance.

It is necessary to perform more tests with the various specimen conditions to understand the material's behavior better. As-built samples are expected to have higher hardness values as it is known that HIPing relieves stresses and therefore makes the material more ductile.

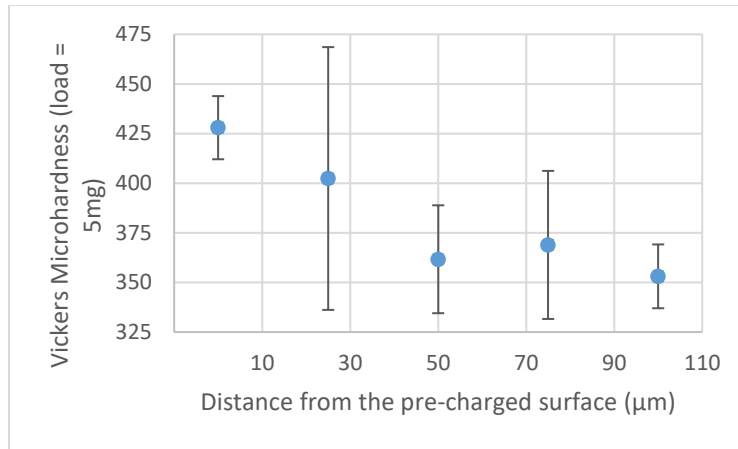


Figure 4.25: Microhardness Measurements Results

### 4.3 TENSILE TESTS RESULTS

Tensile testing was performed on both HIPed and as-built samples in H-charged and uncharged conditions to better understand the influence of microstructure and hydrogen content on mechanical performance. After testing, the graphs shown in Figures 4.26-27 were obtained. When analyzing the results of the as-printed samples, there is no significant difference between the hydrogen-free and the H-charged samples. When comparing the average UTS values for the non-charged and H-charged samples ( $559 \pm 23$  and  $536.9 \pm 12.7$  MPa, respectively), the difference in values is not very significant. The same happens when comparing Yield Strength values ( $545.4 \pm 13.7$  and  $516.3 \pm 22.7$  MPa, respectively) and Young's Modulus values (204 and 186 GPa, respectively). Elongation at fracture was expected to be significantly higher for non-charged samples but the values seem to be very similar. Overall, the H-charged and non-charged as-built samples appear to be very similar, with a slight decrease in mechanical properties for the H-charged samples. Higher precipitate, dislocation density, and residual stresses amounts might have caused this behavior where the non-charged samples were brittle enough from the start and weren't significantly affected by the hydrogen. Another important factor is porosity. Higher

porosity levels in the as-built samples also played an important role in their behavior as porosity can further induce fracture spots in the samples.

When observing the performance of the non-charged and H-charged HIPed samples, a more significant change is observed between them. For UTS values,  $547.1 \pm 42.7$  and  $368.4 \pm 81.4$  MPa, respectively, a significant difference is observed favoring the non-charged samples. The same happens for the Yield Strength ( $361.5 \pm 25.5$  and  $346 \pm 66$  MPa, respectively). The Young's Modulus values appear the same for both conditions ( $198.5 \pm 0.5$  and  $199 \pm 0$ , respectively). Finally, elongation values decrease significantly when the samples are charged (17.6% and 0.6%).

These tests show that hydrogen charging affects the HIPed samples significantly more than the as-built samples. It can affect the material's UTS and YS by lowering the loading capacity and drastically decreasing the fracture elongation (the same as the as-built H-charged samples). The only values that didn't seem to be affected were those of the Young's Modulus.

When looking back at the hydrogen concentration results, HIPed samples had a higher average hydrogen concentration. Although those results were questioned, tensile testing results might validate them as here it can be clearly seen that HIPed samples were the most affected, which, again, might be caused by higher hydrogen absorption/concentration.

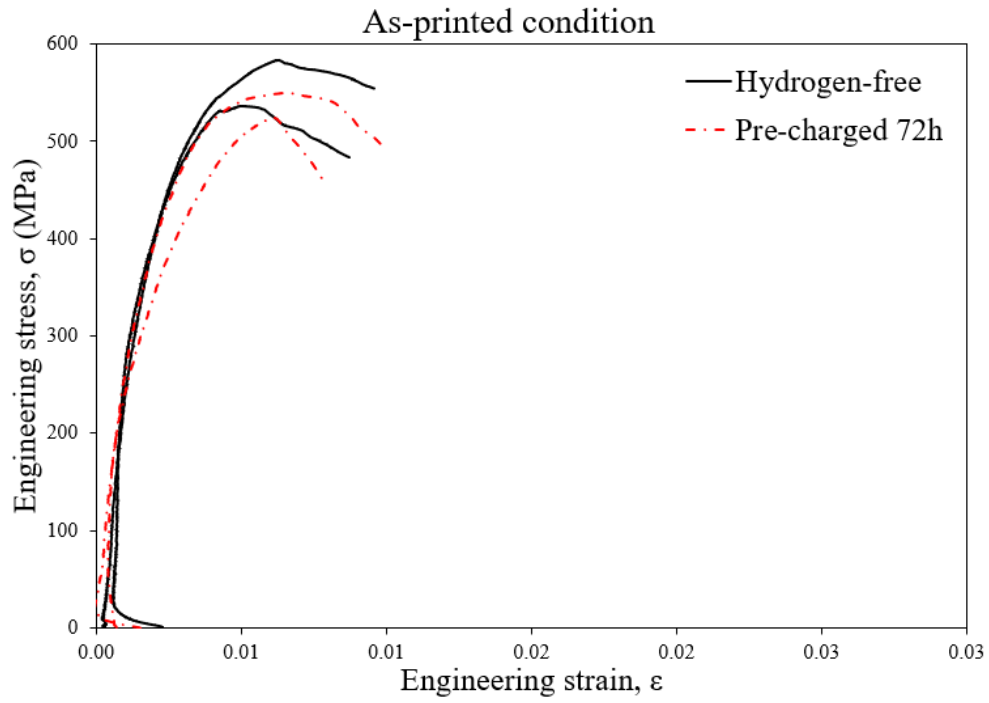


Figure 4.26: As-built Stress vs. Strain Graph

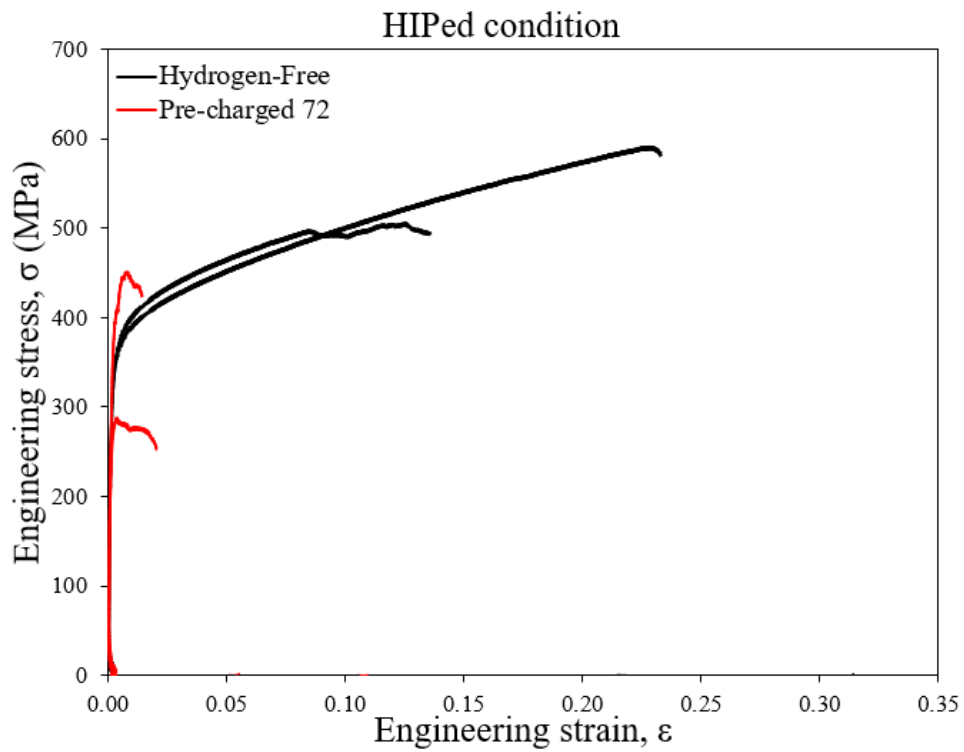


Figure 4.27: HIPed Stress vs. Strain Graph

Table 5. Mechanical Properties after Tensile Testing

Type	YS (0.2%) (MPa):	Young's Modulus (GPa)	UTS (MPa)	Elongation at failure
As-built non-charged	545.4 ± 13.7	204 ± 6	559.7 ± 23.2	0.55% ± 0.05%
As-built H-charged	516.3 ± 22.7	186 ± 1	536.9 ± 12.7	0.6% ± 0%
HIP non-charged	361.5 ± 25.5	198.5 ± 0.5	547.1 ± 42.7	17.7% ± 5.2%
HIP H-charged	346 ± 66	199 ± 0	368.4 ± 81.4	0.6% ± 0.2%

## 5. Conclusion

The study provided a detailed investigation into the microstructural characteristics and mechanical properties of Inconel 718 parts produced by EBM and subsequently subjected to hydrogen charging. The key results can be summarized as follows:

- Microstructure Characterization:

- EBSD Analysis and Microscopy:

Electron Backscatter Diffraction (EBSD) and Microscopy analysis revealed the presence of a hybrid matrix (elongated columnar grains and equiaxed grains) in the as-built samples, aligned with the build direction. These grains were indicative of the directional solidification characteristic of the EBM process. HIPing resulted in a reduction of the columnar grain structure, leading to more equiaxed grains. Also showed that both as-built and HIPed samples had a randomized crystallographic texture. HIPing did not significantly alter the grain structure but helped achieve a more uniform element distribution throughout the matrix.

- TEM Analysis:

Transmission Electron Microscopy (TEM) provided detailed insights into the dislocation structures and precipitate distributions. The HIPed samples exhibited few dislocations, suggesting that HIPing effectively reduced internal stresses. Additionally, TEM images revealed the presence of  $\gamma'$  and  $\gamma''$  precipitates, which are critical for the material's strength. Only HIPed samples were able to be analyzed.

- SEM Analysis:

Scanning Electron Microscopy (SEM) was used to examine the etched surfaces of both specimens. SEM images of the as-built samples showed

- Hydrogen Concentration:

Hydrogen charging increased the hydrogen content in both the as-built and HIPed samples. The HIPed samples showed a higher average hydrogen concentration (206.3 ppm vs. 156.1 ppm).

- Microhardness:

Hydrogen charging caused an increase in hardness near the charging face, demonstrating the hydrogen embrittling effect. The as-built samples showed a gradient in hardness from 428 HV near the surface to 353 HV deeper into the material.

- Tensile Properties:

Tensile tests revealed that hydrogen charging had a minimal effect on the mechanical properties of as-built samples. However, HIPed samples exhibited a significant reduction in ultimate tensile strength (UTS) and yield strength upon hydrogen charging suggesting these samples are more susceptible to HE as shown in the H-concentrations results.

In conclusion, while EBM offers a reliable method for fabricating high-strength Inconel 718 components, the susceptibility of HIPed samples to hydrogen embrittlement poses a significant concern. The findings suggest that post-processing methods such as HIPing, while beneficial for relieving residual stresses and enhancing ductility, may increase the material's vulnerability to hydrogen-induced degradation. Future work should focus on optimizing EBM parameters and post-processing techniques to mitigate hydrogen embrittlement and improve the performance of Inconel 718 components in hydrogen-rich environments. These advancements could lead to broader applications of EBM-fabricated Inconel 718 in critical industries such as aerospace and energy.

## References

- [1] E.-A. Choi *et al.*, “Strengthening Effect of Decreased Dislocation Density After Annealing in Pure Aluminum or Copper,” *Met. Mater. Int.*, vol. 30, no. 3, pp. 607–617, Mar. 2024, doi: 10.1007/s12540-023-01525-4.
- [2] “What Is The Relationship Between The Strength And Ductility Of A Material? - Mechanical Education.” Accessed: May 08, 2024. [Online]. Available: <https://www.mechanicaleducation.com/what-is-the-relationship-between-the-strength-and-ductility-of-a-material/>
- [3] V. G. Gavriljuk, V. M. Shyvaniuk, and S. M. Teus, “Hydrogen in metallic alloys – embrittlement and enhanced plasticity: a review,” *Corros. Rev.*, Mar. 2024, doi: 10.1515/correv-2022-0060.
- [4] S. Jothi, “Multiscale modelling and experimentation of hydrogen embrittlement in aerospace materials,” Ph.D., Swansea University (United Kingdom), Wales. Accessed: May 08, 2024. [Online]. Available: <https://www.proquest.com/docview/2008132144/abstract/4F3AB386C85241C8PQ/1>
- [5] E. D. McCarty, D. Wetzel, and B. S. Kloberdanz, “Hydrogen Embrittlement in Automotive Fastener Applications,” *SAE Trans.*, vol. 105, pp. 355–383, 1996.
- [6] T. Cassagne, H. Marchebois, and T. Mesquita, “A Review of Hydrogen Embrittlement of Nickel-Based Alloys for Oil and Gas Applications,” presented at the CORROSION 2021, OnePetro, Apr. 2021. Accessed: May 08, 2024. [Online]. Available: <https://dx.doi.org/>
- [7] “Heat Treating Metal Parts: A Comprehensive Guide.” Accessed: May 08, 2024. [Online]. Available: <https://www.tfgusa.com/heat-treating-metal-parts/>
- [8] B. N. Popov, J.-W. Lee, and M. B. Djukic, “Chapter 7 - Hydrogen Permeation and Hydrogen-Induced Cracking,” in *Handbook of Environmental Degradation of Materials (Third Edition)*, M. Kutz, Ed., William Andrew Publishing, 2018, pp. 133–162. doi: 10.1016/B978-0-323-52472-8.00007-1.
- [9] M. Hino, S. Mukai, T. Shimada, K. Okada, and K. Horikawa, “Effect of Baking on Hydrogen Embrittlement for High Strength Steel Treated with Various Zinc Based Electroplating from a Sulfate Bath,” *Mater. Trans.*, vol. 61, no. 12, pp. 2302–2306, Dec. 2020, doi: 10.2320/matertrans.MT-M2020245.
- [10] Y. Du *et al.*, “Hydrogen Embrittlement Behavior and Mechanism of Low Carbon Medium Manganese Steel Gas Metal Arc Welding Joints,” *JOM*, vol. 75, no. 10, pp. 4407–4420, Oct. 2023, doi: 10.1007/s11837-023-06064-2.
- [11] S. K. Dwivedi and M. Vishwakarma, “Hydrogen embrittlement in different materials: A review,” *Int. J. Hydrog. Energy*, vol. 43, no. 46, pp. 21603–21616, Nov. 2018, doi: 10.1016/j.ijhydene.2018.09.201.
- [12] H. Kasai, A. A. B. Padama, B. Chantaramolee, and R. L. Arevalo, “Behavior of Hydrogen and Hydrogen-Containing Molecules on Metal Surfaces,” in *Hydrogen and Hydrogen-Containing Molecules on Metal Surfaces: Towards the Realization of Sustainable Hydrogen Economy*, H. Kasai, A. A. B. Padama, B. Chantaramolee, and R. L. Arevalo, Eds., Singapore: Springer, 2020, pp. 31–72. doi: 10.1007/978-981-15-6994-4\_2.
- [13] H. Kakinuma, S. Ajito, T. Hojo, M. Koyama, and E. Akiyama, “Real-Time Visualization of Hydrogen Distribution in Metals Using Polyaniline: An Ultrasensitive Hydrogenochromic Sensor,” *Adv. Mater. Interfaces*, vol. 9, no. 18, p. 2101984, 2022, doi: 10.1002/admi.202101984.

- [14] A. Pundt and R. Kirchheim, “Hydrogen in metals: Microstructural aspects,” *Annu. Rev. Mater. Res.*, vol. 36, pp. 555–608, Jun. 2006, doi: 10.1146/annurev.matsci.36.090804.094451.
- [15] J.-P. Du, W. T. Geng, K. Arakawa, J. Li, and S. Ogata, “Hydrogen-Enhanced Vacancy Diffusion in Metals,” *J. Phys. Chem. Lett.*, vol. 11, no. 17, pp. 7015–7020, Sep. 2020, doi: 10.1021/acs.jpcclett.0c01798.
- [16] B. Ohl, “What Is the Difference Between FCC and BCC? (Crystal Structure, Properties, Interstitial Sites, and Examples),” Materials Science & Engineering Student. Accessed: May 08, 2024. [Online]. Available: <https://mstudent.com/what-is-the-difference-between-fcc-and-bcc-crystal-structure-properties-interstitial-sites-and-examples/>
- [17] K. Takasawa, Y. Wada, R. Ishigaki, and R. Kayano, “Effects of Grain Size on Hydrogen Environment Embrittlement of High Strength Low Alloy Steel in 45 MPa Gaseous Hydrogen,” *Mater. Trans.*, vol. 51, no. 2, pp. 347–353, 2010, doi: 10.2320/matertrans.M2009241.
- [18] W. Wang, H. Fu, H. Zhang, Y. Yan, and J. Li, “Effect of Grain Orientation on Hydrogen Embrittlement Behavior of Interstitial-Free Steel,” *Metals*, vol. 12, no. 6, Art. no. 6, Jun. 2022, doi: 10.3390/met12060981.
- [19] O. Barrera *et al.*, “Understanding and mitigating hydrogen embrittlement of steels: a review of experimental, modelling and design progress from atomistic to continuum,” *J. Mater. Sci.*, vol. 53, no. 9, pp. 6251–6290, May 2018, doi: 10.1007/s10853-017-1978-5.
- [20] T. Uehara, N. Wakabayashi, Y. Hirabayashi, and N. Ohno, “An atomistic study of grain boundary stability and crystal rearrangement using molecular dynamics techniques,” *Int. J. Mech. Sci.*, vol. 50, no. 5, pp. 956–965, May 2008, doi: 10.1016/j.ijmecsci.2007.09.001.
- [21] A. Oudriss *et al.*, “Grain size and grain-boundary effects on diffusion and trapping of hydrogen in pure nickel,” *Acta Mater.*, vol. 60, no. 19, pp. 6814–6828, Nov. 2012, doi: 10.1016/j.actamat.2012.09.004.
- [22] Z. Tong, H. Wang, W. Zheng, and H. Zhou, “Change in Hydrogen Trapping Characteristics and Influence on Hydrogen Embrittlement Sensitivity in a Medium-Carbon, High-Strength Steel: The Effects of Heat Treatments,” *Materials*, vol. 17, no. 8, Art. no. 8, Jan. 2024, doi: 10.3390/ma17081854.
- [23] B. Kagay, K. Findley, S. Coryell, and A. B. Nissan, “Effects of alloy 718 microstructure on hydrogen embrittlement susceptibility for oil and gas environments,” *Mater. Sci. Technol.*, vol. 32, no. 7, pp. 697–707, May 2016, doi: 10.1080/02670836.2016.1139225.
- [24] X. Li *et al.*, “Tensile mechanical properties and fracture behaviors of nickel-based superalloy 718 in the presence of hydrogen,” *Int. J. Hydrog. Energy*, vol. 43, no. 43, pp. 20118–20132, Oct. 2018, doi: 10.1016/j.ijhydene.2018.08.179.
- [25] J. A. Lee and S. Woods, “Hydrogen Embrittlement,” JSC-CN-36009, Apr. 2016. Accessed: May 06, 2024. [Online]. Available: <https://ntrs.nasa.gov/citations/20160005654>
- [26] W. Hui, H. Zhang, Y. Zhang, X. Zhao, and C. Shao, “Effect of nickel on hydrogen embrittlement behavior of medium-carbon high strength steels,” *Mater. Sci. Eng. A*, vol. 674, pp. 615–625, Sep. 2016, doi: 10.1016/j.msea.2016.08.028.
- [27] W. Paatsch, “Long-delay Hydrogen Embrittlement Phenomena In Plating High-strength Steel Components”.
- [28] M. Wetegrove *et al.*, “Preventing Hydrogen Embrittlement: The Role of Barrier Coatings for the Hydrogen Economy,” *Hydrogen*, vol. 4, no. 2, Art. no. 2, Jun. 2023, doi: 10.3390/hydrogen4020022.

- [29] J. J. Beaman, D. L. Bourell, C. C. Seepersad, and D. Kovar, “Additive Manufacturing Review: Early Past to Current Practice,” *J. Manuf. Sci. Eng.*, vol. 142, no. 110812, Sep. 2020, doi: 10.1115/1.4048193.
- [30] X. Zhang and F. Liou, “Chapter 1 - Introduction to additive manufacturing,” in *Additive Manufacturing*, J. Pou, A. Riveiro, and J. P. Davim, Eds., in Handbooks in Advanced Manufacturing. , Elsevier, 2021, pp. 1–31. doi: 10.1016/B978-0-12-818411-0.00009-4.
- [31] “What Is Material Extrusion 3D Printing?” Accessed: Apr. 09, 2024. [Online]. Available: <https://www.additivemanufacturing.media/articles/additive-manufacturing-with-material-extrusion>
- [32] M. Golab, S. Massey, and J. Moultrie, “How generalisable are material extrusion additive manufacturing parameter optimisation studies? A systematic review,” *Heliyon*, vol. 8, no. 11, p. e11592, Nov. 2022, doi: 10.1016/j.heliyon.2022.e11592.
- [33] “Material Extrusion.” Accessed: Apr. 09, 2024. [Online]. Available: [https://www.doitpoms.ac.uk/tlplib/add\\_manuf/extrusion.php](https://www.doitpoms.ac.uk/tlplib/add_manuf/extrusion.php)
- [34] “Material Extrusion | Additive Manufacturing Research Group | Loughborough University.” Accessed: Apr. 09, 2024. [Online]. Available: <https://www.lboro.ac.uk/research/amrg/about/the7categoriesofadditivemanufacturing/material-extrusion/>
- [35] “Material extrusion | Siemens Software,” Siemens Digital Industries Software. Accessed: Apr. 09, 2024. [Online]. Available: <https://www.sw.siemens.com/en-US/technology/material-extrusion/>
- [36] M. Leary, “Chapter 8 - Material extrusion,” in *Design for Additive Manufacturing*, M. Leary, Ed., in Additive Manufacturing Materials and Technologies. , Elsevier, 2020, pp. 223–268. doi: 10.1016/B978-0-12-816721-2.00008-7.
- [37] J. Butt, R. Bhaskar, and V. Mohaghegh, “Investigating the effects of extrusion temperatures and material extrusion rates on FFF-printed thermoplastics,” *Int. J. Adv. Manuf. Technol.*, vol. 117, no. 9, pp. 2679–2699, Dec. 2021, doi: 10.1007/s00170-021-07850-5.
- [38] Y. Rao, N. Wei, S. Yao, K. Wang, and Y. Peng, “A process-structure-performance modeling for thermoplastic polymers via material extrusion additive manufacturing,” *Addit. Manuf.*, vol. 39, p. 101857, Mar. 2021, doi: 10.1016/j.addma.2021.101857.
- [39] R. M. Mahamood, T. C. Jen, S. A. Akinlabi, S. Hassan, Kamar. O. Abdulrahman, and E. T. Akinlabi, “Chapter 6 - Role of additive manufacturing in the era of Industry 4.0,” in *Additive Manufacturing*, M. Manjaiah, K. Raghavendra, N. Balashanmugam, and J. P. Davim, Eds., in Woodhead Publishing Reviews: Mechanical Engineering Series. , Woodhead Publishing, 2021, pp. 107–126. doi: 10.1016/B978-0-12-822056-6.00003-5.
- [40] S. C. Altıparmak, V. A. Yardley, Z. Shi, and J. Lin, “Extrusion-based additive manufacturing technologies: State of the art and future perspectives,” *J. Manuf. Process.*, vol. 83, pp. 607–636, Nov. 2022, doi: 10.1016/j.jmapro.2022.09.032.
- [41] O. Gülcan, K. Günaydın, and A. Tamer, “The State of the Art of Material Jetting—A Critical Review,” *Polymers*, vol. 13, no. 16, Art. no. 16, Jan. 2021, doi: 10.3390/polym13162829.
- [42] E. Kornfellner, M. Königshofer, L. Krainz, A. Krause, E. Unger, and F. Moscato, “Measured and simulated mechanical properties of additively manufactured matrix-inclusion multimaterials fabricated by material jetting,” *3D Print. Med.*, vol. 10, no. 1, p. 4, Feb. 2024, doi: 10.1186/s41205-023-00201-y.

- [43] M. Baumers, C. Tuck, P. Dickens, and R. Hague, “How Can Material Jetting Systems Be Upgraded for More Efficient Multi-Material Additive Manufacturing,” 2014, Accessed: Apr. 09, 2024. [Online]. Available: <https://hdl.handle.net/2152/88741>
- [44] M. R. Silva, A. M. Pereira, Á. M. Sampaio, and A. J. Pontes, “Assessment of the Dimensional and Geometric Precision of Micro-Details Produced by Material Jetting,” *Materials*, vol. 14, no. 8, Art. no. 8, Jan. 2021, doi: 10.3390/ma14081989.
- [45] K. Kumar and G. S. Kumar, “An experimental and theoretical investigation of surface roughness of poly-jet printed parts: This paper explains how local surface orientation affects surface roughness in a poly-jet process,” *Virtual Phys. Prototyp.*, vol. 10, no. 1, pp. 23–34, Jan. 2015, doi: 10.1080/17452759.2014.999218.
- [46] Y.-L. Cheng and K.-C. Huang, “Preparation and Characterization of Color Photocurable Resins for Full-Color Material Jetting Additive Manufacturing,” *Polymers*, vol. 12, no. 3, Art. no. 3, Mar. 2020, doi: 10.3390/polym12030650.
- [47] A. Elkaseer, K. J. Chen, J. C. Janhsen, O. Refle, V. Hagenmeyer, and S. G. Scholz, “Material jetting for advanced applications: A state-of-the-art review, gaps and future directions,” *Addit. Manuf.*, vol. 60, p. 103270, Dec. 2022, doi: 10.1016/j.addma.2022.103270.
- [48] F. Zhang *et al.*, “The recent development of vat photopolymerization: A review,” *Addit. Manuf.*, vol. 48, p. 102423, Dec. 2021, doi: 10.1016/j.addma.2021.102423.
- [49] E. Guven, Y. Karpat, and M. Cakmakci, “Improving the dimensional accuracy of micro parts 3D printed with projection-based continuous vat photopolymerization using a model-based grayscale optimization method,” *Addit. Manuf.*, vol. 57, p. 102954, Sep. 2022, doi: 10.1016/j.addma.2022.102954.
- [50] I. Gibson, D. Rosen, and B. Stucker, “Vat Photopolymerization Processes,” in *Additive Manufacturing Technologies: 3D Printing, Rapid Prototyping, and Direct Digital Manufacturing*, I. Gibson, D. Rosen, and B. Stucker, Eds., New York, NY: Springer, 2015, pp. 63–106. doi: 10.1007/978-1-4939-2113-3\_4.
- [51] “What is Binder Jetting? (Definition, Pros, Cons and Uses).” Accessed: May 09, 2024. [Online]. Available: <https://www.twi-global.com/technical-knowledge/faqs/what-is-binder-jetting.aspx>
- [52] M. Ziaee and N. B. Crane, “Binder jetting: A review of process, materials, and methods,” *Addit. Manuf.*, vol. 28, pp. 781–801, Aug. 2019, doi: 10.1016/j.addma.2019.05.031.
- [53] D.-G. Ahn, “Directed Energy Deposition (DED) Process: State of the Art,” *Int. J. Precis. Eng. Manuf.-Green Technol.*, vol. 8, no. 2, pp. 703–742, Mar. 2021, doi: 10.1007/s40684-020-00302-7.
- [54] M. Ueda, D. Carter, K. Yamazaki, and Y. Kakinuma, “Intelligent process planning and control of DED (directed energy deposition) for rapid manufacturing,” *J. Adv. Mech. Des. Syst. Manuf.*, vol. 14, no. 1, pp. JAMDSM0015–JAMDSM0015, 2020, doi: 10.1299/jamdsm.2020jamdsm0015.
- [55] S. L. Sing, C. F. Tey, J. H. K. Tan, S. Huang, and W. Y. Yeong, “2 - 3D printing of metals in rapid prototyping of biomaterials: Techniques in additive manufacturing,” in *Rapid Prototyping of Biomaterials (Second Edition)*, R. Narayan, Ed., in Woodhead Publishing Series in Biomaterials. , Woodhead Publishing, 2020, pp. 17–40. doi: 10.1016/B978-0-08-102663-2.00002-2.

- [56] A. Jalili, "Sheet Lamination, Everything You Need," *The Additive Manufacturing*. Accessed: May 09, 2024. [Online]. Available: <https://theadditivemanufacturing.com/sheet-lamination-everything-you-need/>
- [57] D. I. Wimpenny, B. Bryden, and I. R. Pashby, "Rapid laminated tooling," *J. Mater. Process. Technol.*, vol. 138, no. 1, pp. 214–218, Jul. 2003, doi: 10.1016/S0924-0136(03)00074-8.
- [58] A. Vafadar, F. Guzzomi, A. Rassau, and K. Hayward, "Advances in Metal Additive Manufacturing: A Review of Common Processes, Industrial Applications, and Current Challenges," *Appl. Sci.*, vol. 11, no. 3, Art. no. 3, Jan. 2021, doi: 10.3390/app11031213.
- [59] D. Dev Singh, T. Mahender, and A. Raji Reddy, "Powder bed fusion process: A brief review," *Mater. Today Proc.*, vol. 46, pp. 350–355, Jan. 2021, doi: 10.1016/j.matpr.2020.08.415.
- [60] N. D. Dejene and H. G. Lemu, "Current Status and Challenges of Powder Bed Fusion-Based Metal Additive Manufacturing: Literature Review," *Metals*, vol. 13, no. 2, Art. no. 2, Feb. 2023, doi: 10.3390/met13020424.
- [61] D. Zhang, W. Niu, X. Cao, and Z. Liu, "Effect of standard heat treatment on the microstructure and mechanical properties of selective laser melting manufactured Inconel 718 superalloy," *Mater. Sci. Eng. A*, vol. 644, pp. 32–40, Sep. 2015, doi: 10.1016/j.msea.2015.06.021.
- [62] AMFG, "An Introduction to Electron Beam Melting," AMFG. Accessed: Apr. 09, 2024. [Online]. Available: <https://amfg.ai/2018/05/16/electron-beam-melting-introduction/>
- [63] "Arcam Shares| GE Additive." Accessed: Apr. 09, 2024. [Online]. Available: <https://www.ge.com/additive/press-releases/ge-agrees-purchase-controlling-shares-arcam-ab>
- [64] "Overview," Freemelt. Accessed: Apr. 09, 2024. [Online]. Available: <https://freemelt.com/investors/overview/>
- [65] H.-H. König *et al.*, "MiniMelt: An instrument for real-time tracking of electron beam additive manufacturing using synchrotron x-ray techniques," *Rev. Sci. Instrum.*, vol. 94, no. 12, p. 125103, Dec. 2023, doi: 10.1063/5.0177255.
- [66] "All About Electron Beam Additive Manufacturing (EBAM) 3D Printing." Accessed: May 09, 2024. [Online]. Available: <https://www.thomasnet.com/articles/custom-manufacturing-fabricating/electron-beam-additive-manufacturing-ebam-3d-printing/>
- [67] M. Galati, G. Rizza, S. Defanti, and L. Denti, "Surface roughness prediction model for Electron Beam Melting (EBM) processing Ti6Al4V," *Precis. Eng.*, vol. 69, pp. 19–28, May 2021, doi: 10.1016/j.precisioneng.2021.01.002.
- [68] B. Cheng and K. Chou, "Deformation Evaluation of Part Overhang Configurations in Electron Beam Additive Manufacturing," presented at the ASME 2015 International Manufacturing Science and Engineering Conference, American Society of Mechanical Engineers Digital Collection, Sep. 2015. doi: 10.1115/MSEC2015-9477.
- [69] "Electron Beam Melting: Everything You Need To Know About EBM 3D Printing - 3DSourced." Accessed: May 09, 2024. [Online]. Available: <https://www.3dsourced.com/guides/electron-beam-melting-ebm/>
- [70] T. Pasang *et al.*, "Additive manufacturing of titanium alloys – Enabling re-manufacturing of aerospace and biomedical components," *Microelectron. Eng.*, vol. 270, p. 111935, Feb. 2023, doi: 10.1016/j.mee.2022.111935.
- [71] A. Diniță, A. Neacșa, A. I. Portoacă, M. Tănase, C. N. Ilinca, and I. N. Ramadan, "Additive Manufacturing Post-Processing Treatments, a Review with Emphasis on

- Mechanical Characteristics,” *Materials*, vol. 16, no. 13, Art. no. 13, Jan. 2023, doi: 10.3390/ma16134610.
- [72] C. Eschey, S. Lutzmann, and M. F. Zaeh, “Examination of the Powder Spreading Effect in Electron Beam Melting (EBM),” Sep. 2009, Accessed: May 09, 2024. [Online]. Available: <https://hdl.handle.net/2152/88169>
- [73] M. K. Kolamroudi, M. Asmael, M. Ilkan, and N. Kordani, “Developments on Electron Beam Melting (EBM) of Ti–6Al–4V: A Review,” *Trans. Indian Inst. Met.*, vol. 74, no. 4, pp. 783–790, Apr. 2021, doi: 10.1007/s12666-021-02230-9.
- [74] “Freemelt ONE: The 3D printer for materials R&D,” Freemelt. Accessed: May 09, 2024. [Online]. Available: <https://freemelt.com/freemelt-one/>
- [75] H. Irrinki *et al.*, “Effects of Powder Attributes and Laser Powder Bed Fusion (L-PBF) Process Conditions on the Densification and Mechanical Properties of 17-4 PH Stainless Steel,” *JOM*, vol. 68, no. 3, pp. 860–868, Mar. 2016, doi: 10.1007/s11837-015-1770-4.
- [76] X. Zhao, Y. Wei, R. Mansour, S. Dadbakhsh, and A. Rashid, “Effect of Scanning Strategy on Thermal Stresses and Strains during Electron Beam Melting of Inconel 625: Experiment and Simulation,” *Materials*, vol. 16, no. 1, Art. no. 1, Jan. 2023, doi: 10.3390/ma16010443.
- [77] N. Hrabe, T. Gnäupel-Herold, and T. Quinn, “Fatigue properties of a titanium alloy (Ti–6Al–4V) fabricated via electron beam melting (EBM): Effects of internal defects and residual stress,” *Int. J. Fatigue*, vol. 94, pp. 202–210, Jan. 2017, doi: 10.1016/j.ijfatigue.2016.04.022.
- [78] K. Carpenter and A. Tabei, “On Residual Stress Development, Prevention, and Compensation in Metal Additive Manufacturing,” *Materials*, vol. 13, no. 2, Art. no. 2, Jan. 2020, doi: 10.3390/ma13020255.
- [79] T. Kurzynowski, M. Madeja, R. Dziedzic, and K. Kobiela, “The Effect of EBM Process Parameters on Porosity and Microstructure of Ti-5Al-5Mo-5V-1Cr-1Fe Alloy,” *Scanning*, vol. 2019, p. e2903920, Apr. 2019, doi: 10.1155/2019/2903920.
- [80] A. T. Polonsky, N. Raghavan, M. P. Echlin, M. M. Kirka, R. R. Dehoff, and T. M. Pollock, “Scan strategies in EBM-printed IN718 and the physics of bulk 3D microstructure development,” *Mater. Charact.*, vol. 190, p. 112043, Aug. 2022, doi: 10.1016/j.matchar.2022.112043.
- [81] D. Deng, J. Moverare, R. L. Peng, and H. Söderberg, “Microstructure and anisotropic mechanical properties of EBM manufactured Inconel 718 and effects of post heat treatments,” *Mater. Sci. Eng. A*, vol. 693, pp. 151–163, May 2017, doi: 10.1016/j.msea.2017.03.085.
- [82] R. Cunningham, S. P. Narra, T. Ozturk, J. Beuth, and A. D. Rollett, “Evaluating the Effect of Processing Parameters on Porosity in Electron Beam Melted Ti-6Al-4V via Synchrotron X-ray Microtomography,” *JOM*, vol. 68, no. 3, pp. 765–771, Mar. 2016, doi: 10.1007/s11837-015-1802-0.
- [83] C. Guo *et al.*, “Additive manufacturing of Ni-based superalloys: Residual stress, mechanisms of crack formation and strategies for crack inhibition,” *Nano Mater. Sci.*, vol. 5, no. 1, pp. 53–77, Mar. 2023, doi: 10.1016/j.nanoms.2022.08.001.
- [84] T. Persenot, G. Martin, R. Dendievel, J.-Y. Buffière, and E. Maire, “Enhancing the tensile properties of EBM as-built thin parts: Effect of HIP and chemical etching,” *Mater. Charact.*, vol. 143, pp. 82–93, Sep. 2018, doi: 10.1016/j.matchar.2018.01.035.

- [85] H. Galarraga, R. J. Warren, D. A. Lados, R. R. Dehoff, M. M. Kirka, and P. Nandwana, "Effects of heat treatments on microstructure and properties of Ti-6Al-4V ELI alloy fabricated by electron beam melting (EBM)," *Mater. Sci. Eng. A*, vol. 685, pp. 417–428, Feb. 2017, doi: 10.1016/j.msea.2017.01.019.
- [86] C. Ye, C. Zhang, J. Zhao, and Y. Dong, "Effects of Post-processing on the Surface Finish, Porosity, Residual Stresses, and Fatigue Performance of Additive Manufactured Metals: A Review," *J. Mater. Eng. Perform.*, vol. 30, no. 9, pp. 6407–6425, Sep. 2021, doi: 10.1007/s11665-021-06021-7.
- [87] P. Nandwana, "Electron beam melting of Inconel 718: Effects of processing and post-processing." Accessed: Jun. 07, 2024. [Online]. Available: <https://journals.sagepub.com/doi/epub/10.1080/02670836.2018.1424379>
- [88] S. Goel *et al.*, "Microstructure evolution and mechanical response-based shortening of thermal post-treatment for electron beam melting (EBM) produced Alloy 718," *Mater. Sci. Eng. A*, vol. 820, p. 141515, Jul. 2021, doi: 10.1016/j.msea.2021.141515.
- [89] J. Yao, Q. Tan, J. Venezuela, A. Atrens, and M.-X. Zhang, "Recent research progress in hydrogen embrittlement of additively manufactured metals – A review," *Curr. Opin. Solid State Mater. Sci.*, vol. 27, no. 5, p. 101106, Oct. 2023, doi: 10.1016/j.cossms.2023.101106.
- [90] N. K. Mohandas, A. Giorgini, M. Vanazzi, T. Riemslog, S. P. Scott, and V. Popovich, "Hydrogen Embrittlement of Inconel 718 Manufactured by Laser Powder Bed Fusion Using Sustainable Feedstock: Effect of Heat Treatment and Microstructural Anisotropy," *Metals*, vol. 13, no. 2, Art. no. 2, Feb. 2023, doi: 10.3390/met13020418.
- [91] E. Hosseini and V. A. Popovich, "A review of mechanical properties of additively manufactured Inconel 718," *Addit. Manuf.*, vol. 30, p. 100877, Dec. 2019, doi: 10.1016/j.addma.2019.100877.
- [92] H. Qi, "Review of INCONEL 718 Alloy: Its History, Properties, Processing and Developing Substitutes," *J. Mater. Eng.*, vol. 2, no. 8, pp. 92–100, Aug. 2012, doi: 10.3969/j.issn.1001-4381.2013.06.001.
- [93] A. Lingenfelter, "Welding of Inconel Alloy 718: A Historical Overview," *Superalloys 718 Metall. Appl. 1989*, pp. 673–683, 1989, doi: 10.7449/1989/Superalloys\_1989\_673\_683.
- [94] "Inconel 718: A Workhorse Material for Additive Manufacturing." Accessed: Jun. 03, 2024. [Online]. Available: <https://www.protolabs.com/resources/blog/inconel-718-a-workhorse-material-for-additive-manufacturing/>
- [95] M. Godec *et al.*, "Hybrid additive manufacturing of Inconel 718 for future space applications," *Mater. Charact.*, vol. 172, p. 110842, Feb. 2021, doi: 10.1016/j.matchar.2020.110842.
- [96] B. Sutton, E. Herderick, R. Thodla, M. Ahlfors, and A. Ramirez, "Heat Treatment of Alloy 718 Made by Additive Manufacturing for Oil and Gas Applications," *JOM*, vol. 71, no. 3, pp. 1134–1143, Mar. 2019, doi: 10.1007/s11837-018-03321-7.
- [97] I. V. S. Yashwanth and I. Gurrappa, "Corrosion Characteristics of New Superalloy Under Industrial Environmental Conditions," *J. Mater. Eng. Perform.*, vol. 26, no. 12, pp. 6057–6063, Dec. 2017, doi: 10.1007/s11665-017-3042-7.
- [98] D. G. Thakur, B. Ramamoorthy, and L. Vijayaraghavan, "Study on the machinability characteristics of superalloy Inconel 718 during high speed turning," *Mater. Des.*, vol. 30, no. 5, pp. 1718–1725, May 2009, doi: 10.1016/j.matdes.2008.07.011.
- [99] B. Sun, D. Wang, X. Lu, D. Wan, D. Ponge, and X. Zhang, "Current Challenges and Opportunities Toward Understanding Hydrogen Embrittlement Mechanisms in Advanced

- High-Strength Steels: A Review,” *Acta Metall. Sin. Engl. Lett.*, vol. 34, no. 6, pp. 741–754, Jun. 2021, doi: 10.1007/s40195-021-01233-1.
- [100] J. Ding *et al.*, “Characterization of precipitation in gradient Inconel 718 superalloy,” *Mater. Sci. Eng. A*, vol. 804, p. 140718, Feb. 2021, doi: 10.1016/j.msea.2020.140718.
- [101] S. Azadian, L.-Y. Wei, and R. Warren, “Delta phase precipitation in Inconel 718,” *Mater. Charact.*, vol. 53, no. 1, pp. 7–16, Sep. 2004, doi: 10.1016/j.matchar.2004.07.004.
- [102] J. Schneider *et al.*, “Microstructure Evolution in Inconel 718 Produced by Powder Bed Fusion Additive Manufacturing,” *J. Manuf. Mater. Process.*, vol. 6, no. 1, Art. no. 1, Feb. 2022, doi: 10.3390/jmmp6010020.
- [103] L. E. Murr, “Metallurgy of additive manufacturing: Examples from electron beam melting,” *Addit. Manuf.*, vol. 5, pp. 40–53, Jan. 2015, doi: 10.1016/j.addma.2014.12.002.
- [104] L. Liu, K. Tanaka, A. Hirose, and K. Kobayashi, “Effects of precipitation phases on the hydrogen embrittlement sensitivity of Inconel 718,” *Sci. Technol. Adv. Mater.*, vol. 3, no. 4, pp. 335–344, Jan. 2002, doi: 10.1016/S1468-6996(02)00039-6.
- [105] G. C. Obasi, Z. Zhang, D. Sampath, R. Morana, R. Akid, and M. Preuss, “Effect of Microstructure and Alloy Chemistry on Hydrogen Embrittlement of Precipitation-Hardened Ni-Based Alloys,” *Metall. Mater. Trans. A*, vol. 49, no. 4, pp. 1167–1181, Apr. 2018, doi: 10.1007/s11661-018-4483-9.
- [106] “ZEISS Crossbeam 340 & 540 - Sonde ionique focalisée by ZEISS Industrial Metrology | DirectIndustry.” Accessed: Jun. 04, 2024. [Online]. Available: <https://www.directindustry.fr/prod/zeiss-industrial-metrology/product-5693-2232563.html>
- [107] S. Goel, A. Sittiho, I. Charit, U. Klement, and S. Joshi, “Effect of post-treatments under hot isostatic pressure on microstructural characteristics of EBM-built Alloy 718,” *Addit. Manuf.*, vol. 28, pp. 727–737, Aug. 2019, doi: 10.1016/j.addma.2019.06.002.
- [108] S. Goel, M. Ahlfors, F. Bahbou, and S. Joshi, “Effect of Different Post-treatments on the Microstructure of EBM-Built Alloy 718,” *J. Mater. Eng. Perform.*, vol. 28, no. 2, pp. 673–680, Feb. 2019, doi: 10.1007/s11665-018-3712-0.
- [109] S. Goel, H. Mehtani, S.-W. Yao, I. Samajdar, U. Klement, and S. Joshi, “As-Built and Post-treated Microstructures of an Electron Beam Melting (EBM) Produced Nickel-Based Superalloy,” *Metall. Mater. Trans. A*, vol. 51, no. 12, pp. 6546–6559, Dec. 2020, doi: 10.1007/s11661-020-06037-z.
- [110] S. C. Krishna *et al.*, “Closed Die Hammer Forging of Inconel 718,” *J. Metall.*, vol. 2014, no. 1, p. 972917, 2014, doi: 10.1155/2014/972917.
- [111] H. Gan *et al.*, “Spheroidization Mechanism of Lamellar  $\delta$  Phase in Inconel 718 during Delta Processing,” *J. Mater. Eng. Perform.*, vol. 29, no. 6, pp. 3852–3857, Jun. 2020, doi: 10.1007/s11665-020-04909-4.

## Appendix

1.

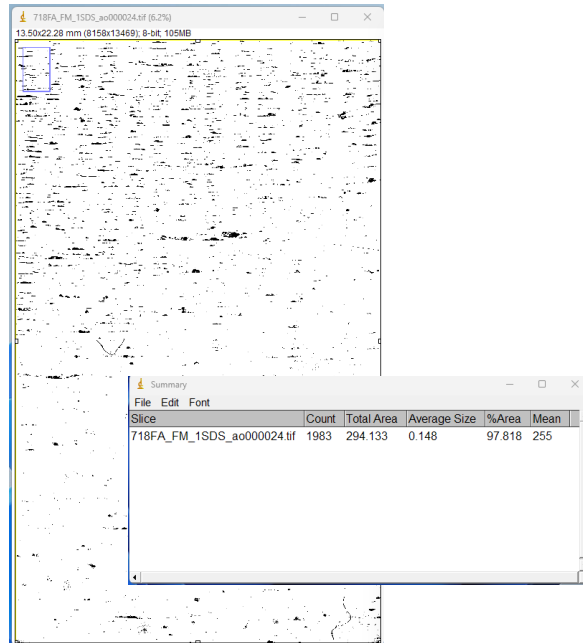


As-built Vertical Sample Cross section. Porosity Display.

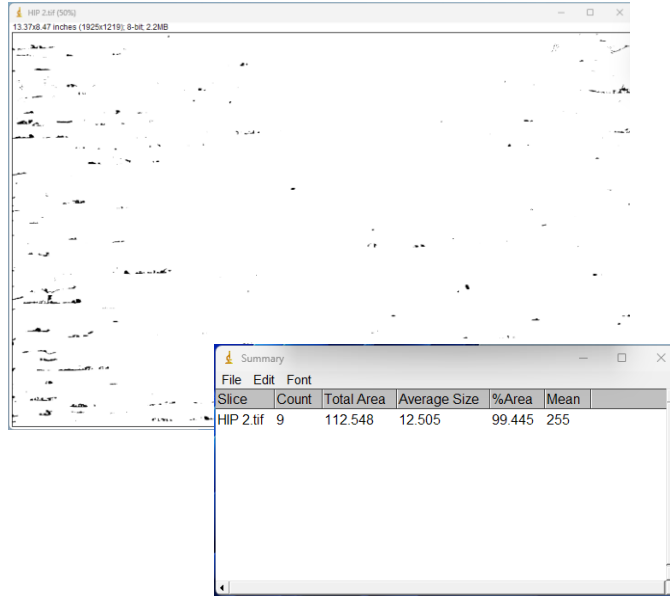


HIPed Vertical Sample Cross section. Porosity Display.

2.



As-built Porosity Measurement by ImageJ



HIPed Porosity Measurement by ImageJ

## **Vita**

Julio Cesar Diaz developed an interest in engineering at a young age. In 2022, he earned a Bachelor of Science in Mechanical Engineering from the University of Texas of El Paso. During his studies, he worked as an Undergraduate Research Assistant at the W.M. Keck Center, contributing to research in EBM.

He gained practical experience during the summer of 2023 at Cummins, where he redesigned an engine's drain fuel piping system. Additionally, he served as a Mechanical Engineer Intern at Freeport McMoran, focusing on project management.

In 2022, Julio Diaz started his graduate school at UTEP, aiming for a master's degree specializing in additive manufacturing. His dedication to innovation and strong problem-solving skills make him a valuable asset in the AM industry.

Contact Information: [j97cdm@gmail.com](mailto:j97cdm@gmail.com)